UNIVERSITÀ DEGLI STUDI DI MILANO
FACOLTÀ DI SCIENZE E TECNOLOGIE

Corso di Laurea Magistrale di Fisica

Inter-fractional monitoring of ^{12}C ions treatments with the Dose Profiler detector: simulation studies and clinical trial results at the CNAO facility

Relatore:
Paolo AROSIO
Relatore esterno:
Yunsheng DONG

Tesi di Laurea di:
Leonardo LAMPERTICO
Matricola: 08062A

Anno Accademico 2023/2024

Contents

Introduction

Today, cancer is the second leading cause of death worldwide, as stated on the last report of the World Health Organization (WHO) [1]. According to the Global Cancer Statistics 2020 report, jointly produced by the American Cancer Society (ACS) and the International Agency for Research on Cancer (IARC), there were approximately 19.3 million new cases of cancer and 10 million deaths from the disease worldwide in 2020 [2]. Current treatments for cancer include surgery, chemotherapy, immunotherapy and radiotherapy, which uses ionising radiation to kill cancer cells. In the clinical setting, several therapies may be used simultaneously to increase the effectiveness of tumour treatment. In particular, X-rays and electrons are used in conventional radiotherapy as a minimally invasive alternative for the treatment of certain diseases.

Hadrontherapy is a type of radiotherapy that uses beams of heavy charged particles such as protons and carbon ions. One of the advantage of this type of therapy is due to the characteristic depth-dose profile of the projectile. Most of the energy is deposited in a region at the end of the particle path, the so called *Bragg peak*. This allows the dose to be maximised in the tumour region while significantly sparing healthy tissues and organs in the vicinity of the tumour. In addition, hadrontherapy is more efficient in the treatment of radioresistant tumours. Today, there are 109 facilities for treating tumours with hadrontherapy, and 36 are under construction [3]. There are three facilities in Italy: CATANA (Centre for Advanced Hadrontherapy and Nuclear Applications) in Catania, the Proton Therapy Centre in Trento and CNAO (National Centre for Oncological Hadrontherapy) in Pavia, the only one in Italy that uses both protons and carbon ions.

One of the major open challenges in hadrontherapy is range monitoring. The Bragg peak position of the primaries depends on the beam energy and the amount of material crossed by the projectiles. If morphological changes occur along the primary beam path, the Bragg peak can be shifted, leading to an under-dosage of the tumour area and a release of unwanted dose into healthy tissues. The aim of range monitoring techniques is to provide a method that can detect any morphological changes occurred during the treatment, giving the possibility to radiotherapists to change and adapt the treatment plan. The range monitoring methods proposed so far make use of the secondary and tertiary products generated by the interaction between the primary beam and the tissue. The INSIDE project (INnovative Solution for In-beam DosimEtry in hadrontherapy) has proposed a range monitoring method for hadrontherapy treatments with protons and carbon ions. It is a bimodal system consisting of a charged particle detector and two PET heads, installed at the CNAO facility. The detector, called Dose Profiler, is used in the case of carbon ion beams and it is capable of detecting secondary protons produced during the treatments. Due to the correlation between the primary beam Bragg peak position and the production point of the secondary protons, it is possible to identify possible morphological changes occurred during the treatment.

In this thesis, I analysed the performance of the Dose Profiler in measuring the morphological changes in patients by using the data collected by the detector during a clinical trial conducted at the CNAO facility. Specifically, I compared the 3D emission distribution maps of the charged secondary fragments reconstructed at each treatment fraction, using the gamma index test. The objectives of this work are twofold: first, to optimise the parameters of the gamma index test in order to find suitable values for all clinical cases; second, to find an estimate of the sensitivity of the Dose Profiler in the detection of morphological changes.

Chapter 1 discusses particle interactions with matter, range uncertainties and range monitoring in hadrontherapy with protons and carbon ions. Chapter 2 is devoted to the description of the Dose Profiler and the clinical study carried out at CNAO, as well as the methods used to reconstruct the tracks of the detected fragments. Also the gamma index test is illustrated. The last chapter contains

the analysis of the data collected in the study of three patients that presented a morphological change during their treatment. The strategies adopted and the results obtained in the evaluation of the Dose Profiler performances are described and discussed.

Chapter 1

Heavy ions particles therapy

Today, conventional external beam radiotherapy adopts highly penetrating X-rays and γ-rays. The goal of the treatments is to damage the DNA of the cancer cells leading to their apoptosis. The aim of all types of radiotherapy is to deliver as much energy as possible to the tumour, while sparing as much healthy tissue as possible.

In the second half of the 20^{th} century, a new branch of radiotherapy called hadrontherapy has been developed. It adopts charged hadrons such as protons or carbon ions instead of photons and electrons [4]. The physical mechanisms behind the toxic effects on cells are fundamentally different for the two techniques. The physical aspects of the interaction of hadrons with matter are explained in Section 1.1. Hadrontherapy is mainly used to treat tumours that are often inoperable or resistant to traditional radiotherapy treatments, and since 2017 has been included in the Essential Levels of Assistance provided by the National Health System. To date, according to the Particle Therapy Co-Operative Group (PTCOG), there are 134 particle accelerators in operation around the world, including those in scientific research institutes. By the end of 2022, more than 360,000 patients worldwide will have been treated with particle therapy: about 312,000 patients with protons, about 46,800 with C-ions and about 3,500 with He, pions and other particles.

The hadrons used in clinical practice are mainly protons and carbon ions. The first are accelerated by cyclotrons or synchrotrons in an energy range between 50 and 250 MeV; the latter are accelerated by synchrotrons in an energy range between

80 and 400 MeV/u. Due to the particular physical properties of the particles used, hadrontherapy offers some significant advantages over conventional radiotherapy. All the biological aspects will be discussed in Section 1.2.

One of the fundamental characteristics and requirements of hadrontherapy is the need to deliver the incident particle beam to the tumour with the highest possible spatial precision. For this reason, there is a field of research dedicated to range monitoring, which will be presented in Section 1.3 and which is the purpose of the experiment in this thesis.

1.1 Particle interactions with matter

Charged particles, such as protons and carbon ions, lose energy in matter mainly through Coulomb interactions. Nuclear reactions can also play an important role in the interaction with the medium, especially for carbon ions (nuclear fragmentation). This section discusses the interaction of charged particles with matter and the various physical aspects involved.

1.1.1 Stopping power

The stopping power S is used to quantify the energy loss per unit length of a charged particle as it travels through a medium. it is defined as:

$$S(E) = -\frac{dE}{dx} \tag{1.1}$$

and is expressed in MeV/mm or similar. It depends on the incident particle (charge, mass and energy), the nature of the target and the type of interaction taking place. Indeed, four different modalities that compete in the interaction can be distinguished, depending on the distance b from the target atom:

- for b > r_a excitations/de-excitations of the target atom can occur due to "soft" collision (S_{soft}), i.e. interaction of the electric field of the incident radiation with the electric field of the entire target atom. This type of interaction is very probable, but it's very weak;

- for b $\sim$ r$_a$ ionization of the target atom can occur due to a "hard" collision (S$_{hard}$) and the energy transfer from the incident particle to the atomic electron.
- for b $<<$ r$_a$ the incident particle is deflected by interaction with the field of the nucleus target (inelastic scattering) and it can be accelerated or decelerated (for light particles such as electrons). The acceleration of a charged particle generates bremsstralhung radiation at the expense of kinetic energy (S$_{rad}$).
- for b $\approx$ 0 elastic or inelastic collisions with the nucleus (S$_{nucl}$) can also occur with a cross sections of the order of $\sigma_{nucl} \approx 10^{-8}\sigma_{atom}$.

The stopping power is equal to the total energy lost by the particle in all the possible ways described above, so it can be written as:

$$S_{tot} = S_{hard} + S_{soft} + S_{rad} + S_{nucl} \tag{1.2}$$

The study of stopping power began in 1913 with Niels Bohr, who estimated it in a classical way; with the advent of quantum mechanics and relativity, Hans Albrecht Bethe and Felix Bloch were able to give a much more accurate estimate in 1931 based on some basic assumptions:

- Incident particles have a much higher velocity than atomic electrons, which can be considered stationary;
- Incident particles have much greater mass than atomic electrons;
- Only the electromagnetic interaction has been considered, neglecting the nucleus-nucleus interactions;
- Energy loss is dominated by hard and soft collisions ($S_{tot} \approx S_{hard} + S_{soft}$).

The Bethe-Bloch theory well describes the stopping power for kinetic energies of the incident particle in the range of $0.1 \leq \beta\gamma \leq 1000$, which includes the energies used in hadrontherapy. The Bethe-Bloch equation is of this form [5]:

$$-\frac{dE}{dx} = 4\pi N_A r_e^2 m_e c^2 \rho \frac{Z_p^2}{\beta^2} \frac{Z_t}{A_t} \left[\frac{1}{2} \ln \left(\frac{2 m_e c^2 \beta^2 \gamma^2 T_{max}}{I^2} \right) - \beta^2 - \frac{\delta}{2} - \frac{C}{Z_t} \right] \tag{1.3}$$

where:

- N_A is the Avogadro number;
- r_e and m_e are the radius and mass of electron respectively;
- ρ, Z_t and A_t are density, atomic number and atomic mass of the target, respectively;
- Z_p and $\beta = \frac{v_p}{c}$ are the mean atomic number and the velocity of the incident particle;
- T_{max} and I are the maximum transferable kinetic energy per single impact from the projectile and the average excitation potential of the target atomic electrons;
- $\gamma = (1 - \beta^2)^{-\frac{1}{2}}$ is the Lorentz factor;
- δ is the density correction term, relevant only for ultrarelativistic particles; it takes into account the effect of electronic polarization. It shields the influence of incident radiation on even the most distant electrons, reducing stopping power [6];
- C is the shell correction term and it's significant when the velocity of the incoming particle becomes comparable to or less than the orbital velocity of the target electrons. In these cases a build-up phenomenon can occur and the target electrons bind to the projectile, reducing its effective charge Z_{eff} and consequently S_{tot}.

As can be seen from Figure 1.1, the evolution of the stopping power as a function of incident particle energy can be divided into four zones (only one of which is the Bethe-Bloch zone). After a rapid initial increase, the curve reaches a maximum; then the range of energies begins where the Bethe-Bloch approximation works: as the particle velocity increases, the time during which the charged particle can interact with the atomic electrons decreases. As a result, the energy transferred is less and therefore the stopping power decreases. After reaching a minimum, when the particle velocity is close to the speed of light (c), the stopping power increases significantly due to relativistic phenomena such as the Cherenkov effect.

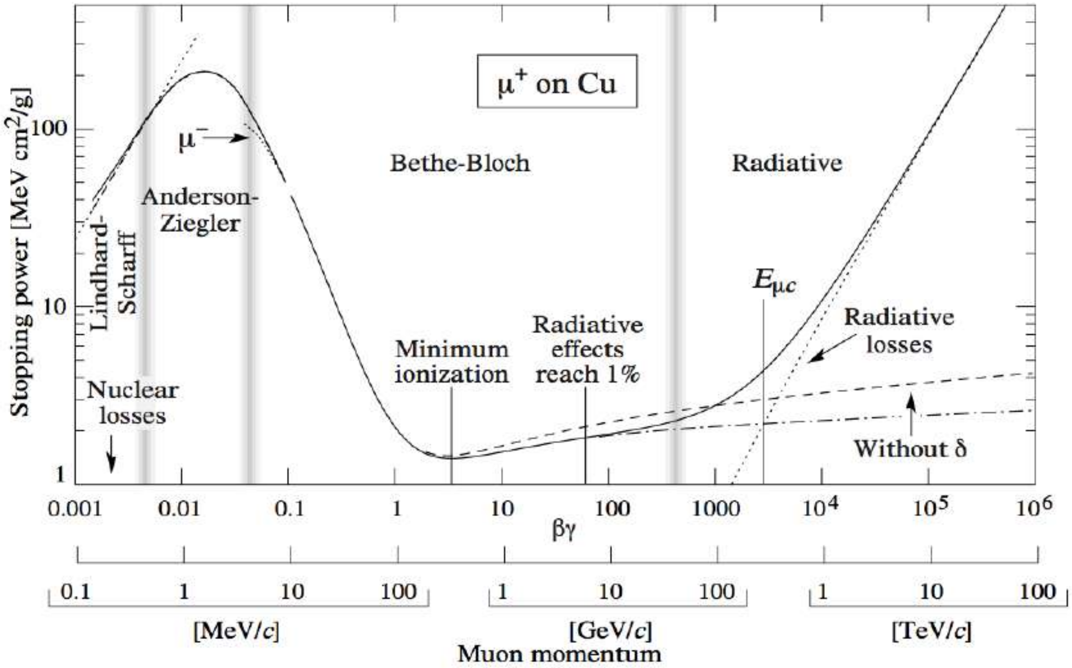

Figure 1.1: Bethe-Bloch energy loss distribution as a function of the energy of the charged particle (Antimuon against a copper target) [7].

Figure 1.2 compares the stopping power in different targets: notice that the trend is similar for all materials: the value decreases until it reaches a minimum and then increases again as the speed increases due to relativistic effects.

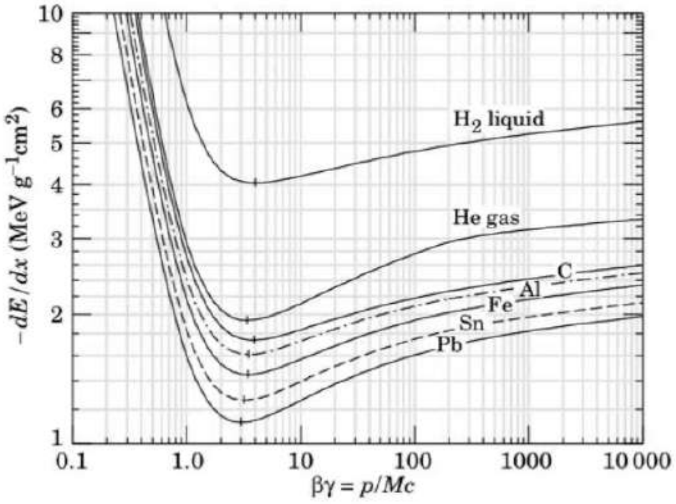

Figure 1.2: Comparison of the mass stopping power (divided by the density of the target) for muons incident at different energies on different targets [8].

1.1.2 Bragg peak

A hadron crossing a target material releases a small portion of its energy at the beginning of its path; as it penetrates the material, the velocity of the charged particle decreases and therefore the energy transferred per unit length increases, (as can be seen from Figure 1.2 until the particle velocity gets close to the speed of light). This implies that the maximum energy release occurs at the end of the path (Figure 1.3, protons), giving rise to the so-called Bragg peak (BP). Different beam energies correspond to different depths reached in the same material: the greater the energy of the primary particles, the greater the depth of the Bragg Peak. These characteristics of charged particle beams make hadrontherapy a much more precise technique than conventional radiotherapy with X-rays, which has a much more uniform dose release (Figure 1.3, X-rays). This is why hadrontherapy is a tool that significantly helps in the treatment of deep solid tumours close to Organs At Risk (OARs).

Since the Bragg peak has a typical depth of few millimiters, in order to deliver a uniform dose to the entire tumour volume, beams of different energies are used to create a Spread Out Bragg Peak (SOBP), as shown in the Figure 1.4. In this

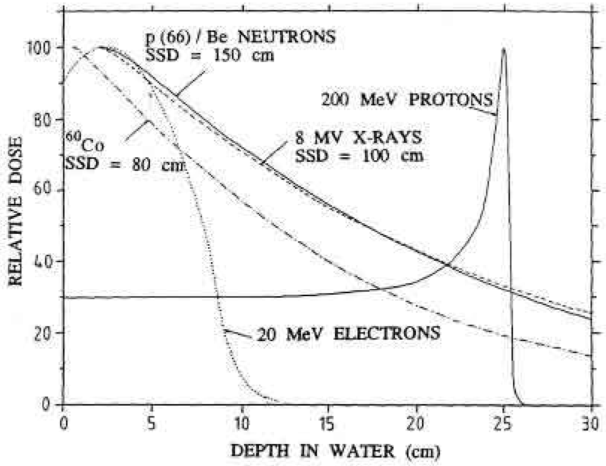

Figure 1.3: Relative dose released in water as a function of depth reached for different ionising beams. Note the Bragg peak at about 25 cm for protons with a kinetic energy of 200 MeV [4].

case, the beam is composed of particles of different energies and it is characterised by Bragg peaks at different depths, allowing a better dose coverage over the whole tumour volume.

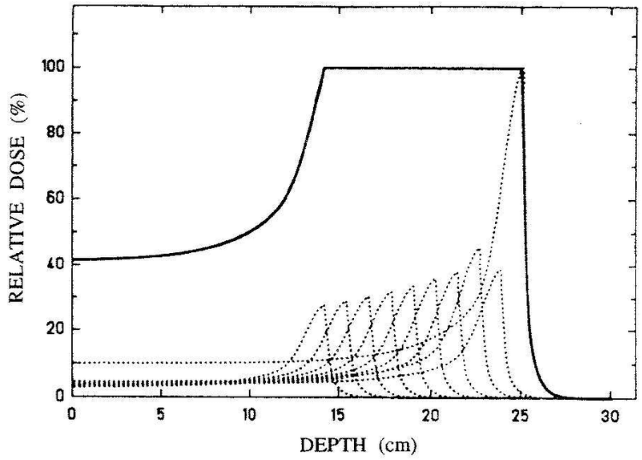

Figure 1.4: Example of a SOBP: the dotted line shows the doses released by the different monoenergetic proton beams, the solid line shows the total dose released [9].

1.1.3 Range

According to the theory of CSDA [10], the total distance travelled by a charged particle in a given material is defined as the range. Since the nature of the interactions is stochastic, the number of collisions required to bring a radiation particle to rest in the medium will vary slightly for each particle. Therefore there will be a small variation in the range, known as range straggling. Thus, particle range refers to an average range defined as the distance travelled beyond which half of the incident particles are stopped. Experimentally, it is possible to measure the average range of a monoenergetic beam of particle with a given intensity impinging on a target of a certain material. The average range of a monoenergetic beam with initial energy E_0 is defined as

$$R(E) = \int_0^{E_0} \left(\frac{dE'}{dx}\right)^{-1} dE' \tag{1.4}$$

Figure 1.5 shows the trends of the range of different particles as a function of the kinetic energy.

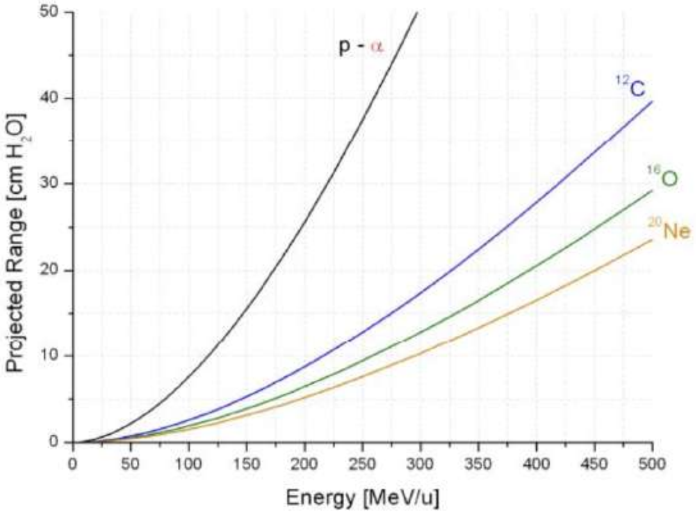

Figure 1.5: Range of different particles in water as a function of energy [11].

1.1.4 Multiple Coulomb Scattering

A charged particle impinging in a target material may interact with the nuclei of atoms in the medium during its trajectory. The process with the higher cross section is elastic scattering due to Coulomb forces. In particular, if the mass of the projectile is much less than the mass of the target nucleus, the energy lost in the process can be assumed as negligible and, the only result, is a significant deflection of the projectile particle. Multiple scattering does not contribute significantly to energy loss but is central to the phenomenon of lateral broadening of the primary ion beam. The magnitude of this effect increases with the atomic number of the material [12]. For this reason multiple scattering is very important in hadrontherapy because it causes angular dispersion of the primary beam in the patient as it penetrates, as shown in Figure 1.6; the beam broadening can be quantified by the Full Width at Half Maximum (FWHM).

The models used to estimate the net deflection angle experienced by the particle in the case of multiple scattering are extremely complicated. Nevertheless, thanks to the Central Limit Theorem, for applications of interest in particle therapy, a very good approximation can be obtained using a Gaussian distribution derived as the sum of many deflection events with random orientation. The distribution is centred at $\theta = 0$, with RMS equal to θ_0 and it is known as the Highland equation [13]:

$$\theta_0 = \frac{14.1MeV}{\beta cp} Z_p \sqrt{\frac{L}{L_0}} \left[1 + 0.0083 \ln \left(\frac{L}{L_0} \right) \right] \tag{1.5}$$

where L is the path travelled in the target and L_0 is the radiation length of the material and is related to the energy loss of the particles interacting with it. Figure 1.6 shows that multiple Coulomb scattering has a greater effect on protons than on carbon ions. Although the angle of beam broadening increases with the atomic number of the projectile (Z_p of carbon ions is six times that of protons), it is also inversely proportional to the mass and velocity of the charged particle. This is why carbon ions show a much smaller spread than protons for the same penetration depth.

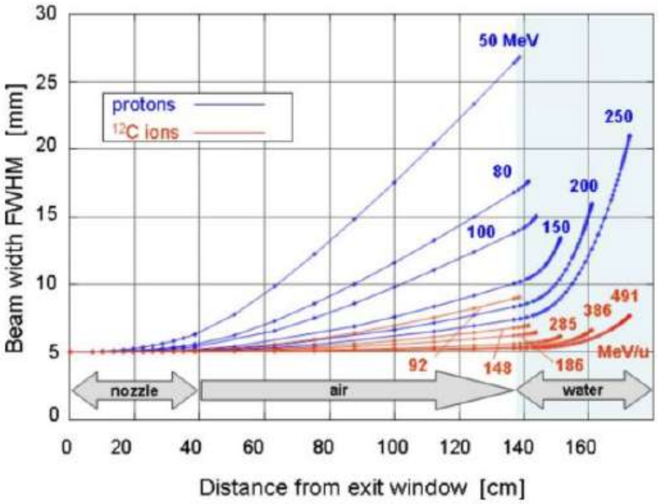

Figure 1.6: Lateral scattering for beams at different energies of protons and carbon ions in air and water as a function of depth (MC) [14].

1.1.5 Nuclear fragmentation

In hadrontherapy, the primary beam kinetic energies are of the order of tens up to hundreds MeV per nucleon, which is sufficient to overcome the Coulomb barrier and allow nuclear reactions to take place. Such an energetic projectile is able to fragment the target nucleon (target fragmentation) or, if it is a $Z > 1$ ion, to fragment itself (projectile fragmentation). Protons can only fragment the target nucleus, but heavier ions such as the carbon ion can fragment and produce charged particles with energies similar to those of the primary beam, but with a lower mass. Charged secondary projectile fragments release energy just beyond the Bragg peak, producing a tail in the depth-dose distribution (Figure 1.7).

A geometric approximation is used to model these phenomena, whereby nuclei are considered as simple spheres. Central and peripheral nuclear reactions are distinguished, depending on the size of the impact parameter b, defined as the distance between the trajectories of the two reacting nuclei, with respect to the size of the particles themselves. For small values of b, central collisions can occur and all the nucleons of the reacting nuclei are involved, resulting in the destruction of both. In

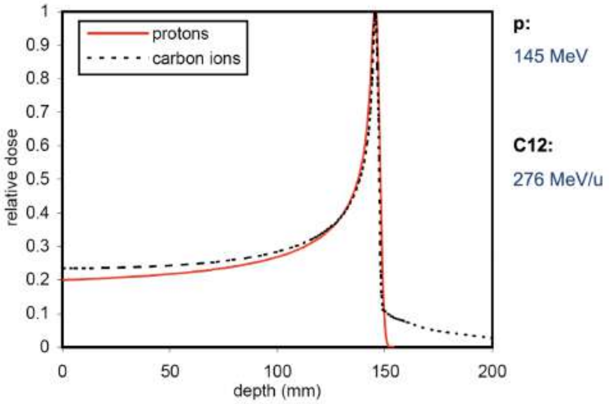

Figure 1.7: Pristine Bragg peaks for a 145 MeV proton beam and a 276 MeV carbon beam with the same range on a water target, analytically calculated (degraded with 3 mm ripple filter) [15].

this case, lighter fragments with a very wide angular distribution can be produced. As the impact parameter increases, peripheral collisions occur: in this type of interaction, the projectile and target overlap in a small region, resulting in incomplete fusion of the nuclei. As a result, only a few fragments are observed, very often at approximately the same velocity as the projectile and in the same beam direction. Peripheral collisions are the most frequent during the projectile path, causing the beam particles to lose one or more nucleons. The abrasion-ablation model, shown in Figure 1.8, divided into two stages is used to describe this physical process. In the abrasion phase, the two nuclei overlap (completely or partially), excite each other and form a highly reactive zone (fireball). During the ablation phase, the system undergoes thermalisation: the nuclear fragments and the fireball lose their excited state through the evaporation of gamma rays and particles such as protons, neutrons or light particles.

Nuclear fragmentation is a much less likely process than interaction with atomic electrons. Nevertheless, it is a very important process to consider for hadrontherapy, as it has several consequences:

- Loss of primary beam fluence, resulting in the production of ions with lower Z in treatments with ^{12}C.

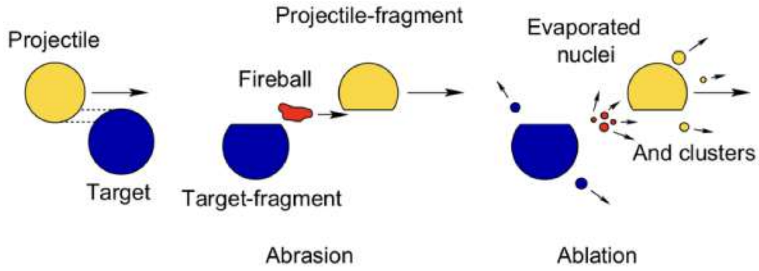

Figure 1.8: Simplified representation of the abrasion-ablation model phases [16].

- Changes in dose distribution: the secondary or even tertiary charged fragments that are produced release dose along their path modifying the total dose distribution (Figure 1.9).
- Secondary charged fragments in some cases have enough energy to leave the patient. They can be detected and exploited to evaluate the range of the incident beam.

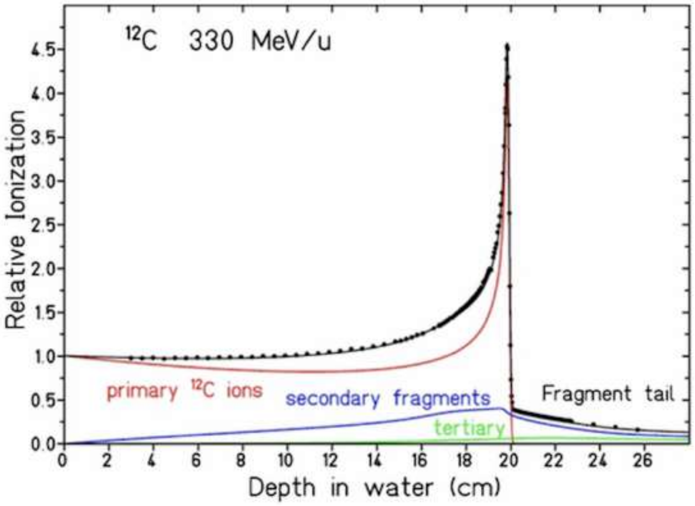

Figure 1.9: Dose contributions of primary ions (red line), secondary (blue line) and tertiary (green line) fragments calculated for a 330 MeV/u ^{12}C ion beam stopping in water as a function of the depth. The black line is the total calculated Bragg curve [17].

1.2 Biological Effect

The physical quantity used to quantify biological damage is dose, defined as the energy absorbed by biological tissue per unit mass and expressed in *Gray* [1 $Gy = 1$ J/kg].

$$D = \frac{dE}{dm} \tag{1.6}$$

The dose has different biological effects depending on the type of incoming radiation and type of target tissue. For this reason, in radiobiology, two other fundamental quantities are introduced to describe the biological effects of radiation. The first is the equivalent dose, which takes account of the fact that different ionising radiation have different biological effects in the same target tissue. It is defined as:

$$H_T = \sum_R w_R D_R \tag{1.7}$$

where w_R is a weighting factor that depends on the incident radiation type. It is expressed in *Sievert* (Sv). The second is the effective dose, which takes into account the fact that different biological tissues have different sensitivities to the same ionising radiation. It is defined as:

$$E_T = \sum_T w_T H_T \tag{1.8}$$

where w_T is a weighting factor that depends on the target tissue. Clinical studies have succeeded in tabulating the weighting factor w_T for all human organs [18] and the values are constantly updated.

The biological effects of exposure to ionising radiation can vary depending on the type of radiation, the dose released or the time of exposure. They can be divided into two categories:

- Deterministic
- Stochastic

Deterministic effects occur immediately after exposure if the dose is above a certain threshold. They occur when the absorbed dose is of the order of Sv or higher.

Beyond the threshold, the effects become worse as the dose increases. On the other hand, a cause of stochastic effects cannot be immediately identified. This is the case with low dose radiation exposures where no immediate tissue damage is expected. Under these conditions, typical side effects are genetic mutations or tumour, but unlike deterministic effects, they occur years later, so their causal relationship with the absorbed dose cannot be established with certainty [19].

1.2.1 DNA strand breaks

In radiotherapy, the energy lost from the incident radiation is released into human biological tissues by damaging biological molecules. It has been shown that the molecule most responsible for the biological effect is the DNA. There are two types of damage that ionising radiation can cause to DNA:

- Direct
- Indirect

By direct effects, it means that the radiation energy is deposited in the DNA, which is responsible for the biological effect. Two types of damage can be distinguished: single-strand breaks (SSB) and double-strand breaks (DSB), which refer to single or double damage to the DNA strands. Indirect effects mean that the radiation energy is deposited in the environment and then chemically transferred to the DNA responsible for the biological effect. In this case, since the cellular environment is aqueous, the radiation ionises H_2O molecules, leading to the formation of highly reactive free radicals (reactive oxygen species) that can induce SSBs in the DNA [20].

To repair radiation induced damage, the cell has several DNA repair mechanisms [22]; DSBs are more difficult to repair than SSBs, but both types of damage are not always lethal for the cell. For example, homologous recombination is a mechanism that can perfectly repair DSB damage [19]. However, it requires that the DNA has already been duplicated and therefore can only be completed in the G2 phase of the cell cycle. The success of the various mechanisms in repairing SSBs and DSBs

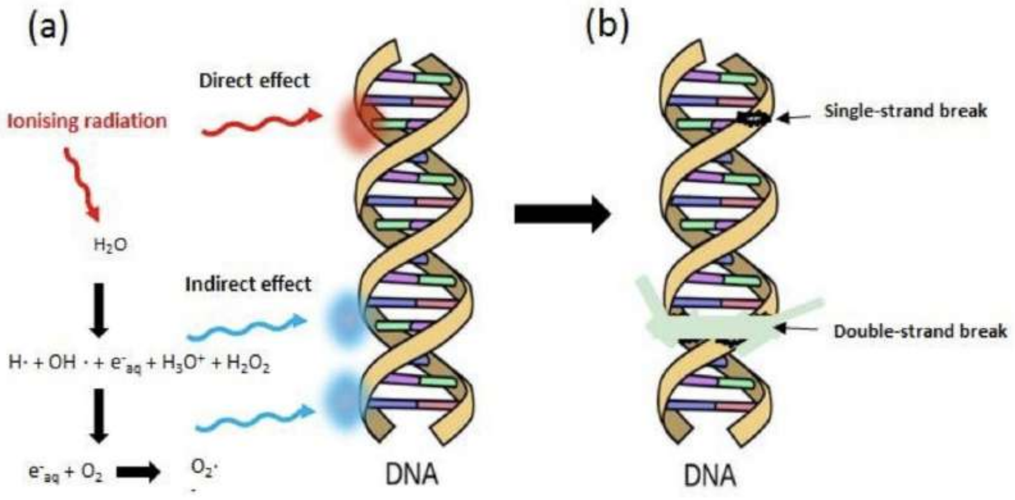

Figure 1.10: (a) Two different ways in which ionising radiation can damage DNA: directly or indirectly through the generation of reactive oxygen species. (b) DNA damage can occur as a result of single-strand breaks, double-strand breaks [21].

depends on different biological and physical parameters. As an example, in which phase of the cell cycle or in which point on the DNA strand the damage occurs.

1.2.2 Survival curve

The survival fraction curve is a function adopted in radiobiology to quantify the biological damage of a given radiation. It can be defined as the fraction of surviving cells that retain their reproductive integrity as a function of the absorbed dose. Conventionally, the survival fraction is plotted on a logarithmic scale on the y-axis against the dose on the x-axis.

There are several models that describes the survival curve; the LQ model is presented by Chadwick and Leenhouts in 1973 [23]. The model is based on the principle that only DSBs in DNA cause cell inactivation and that these can be induced either by a single interaction that damages both strands (single DSB, process 1 in Figure 1.11) or by two separate interactions that are close in time and space (double DSB, process 2 in Figure 1.11). The first process is linear with dose because only a single interaction is required, whereas the second process is quadratic with dose because two interactions are required [19]. According to the LQ model, the survival curve is expressed as:

$$S(D) = e^{-\alpha D - \beta D^2} \tag{1.9}$$

where α and β, represent the intrinsic radiosensitivity of the irradiated cells: cells with a higher α and β are more sensitive to radiation. The first parameter is associated with the first process in Figure 1.11, while the beta parameter is associated with the second process [24].

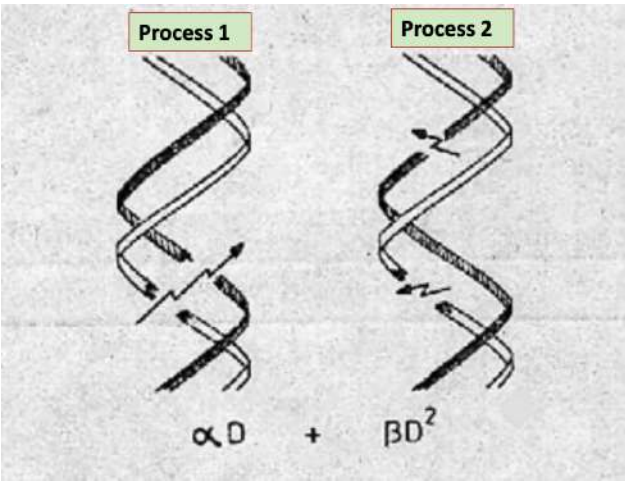

Figure 1.11: DSB can be induced in two different ways. The first consists of both strands breaking in a single interaction and is associated with the parameter α; the second consists of two strands breaking close together in space and time and is associated with the parameter β [19].

In a typical survival fraction curve, the fraction of non-inactivated cells obviously decreases with increasing dose. In particular, the α parameter influences the linear component of the curve: the greater the α, the steeper the curve is initially. The parameter β, on the other hand, is related to the quadratic component of the *S(D)* function: the greater the beta, the greater the shoulder of the curve. These properties are illustrated in Figure 1.12. Important is the $\frac{\alpha}{\beta}$ ratio, which indicates the dose at which the two DNA damage processes have equal weight. The $\frac{\alpha}{\beta}$ ratio is also an index of the radioresistance of the irradiated tissue: tissues characterised by a high $\frac{\alpha}{\beta}$ ratio (> 6) are called “early responding tissues” and are more radiosensitive than “late responding tissues” characterised by a low $\frac{\alpha}{\beta}$ ratio ($\sim 1 \div 4$) [19].

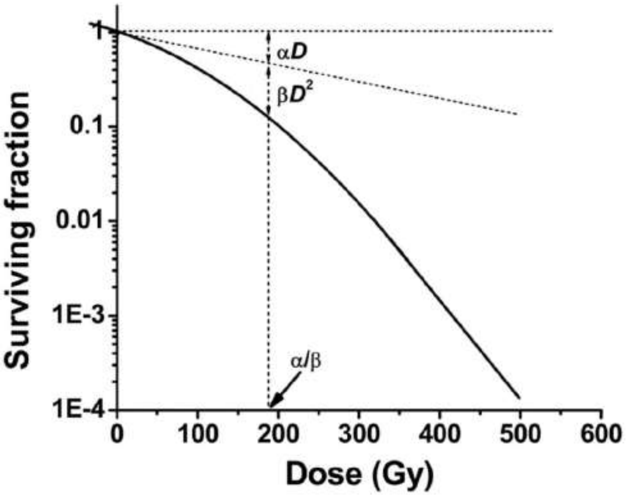

Figure 1.12: Mammalian cell survival curve after low-LET radiation. The curve exhibits a shoulder [25].

1.2.3 LET

A fundamental physical quantity in dosimetry is Linear Energy Transfer (LET) defined as the amount of energy released by ionising radiation in biological tissue due to electron collisions. Very often the LET can be defined associated with a threshold Δ related to the energy of the ionised electrons: a cut-off value expressed in eV:

$$LET_{\Delta} = \frac{dE_{\Delta}}{dx} \tag{1.10}$$

It is expressed in $keV/\mu m$. The addition of a threshold indicates that only electrons that release energy locally are considered, whereas high-energy electrons travel further into the medium and release their energy far away. Low LET ionising radiations are given by photons, electrons and protons ($0.2 \div 2\ keV/\mu m$), while heavy ions are considered as high LET radiation ($50 \div 200\ keV/\mu m$). Protons have low LET because they have $Z = 1$. The higher the Z of the charged particle, the higher the LET, due to the dependence on Z^2 in the Bethe-Bloch equation (Equation 1.3).

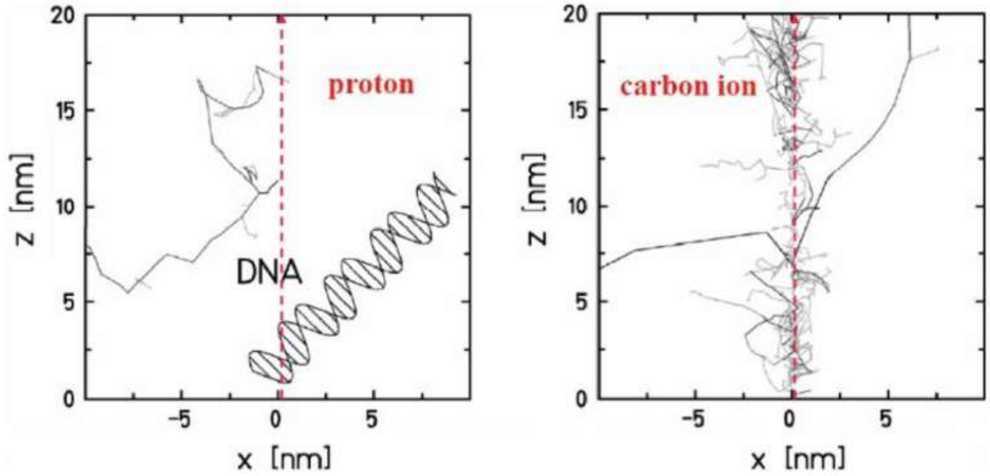

Figure 1.13: Secondary electrons produced by protons and carbon ions with schematic scale representation of DNA. Particles enter at x = 0 and move along the z axis [26].

The LET is directly proportional to the number of ionisations that a charged particle induces per unit length during its path. In the figure 1.13 it can be seen how carbon ions, which have a high LET, produce many ionisations compared to protons. Since the most lethal damage to a cell is the breakage of the DNA strands (which are 2.2 nm apart), high LET radiation is more effective in killing the cell. To illustrate this, in Figure 1.14 the survival fraction curves for X-rays, neutrons and α particles are shown. It can be seen that high LET radiation has a steeper curve because it is more effective at inactivating cells. Indeed, high LET radiation is characterised by a higher α parameter.

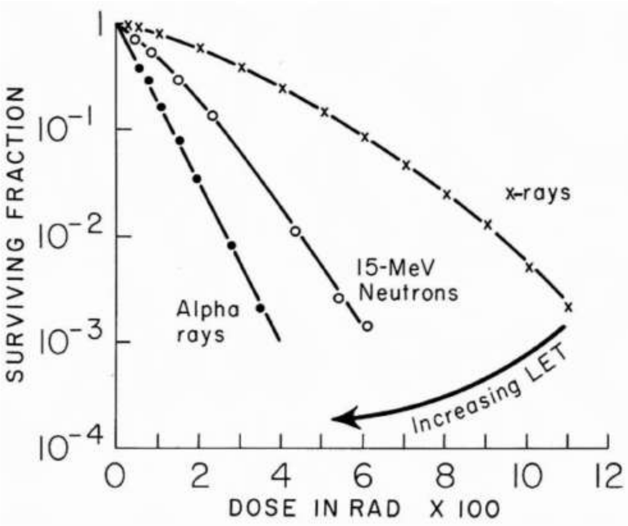

Figure 1.14: Survival curves for cultured cells of human origin exposed to 250 kVp X-rays (LET = 1.3 $keV/\mu m$), 15 MeV neutrons (LET = 70 $keV/\mu m$), and 4 MeV α-particles (LET = 110 $keV/\mu m$). As the LET of the radiation increases, the slope of the survival curve becomes steeper and the size of the initial shoulder becomes smaller [27].

1.2.4 Relative biological effectiveness

The Relative Biological Effectiveness (RBE) was introduced as a parameter to evaluate the radiobiological effectiveness of different beams on different targets. It is defined as the ratio between the absorbed dose for a reference radiation D_{ref} (usually X-rays) relative to the radiation under test D_{test} causing the same biological effect. Mathematically, the definition is as follows:

$$RBE = \frac{D_{ref}}{D_{test}} |_{isoeffect} \tag{1.11}$$

Equal doses of different types of radiation do not produce the same biological effects: for example, 1 Gy of carbon ions produces a greater biological effect than 1 Gy of X-rays under the same conditions. Hadrontherapy takes advantage of the fact that ions have a higher RBE than photons in the energy range used in the clinic, and are therefore able to cause greater biological damage than conventional therapy.

A possible method used to assess the RBE is the survival fraction curve. Given two survival fraction curves for two different types of radiation, the ratio of the doses for a given probability of survival (i.e. to the same biological effect) can be calculated and considered as the RBE. The RBE is a very complex parameter because it depends on many factors: radiation quality (LET), radiation dose, number of dose fractions, cell cycle phase, oxygenation level and dose rate. Indeed, as shown in Figure 1.15, the value of the RBE is different with different values of survival fraction. Normally, the RBE is calculated at a survival rate of 10%.

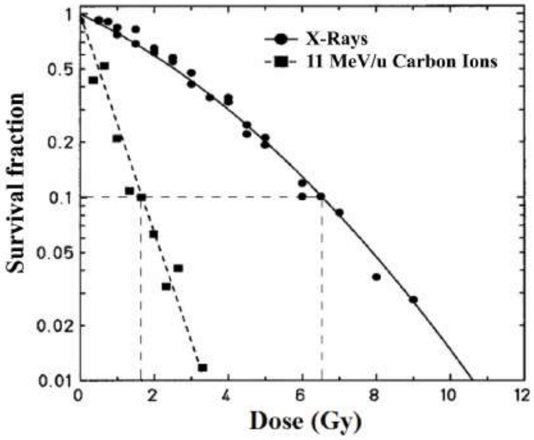

Figure 1.15: Survival curves of Chinese hamster cells (CHO) irradiated with X-rays and carbon ions with an energy of 11 MeV/u. It can be seen that the RBE at the 10% survival level is about 3.5 [28].

Another important aspect of the RBE is its relationship with the LET. If the RBE is plotted as a function of the LET for different types of radiation, it can be seen in Figure 1.16 that there is a maximum around 100 $keV/\mu m$. The figure also shows that the absolute value of the RBE is not unique, but depends on the level of biological damage and therefore on the dose level as mentioned before. As shown in figure 1.17, in this case the average distance between ionisation events corresponds about to the diameter of the DNA double helix (approximately 2 nm). This is optimal for inducing a DSB in the DNA because all the energy released is used to damage DNA. For radiation with LET above 100 $keV/\mu m$, although the probability of breaking the two strands of DNA is relatively high because the average distance

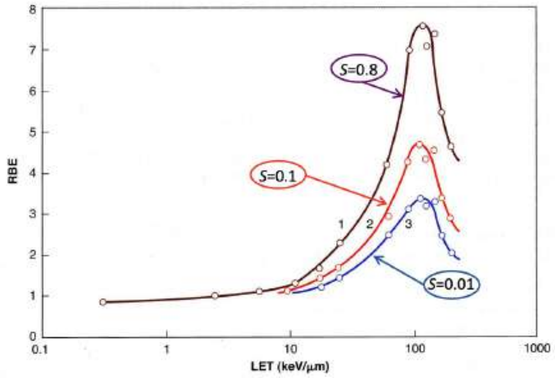

Figure 1.16: Variation of RBE with LET for the survival of mammalian cells of human origin. The RBE increases to a maximum at an LET of about 100 $keV/\mu m$ and then decreases for higher LET values. The brown, red and blue curves refer to cell survival values of 0.8, 0.1 and 0.01, respectively [29].

between one ionisation event and the next is less than 20 nm, some of the energy is lost by the particles without causing any damage. Consequently the RBE decreases after the peak because it is the ratio of two doses to produce the same biological effect; this is commonly referred to as the overkill effect.

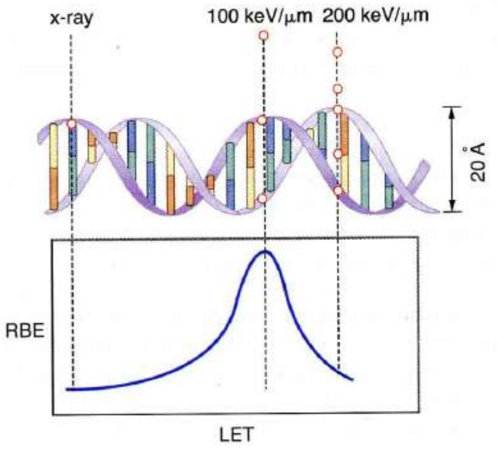

Figure 1.17: Schematic view of the RBE-LET trend with DNA damage [19].

1.2.5 OER

Another important factor influencing the damage caused by ionising radiations is the level of oxygen in biological tissues. Oxygen can increase biological damage at the same dose by competing in reactions with free radicals. Therefore, an environment with low levels of oxygen weakens the effect of ionising radiation. Most tumours are very hypoxic tissues (low oxygen concentration), which makes them much more radioresistant than healthy tissues. The parameter used to quantify the effect of oxygen in tissue is the Oxygen Enhancement Ratio (OER) defined as the ratio between the dose absorbed by a tissue with a given incident radiation in absence ($D_{hypoxic}$) and presence ($D_{aerobic}$) of oxygen to produce the same level of biological damage:

$$OER = \frac{D_{hypoxic}}{D_{aerobic}} |_{isoeffect} \tag{1.12}$$

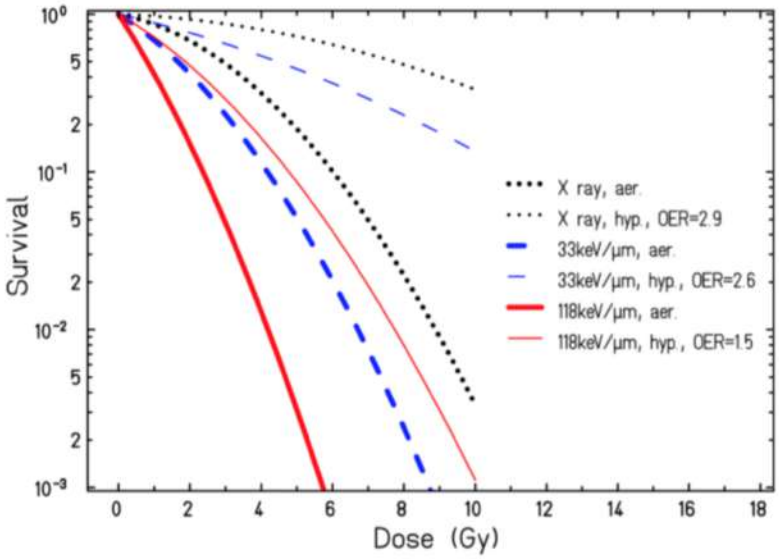

Figure 1.18: Survival curve of human kidney cells as a function of the absorbed dose in the presence of O_2 (thicker line) and under conditions of severe hypoxia (thinner line) for different radiations with different LET values. The influence of the oxygen content for carbon ions at 33 $keV/\mu m$ is shown in blue, at 118 $keV/\mu m$ in red. The variation for X-rays is shown in black [30].

Like the RBE, the OER can be different at different isoeffect levels. For X-rays, the OER is close to 3.5 at high doses ($6 \div 10$ Gy), but can be as low as 2.5 at doses below 2 or 3 Gy. Figure 1.18 shows the influence of the oxygen content on the survival fraction curves for different types of primary radiation, energy and LET [30]. The OER can be evaluated from these curves as the ratio of doses at a given isoeffect level.

For high LET radiation, however, the oxygen effect decreases rapidly to a value of 1 since the oxygen effect is highly dependent on the quality of the radiation. Therefore, one of the advantages of hadrontherapy is that ions, characterised by a high-LET, are more independent of the presence of oxygen and more effective in treating tumours, which are often radioresistant because of hypoxia. In Figure 1.19 the evolution of the OER as a function of LET is shown. Although the oxygen effect is very small at high LET, it is not negligible in hadrontherapy treatments and it must be taken into account during planning.

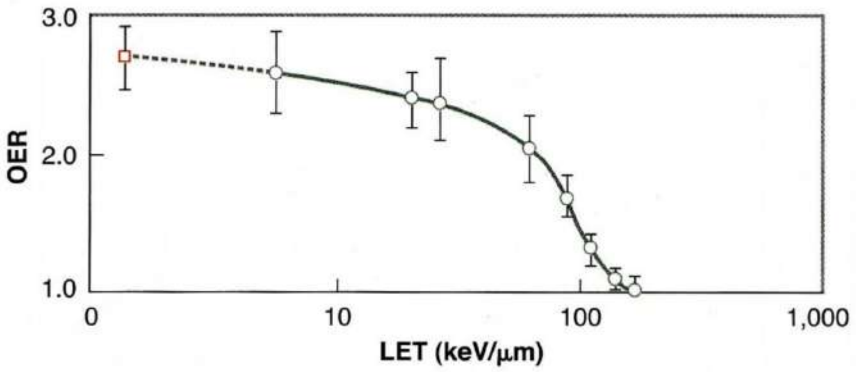

Figure 1.19: OER as a function of LET. Measurements are taken with cultured cells of human origin. Closed circles refer to monoenergetic charged particles, the square to 250 kVp X-rays with an assumed track average LET of 1.3 $keV/\mu m$ [31].

1.3 Range uncertainties

As discussed in Section 1.2, charged particles have different advantages with the respect to X-rays in the treatment of certain solid tumours, especially deep-seated tumours and tumours close to organs at risk (OAR). To ensure that the large amount of dose released in the Bragg peak is actually absorbed by the tumour and not by the healthy tissue, it is necessary to predict very accurately the range of the particles and thus the maximum dose release position. An incorrect estimate of the range can lead to an under dosage of the tumour region and to the detriment of the surrounding healthy tissues. This chapter discusses how range uncertainties are monitored in proton and carbon ion hadrontherapy.

1.3.1 Range monitoring

Hadrontherapy is a high precision technique of cancer treatment and, due to the Bragg peak, is more sensitive to range uncertainties than conventional X-rays therapy. An error in range prediction could result in an under-dose in the tumour region and an over-dose in the healthy tissue, with the risk of affecting the OARs. An example of this situation is shown in Figure 1.20: the red line represents the planned dose, while the green line represents the actual dose delivered. In the figure, there is an under-dose in the pre-tumour region and an over-dose in the post-tumour region; an additional problem is the possible presence of OARs in the vicinity.

For this reason, in hadrontherapy, the range of the incident beam must be predicted very precisely in the Treatment Planning System (TPS); therefore, all sources of range uncertainties must be considered. Range uncertainties have led to the definition of a protocol called ICRU 50, which defines different types of volumes used in the context of a radiotherapy treatment [33]:

- GTV (Gross Tumor Volume): it's the volume of the visible solid tumor as determined by CT;
- CTV (Clinical Target Volume): it's GTV including subclinical microscopic disease;

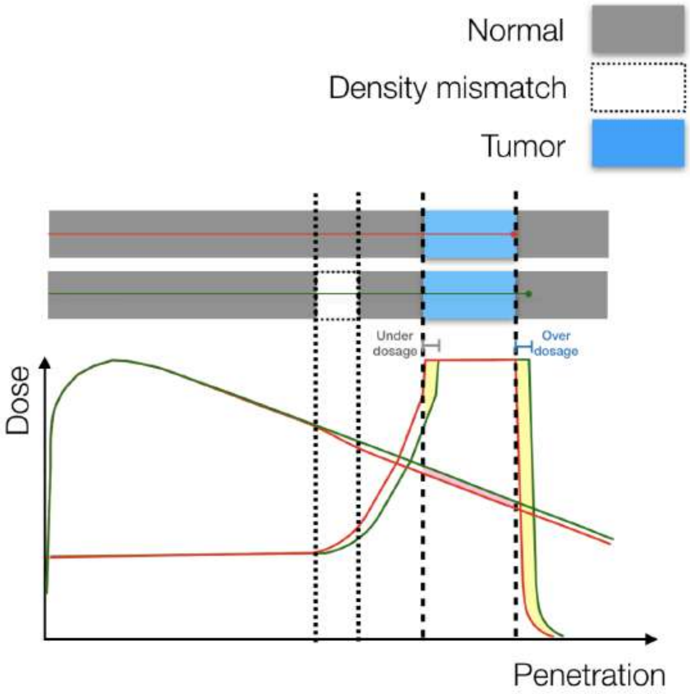

Figure 1.20: Effect of range variation on delivered dose. In red is the line relative to the planned dose (for photons and ^{12}C ions), while in green is the effective dose delivered. A shift in the dose distribution due to a density mismatch (white box) can lead to drastic local dose changes for charged particles (yellow area). On the other hand, the effect in the dose distribution has less impact on photon treatments (pink area representing the difference between the distributions) [32].

- PTV (Planning Target Volume): geometric concept that takes into account all types of geometric variations to ensure that the prescribed dose is delivered to the CTV;
- TV (Treated Volume): the volume supported by an isodose curve that is considered adequate to achieve the treatment goal (often the 95% isodose curve);
- IR (Irradiated Volume): the volume receiving a dose level considered significant for healthy tissue.

The margin between CTV and PTV includes a combination of different uncertainties:

IM (Internal Margins) due to internal movement and SM (Setup Margins) due to setup and instrument uncertainties. Another type of volume can also be defined: ITV (Internal Target Volume), which is defined as CTV + IM, taking into account only internal margins. The purpose of the margins is to increase the volume to be irradiated to ensure that the tumour is hit and that a large dose is released inside the tumour. All the different volumes with the corresponding margins are shown in Figure 1.21.

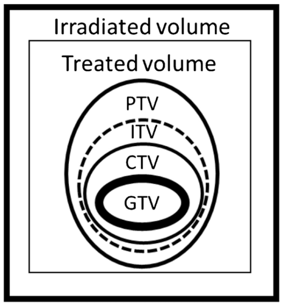

Figure 1.21: Different volumes defined in ICRU 50.

Radiotherapy treatment planning consists of several steps. First, the patient undergoes a CT and/or MRI scan a few days before treatment in order to obtain morphological and anatomical information about the patient. Thanks to these medical imaging examinations, the oncologist is able to identify the different volumes (GTV, PTV, CTV,...). In addition, CT and MRI provide input to the TPS, which designs a complete treatment plan. The TPS has to take into account all the sources of uncertainty that may affect the range of the charged particles, such as: morphological changes in the patient that may occur between the date of acquisition of the CT and the start of the treatment or during the several weeks in which the treatment is carried out, errors in the calibration of the CT, errors in the conversion of Hounsfield Units (HU) to tissue densities, patient mispositioning and finally the inevitable artefacts due to organ motion (such as breathing).

In some cases, a new CT scan is acquired during treatment to check for any morphological changes in the patient. If they significantly change the dose delivery in the patient compared to that planned in the TPS, the treatment is rescheduled. In current clinical practice, the decision whether or not to perform a re-evaluation CT during the course of treatment is only based on the clinical history of the particular pathology treated, ignoring the actual condition of the examined patient. For this reason, a range monitoring technique is needed to detect any morphological differences in the patient to help the clinician assess the need for a re-evaluation CT. The aim is to have a method that is based only on the specific characteristics of each patient and allows the performing of the re-evaluation CT only when necessary. There are two different monitoring methods: in the first case the range of the primary particles and therefore the occurrence of morphological changes is assessed by comparing one treatment fraction with another. It's called Inter-fractional monitoring. The second one is the On-line monitoring: the range is monitored during the treatment and if a consistent morphological variation is detected, the beam delivery is immediately interrupted. This is the ultimate goal of all scientific research into the monitoring of hadrontherapy treatments.

As the primary beam enters and remains within the patient, an approach of range monitoring use the secondary or tertiary particles produced by the interaction of the primary beam with the target, which have sufficient energy to leave the patient. These can include:

- $\beta+$ emitters: positrons generated by the β^+ decay of products of projectile-target interactions can be tracked as they annihilate with electrons to produce two 511 keV gamma photons emitted in opposite directions. These photons can be detected by Positron Emission Tomography (PET) scanners.

- Prompt gamma: the primary beam excites the target nuclei through nuclear interactions; the nuclei then decay rapidly ($\approx ns$), releasing prompt photons with energies up to 10 MeV.

- Charged fragments: are produced by nuclear fragmentation of the primary beam particles when the projectiles are light ions with $Z > 1$.

- Neutrons: are generated by nuclear interactions between the primary beam and the target [34, 35].

1.3.2 Range monitoring in hadrontherapy with protons

In proton hadrontherapy, the most commonly used range monitoring techniques are based on $\beta+$ emitters and prompt-γ because the projectile particles cannot be fragmented; this chapter discusses both methods of proton range monitoring. The production of $\beta+$ isotopes in proton hadrontherapy results either from target fragmentation or from excitation reactions induced by the interaction between the projectiles and the target. The radiation produced by $\beta+$ decay can be detected by PET scanners, which reconstruct the distribution of radioactive isotopes in the patient. Figure 1.22 shows that the activity of the $\beta+$ emitters correlates with the dose delivered to the patient and therefore with the proton range. In particular, the activity is very high along the entire path taken by the proton until it reaches a maximum just before the Bragg peak and then disappears rapidly at the peak.

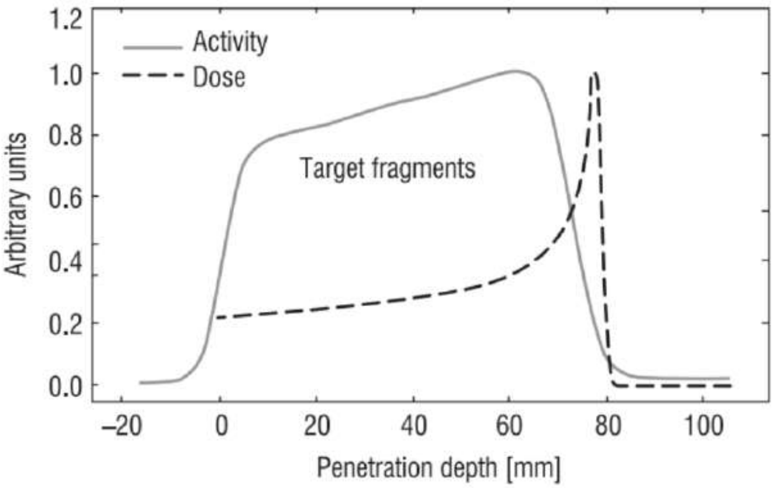

Figure 1.22: Activity and dose distribution of $\beta+$ as a function of penetration depth in PMMA target irradiated with 110 MeV protons [36].

The range monitoring based on $\beta+$ emitters is divided into different modalities:

- Offline monitoring: the patient physically moves to another room after treatment, where $\beta+$ detection takes place [37, 38, 39, 40]. However, this method is strongly limited by the metabolic washout. It is a biological effect due to the human metabolism expelling waste substances from the body. For this reason, the number of isotopes present along the beam path decreases and therefore much of the detection signal is lost by the time the patient physically moves into the room where the PET scanners are located. Metabolic washout also reduces the correlation between absorbed dose and isotope activity distribution.

- In-room monitoring: in this case, the $\beta+$ detection system is located directly in the treatment room [40]. In particular, after treatment, the patient's bed is automatically moved into the PET scan position. Despite the reduction of the time interval between treatment and photon detection, the problem of metabolic washout is not solved, but only attenuated. Moreover, no more patients can be treated during the photon detection phase, which drastically slows down the clinical workflow.

- In-beam monitoring: in this method, the PET detection system is integrated with the beam delivery system to detect the $\beta+$ emitted during and immediately after treatment. Figure 1.23 shows the $\beta+$ activity as a function of time, where $t < 0$ is the time interval during which the patient is treated. It can be seen that the activity increases throughout the treatment, peaks at $t = 0$ (end of treatment) and then decreases due to washout and decay. This monitoring technique solves the problem of metabolic washout. However, new problems arise: detection is affected by a large background as it occurs during treatment. There is also the problem of integrating the monitoring system into the treatment's room.

Nowadays, many facilities around the world are using or developing technical solutions for in-beam PET: Gesellschaft fur Schwerioneneforschung (GSI), Darmstadt, Germany [42, 43]; the Heavy Ion Medical Accelerator (HIMAC) in Chiba, Japan [44]; the CATANA Proton Therapy Center in Catana, Italy [45]; and the National Cancer Center (NCC), Kashiwa, Japan [46]. Positive and promising results have also been obtained by the INSIDE project (INnovative Solutions for In-beam DosimEtry

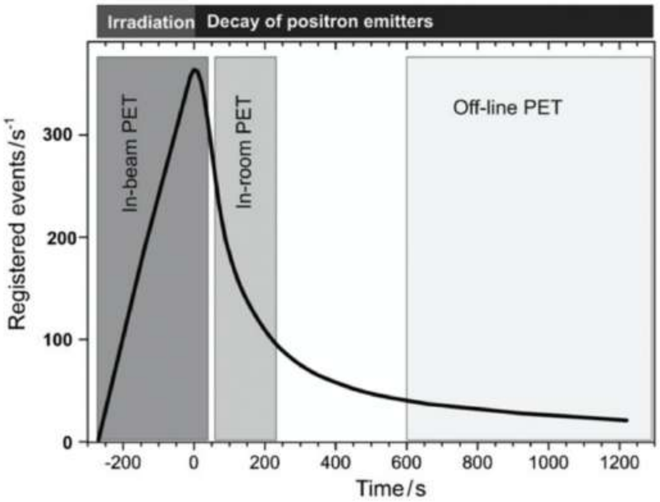

Figure 1.23: Event rate distribution as a function of time in the detection of $\beta+$ during a carbon ion treatment at GSI, where $t = 0$ is the end of the treatment; the time intervals in which the three detection modes operate are shown [41].

in hadrontherapy) [47], founded by the INFN, Centro Fermi and the Universities of Turin, Milan, Pisa and Rome. The project has developed a PET system consisting of two PET heads installed at CNAO; the usual ring is not allowed in the treatment room due to its bulkiness.

The other strategy for range control in proton hadrontherapy is the use of prompt-γ. The primary beam interacting with the medium excites the target nuclei, which decay with typical nuclear de-excitation times ($10^{-16} \div 10^{-12}$ s), releasing prompt-γ with an energy spectrum of $1 \div 10$ MeV [48, 49]. Figure 1.24 shows the correlation between the prompt-γ emission distribution and the absorbed dose. The fall-off of the prompt-γ distribution is close to the Bragg peak.

This method has both advantages and disadvantages compared to the use of $\beta+$: due to the typical short nuclear de-excitation times, prompt-γ detection is not affected by metabolic washout. Another advantage is that, unlike $\beta+$ detection, prompts-γ are released isotropically and each photon is released independently, so that a whole ring is not required for detection. A disadvantage of this method, however, is that the wide energy spectrum of the prompt-γ does not allow standard

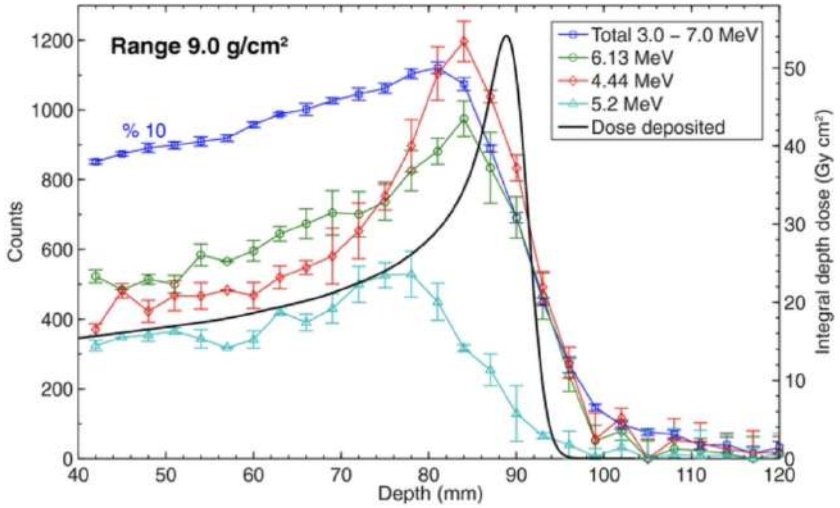

Figure 1.24: Energy-integrated (□) and discrete (○, ◇, △) prompt-γ emissions along the path of a proton pencil-beam in water with a range of 9.0 gcm^{-2}. The lines connecting the points serve to guide the eye. The dose deposited by the protons is shown for reference in black, which is based on the clinically commissioned depth-dose curve [50].

SPECT (Single Photon Emission Computed Tomography) to be used, as heavier and bulkier absorbers are required, with consequent encumbrance and weight limitations, loss of efficiency and spatial resolution. Another problem with this method is the fact that in addition to prompt-γ, uncorrelated neutrons and photons are also produced with the primary beam; in particular, neutrons contribute significantly to the background in the detection, thus reducing the spatial resolution. To overcome these problems of prompt-γ detection, three different detection methods have been proposed:

- Mechanical collimation: the idea is to use mechanical collimation imaging systems with pinholes, linear slits or multiple slits, between the patient and the detector in order to reduce the background, to measure the proton range with a resolution on the order of millimetres [51]. This system is actually implemented.

- Compton Cameras (CC): the principle of this method is to reconstruct the trajectory of the incoming photon by measuring the Compton scattering interaction that takes place in the detector [52]. The detector consists of two parts: the scatterer, where the Compton scattering of the incoming photon takes place, and the absorber, where the scattered photon is absorbed. This reconstructs the point of emission of the photon, providing 3D information and avoiding the background contribution due to neutrons. However, the detection and reconstruction process is more complex with the respect to the other methods.

- Non-imaging systems: these methods are based on the Time-Of-Flight (TOF) of the protons in the primary beam or based on the prompt-γ energy spectrum measurements. Prompt Gamma Timing (PGT) is an approach that uses the TOF in order to reconstruct the position of the Bragg peak. Simulations have demonstrated the feasibility of this method, showing a correlation between the primary beam energy (depth of the Bragg peak) and the measured time-of-flight of the prompt-γ.

1.3.3 Range monitoring in hadrontherapy with carbon ions

In addition to the two previously described methods using $\beta+$ and prompt-γ emission, the production of secondary charged fragments in carbon ion treatments can be used for range monitoring, since the projectiles are charged ions with $Z > 1$. Secondary fragments are also produced in proton hadrontherapy due to nuclear fragmentation of the target nuclei. However, detection of them in proton treatments is not feasible because the charged fragments have a kinetic energy of at most a few MeV and a range on the order of micrometres, not enough to escape from the patient and therefore cannot be detected.

On the other hand, the secondaries produced by the fragmentation of heavy ion beams, used in carbon ion treatments, can have velocities comparable to those of the primary beam. Their energy can exceed 100 MeV and therefore have a range sufficient to pass through the patient's body, allowing detection and tracking.

However, some of them will still stop in the patient and not reach the detector. This re-absorption phenomenon is a problem for the monitoring of secondary charged fragments, as it reduces the efficiency of their detection.

In addition, although the preferred direction of secondary fragments is the forward direction, in carbon ion treatments a non-negligible fraction of them (mostly neutrons and protons) can also be detected at much wider angles (60-90°). Charged particles (in this case protons) and neutrons are very easy to distinguish. For this reason, the low background is definitely one of the advantages of this monitoring technique.

Figure 1.25 shows the emission curves of secondary fragments obtained experimentally at GSI using carbon ion beam with an energy of 400 MeV/u in a 35 cm water phantom [53]. The curves show that the production of secondaries increases with the depth of penetration of the beam, with a maximum at the Bragg peak. Protons are the most produced fragments and they are the only ones that show a significant emission at angles greater than 10°.

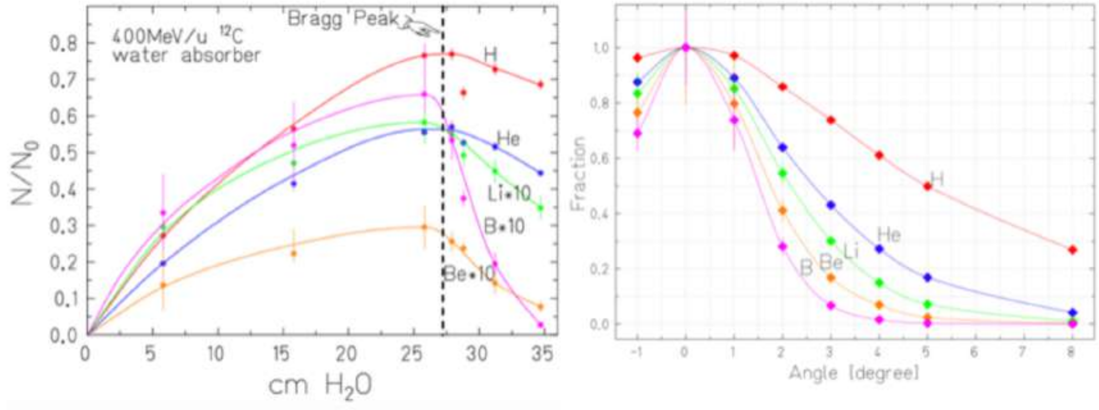

Figure 1.25: Left: fraction of secondary fragments produced by a 400 MeV/u carbon ion beam in a water phantom as a function of depth. Right: relative angular distribution of secondary fragments under the same conditions. To improve readability, the values for Li, B, Be are multiplied by a factor of 10 [53].

Since there is a correlation between the emission intensity of the secondary fragments and the position of the Bragg peak, the idea of using secondary charged fragments can be adopted for range monitoring purposes. In order to verify the feasibility of an on-line monitoring of the treatment, measurements of the flux of charged secondary particles produced by hadron beams were carried out at GSI [54, 55], LNS (Southern National Laboratories) [56] and HIT (Heidelberg Ion Therapy Center) [57]. All of them used a carbon ion beams with energies between 80 MeV/u and 220 MeV/u and used an almost identical experimental setup as shown in Figure 1.26: a 12-plane wire Drift Chamber (DC) was used to reconstruct the trace of charged fragments coming out from the PMMA target. An array of 4 LYSO crystals, each measuring 1.5 x 1.5 x 12 cm^2, was used to measure the energy of the secondaries. All experiments were simulated using a Monte Carlo software to determine the efficiency and the geometric acceptance.

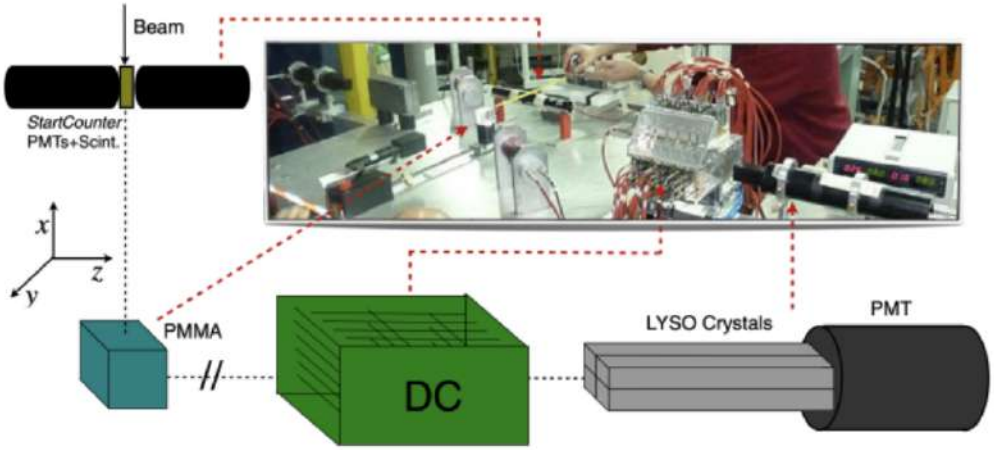

Figure 1.26: Schematic view of the experimental setup used for the measurements of the flux of charged secondary particles produced from the interaction of a 80 MeV/u fully stripped carbon ion beam with a poly-methyl methacrylate target performed at the LNS [56].

The emission profile along the beam axis (x_{PMMA}) of the secondary protons is obtained by back-tracking the detected particles with the DC. It is shown in Figure 1.27 with, superimposed, the profile of the dose released in the target, reconstructed by means of Monte Carlo simulations. The two profiles are anti-correlated [54]. This can be explained by the fact that, corresponding to the first mm of the target, the $\frac{dE}{dx}$ of the particles of the primary beam is small and therefore the dose absorbed by the target is also small. In addition, in the first *mm* of the target, the secondary fragments produced in the entry region have higher energy with the respect to the particles produced close to the Bragg peak, enough to exit the patient and reach the detector. As the depth increases, the primary beam loses energy and the contribution to the emission profile of the charged secondary fragments is significantly reduced. Therefore, most of the reconstructed particles come from the surface of the PMMA target where the absorbed dose is minimal. The intrinsic limit of a monitoring system based on the detection of secondary charged fragments is the lack of statistics in depth makes this technique not very sensitive to deep dose variations. Other disadvantages that affect the spatial resolution are the multiple Coulomb scattering described in Section 1.1.4 and the re-absorption phenomenon described above.

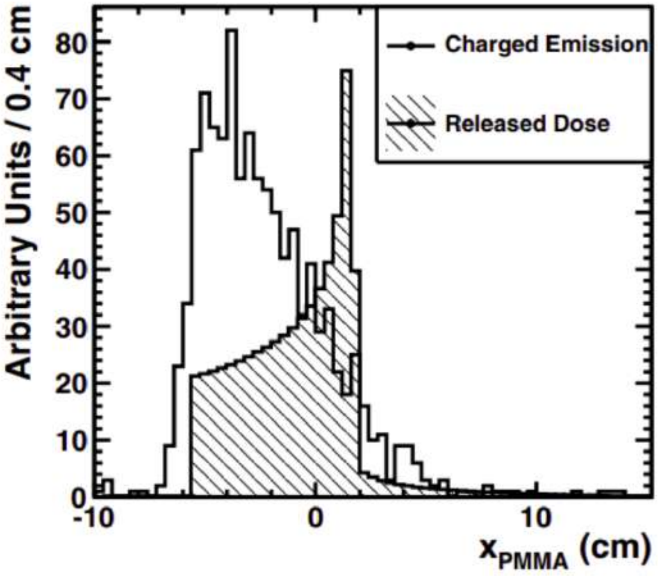

Figure 1.27: Profile of secondary fragments as a function of the penetration in a PMMA target. The absorbed dose profile obtained with MC simulation is superimposed [54].

As explained previously, the variation in density along the beam direction is mainly responsible for the change in the released dose profile. Figure 1.28, shows the correlation between target location and secondary charged fragment production points. Indeed, it can be seen that the peaks associated with the production of secondaries occur in the same distances where the PMMA target is present.

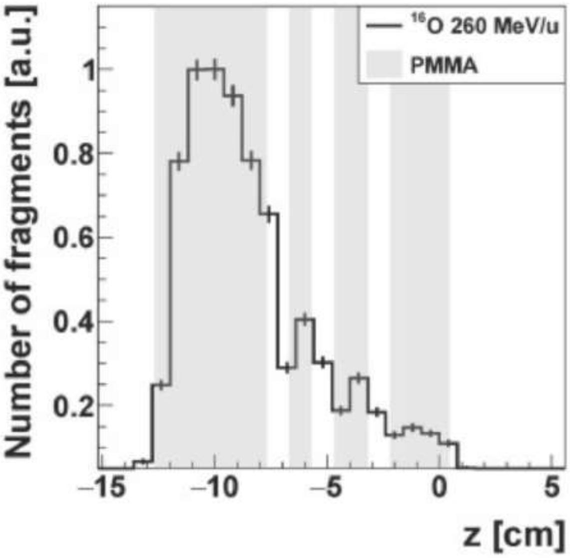

Figure 1.28: Charged secondary emission profile produced irradiating a non homogeneous PMMA phantom with ^{16}O beam with energy 260 MeV/u [57].

Chapter 2

Dose Profiler

The INSIDE (INnovative Solution for In-beam DosimEtry in hadrontherapy) project was born with the aim of developing a range monitoring technique for carbon ion treatments capable of detecting morphological variations within the patient by exploiting the emission profiles of charged fragments. Indeed, any morphological variation along the beam path can lead to a shift in the range of the primaries. Unfortunately, this results in a different release of the dose than that planned by the TPS, damaging healthy tissue and sparing tumour tissues. This effect can be spotted by means of range monitoring technique by measuring the emission profiles of the secondary charged fragments using the Dose Profiler (DP). The aim of the DP is to develop a patient-specific technique that can assist radiotherapists in deciding whether or not to perform an additional re-evaluation CT to adjust the therapy. In this way, additional dose could be avoided in all patients for whom a re-evaluation CT is not necessary, or treatment could be re-planned in patients with diseases for which the clinical history does not predict morphological changes.

In this chapter, the DP will be described [58, 59, 60]: the charged particle detector developed in the INSIDE project and designed to monitor the range of the carbon ion beam in hadrontherapy treatments. The DP is installed in the treatment room n.1 of the CNAO in Pavia, Italy.

In my thesis I studied the feasibility of an inter-fractional 3D monitoring of carbon ion treatments using emission profiles of secondary charged fragments collected during the INSIDE clinical trial at CNAO. In particular, I studied the differences in the 3D emission profiles collected in successive fractions of carbon ion treatments using the gamma index test described in section 2.5. To study the performance of this innovative range monitoring method, a number of patients were simulated using the Monte Carlo method and the emission maps of the charged fragments were reconstructed using a chain of steps described in section 2.6. In this chapter the workflow of the clinical trial is also discussed and a detailed overview of all patients is presented 2.3.2.

2.1 The INSIDE system

The INSIDE system was proposed in 2013 [61] with the aim of monitoring the range of the primary beam (protons and carbon ions) during hadrontherapy treatments by exploiting the interactions of the primary beam with human tissues. The innovative INSIDE system is bimodal, i.e. it consists of an in-beam Positron Emission Tomography (PET) scanner to detect the annihilation photons emitted by positron emitters during protontherapy, and a charged particle detector (DP) to detect the charged fragments produced during carbon ion treatments.

The INSIDE project has been developed by the Universities of Turin, Pisa, Sapienza of Rome and the Polytechnic University of Bari, funded by the Ministry of Universities and Research (MIUR), with the contribution of the Fermi Centre, the National Institute for Nuclear Physics (INFN) and the CNAO. The DP and the PET heads are positioned on a cart of aluminium alloy profiles, shown in light blue in Figure 2.1. The whole system weighs about 300 kg and has dimensions of 110 cm (L) x 110 cm (W) x 160 cm (H).

The two PET heads of the INSIDE system were installed at CNAO in 2016 and tested in-vivo, successfully monitoring two consecutive proton treatments on the 1^{st} and 2^{nd} of December 2016 [62]. Instead, the DP was tested in 2017 and installed on the cart in September 2018.

In July 2019, a clinical trial with the bimodal INSIDE system has started at the CNAO. Patients with head and neck and brain cancer treated with both protons and carbon ions were included in the study. The aim of the clinical study was to evaluate the performance of the INSIDE system in a clinical setting.

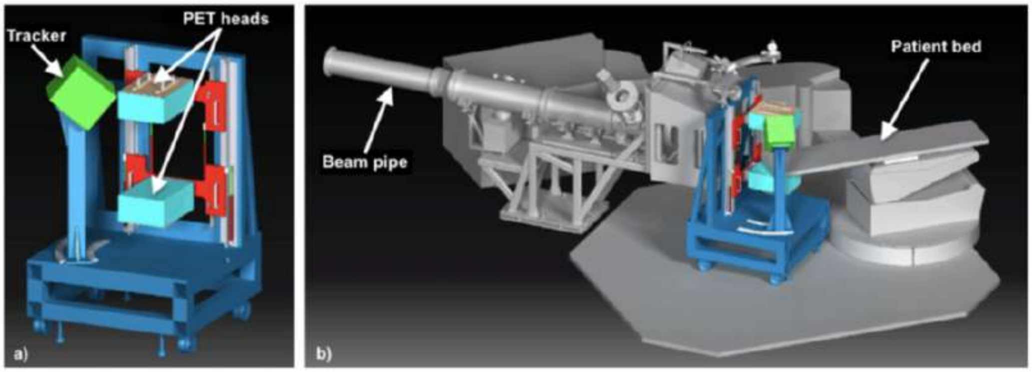

Figure 2.1: Schematic view of the INSIDE bimodal system: a) mechanical details of the carriage to which the PET heads and the DP are fixed. b) View of the treatment room n.1 of the CNAO with the INSIDE cart in its operating position

2.2 Experimental setup

The DP was designed and built at the SBAI (Basic and Applied Sciences for Engineering) department of the Sapienza University of Rome. It was designed to be highly efficient in detecting protons in the energy range 50÷200 MeV and to have a large angular acceptance to maximise the number of charged fragments detected. It can also sustain a fragment detection rate of the order of a few hundred kHz (typical particle production rates in a carbon ion treatment in the DP angular acceptance) [60].

2.2.1 Dose Profiler layout

The DP is a detector consisting of eight planes of squared plastic scintillating fibres, each with an area of 19.2 x 19.2 cm^2; each plane consists of two orthogonal layers of 384 fibres each. This arrangement allows the reconstruction of the path of the charged particle inside the detector in 3D. The distance between the planes is 2 cm, which results in a very compact system, compatible with the limited space available in the clinical room, while guaranteeing a good geometric acceptance of the DP (~ 0.1 sr). A schematic representation of the DP is shown in Figure 2.2.

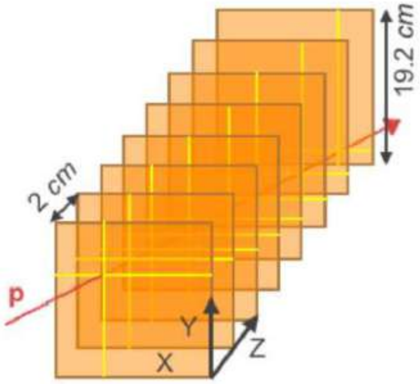

Figure 2.2: Scheme of the principle of working of the DP; the proton (red arrow) crosses all 8 planes of scintillating fibers emitting light-signals [60].

The fibres used are multi-cladding BCF-12 and represent a compromise between the minimization of the amount of scintillating material crossed by the particle, and the amplitude of the signal generated by the fibres. The fibres, with a cross-section of 500 x 500 μm^2, are composed of a polystyrene base and a double layer of PMMA and guarantee a capture efficiency of 7.3%.

Figure 2 shows the photo of the DP in the assembly stage. The detector is enclosed in a light-tight box consisting of four aluminium panels along each surface and a 50 μm thick Tedlar layer on the entrance side, which is able to maintain darkness with a thin layer that limits the energy loss of the fragments at the detector entrance. The total volume of the detector, including the readout system, is $\sim$ 30 x 30 x 30 cm^3. This ensures easy integration into the treatment room.

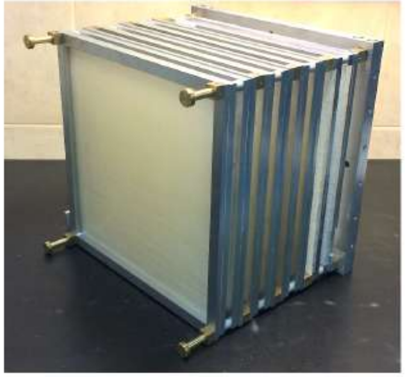

Figure 2.3: View of the DP during the assembly phase. The eight layers of scintillating fibres can be distinguished, fixed to an aluminum frame [60].

2.2.2 INSIDE In-beam PET and integration with DP

The INSIDE in-beam PET system was built in Turin in 2015 and commissioned at the CNAO synchrotron facility. It consists of a two-head PET system with a planar geometry. This configuration degrades the acquired images compared to a full-ring system, but allows easier integration in the treatment room, which is one of the critical points for online operation in the clinical setting.

The PET system and the DP are installed on a mobile cart in the treatment room n.1 of the CNAO facility. During irradiation, the PET heads are positioned above and below the patient's bed at a distance of 60 cm symmetrically to the isocentre of the room. The positions of the patient and of the bed limit how close the DP can be to the patient during data acquisition: in operating position it is fixedly placed approximately $\sim$ 50 cm from the treatment room isocentre, at an angle of 60 degrees with respect to the beam direction and 30 degrees upward, rotating around the plane perpendicular to the incoming beam direction.

2.2.3 Read-out and DAQ system

The read-out and data acquisition system of the DP consists of e-readers with a hierarchical structure. Specifically, silicon photomultipliers (SiPM, 12571-050P Hamamatsu) with a cross section of 1 x 1 mm^2 and a spatial resolution of the order of 300 μm were used for read-out; Table 2.1 shows the other basic technical specifications.

Breakdown Voltage [V]	65 ± 10
Peak sensitivity length [nm]	450
Photon detection efficiency [%]	35
Gain (at 25°C)	$1.25 \cdot 10^6$
Dark count rate [kHz]	100
Number of pixels	400

Table 2.1: Technical characteristics of the SiPM (12571-050P Hamamatsu).

Each SiPM is coupled with two adjacent fibres, each with a side dimension of 0.5 mm. Read-out of successive fibre pairs is performed on opposite sides to optimise SiPM positioning. Figure 2.4 shows the coupling between the fibres and the SiPMs: they are mounted on rectangular boards formed by two parallel rows of 96 SiPM each. There is a dead space of 1 mm between one SiPM and the next one and in order to read all the fibres correctly, there is a shift of the same distance between the upper and lower boards. The read-out of two adjacent planes requires a set of four boards (a unit called a biplane), and to cover the entire detector 16 boards are required, for a total of 3072 read-out channels.

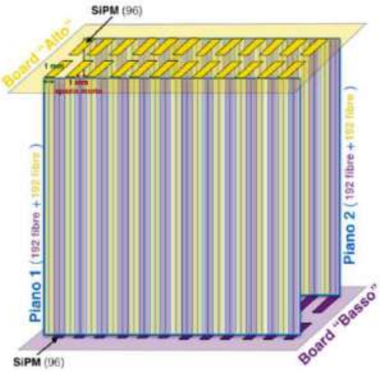

Figure 2.4: Schematic representation of the SiPM reading system: the 1 mm offset between the pair of boards, used to compensate for the dead space between two successive photomultipliers is shown; the SiPMs of the "high" board are shown in yellow, the ones of the "low" board in purple.

The control and read-out of the SiPMs is performed by a custom integrated circuit in CMOS technology (ASIC) suitable for medical imaging applications. Figure 2.5 shows the six 32-channel ASICs on the front-end boards.

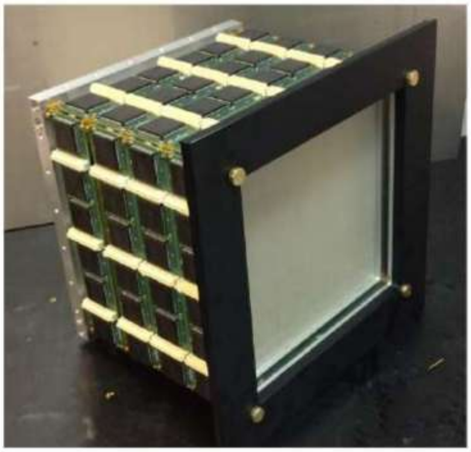

Figure 2.5: Photo of the DP showing the six BASIC32_ADC for each front-end board. A total of 96 ASICs are required to read the 3072 channels.

The ASICs boards communicate with the central data acquisition system via 16 FPGAs (Field Programmable Gate Arrays), which are software programmable integrated circuits located on a control board (Figure 2.6) that also contains a temperature sensor and a removable power supply for the SiPMs.

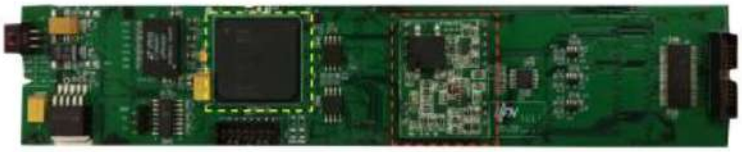

Figure 2.6: Board with FPGA (yellow) and SiPM power supply module (red) highlighted.

The CONCENTRATOR, an other board located at the rear of the detector, collects the data from the FPGAs boards and is responsible for generating a trigger signal that transfers the data, temporarily stored in the ASICs, to the data acquisition server via an Ethernet connection. The CONCENTRATOR also interacts with CNAO's Dose Delivery System (DDS). Indeed, by exploiting the link with the DDS, it is possible, during treatment delivery, to acquire the nominal position targeted by the primary beam, thus verifying its accuracy. In addition, the DDS makes it possible to link the data collected on each pencil beam, knowing the energy, direction, position and number of particles associated with the pencil beam itself. Specifically, the DDS treatment room consists of five ionisation chambers that continuously provide information on the intensity and position in the transverse plane (x,y) of the delivered pencil beam [63]. The collected charge is then converted into a digital signal by the front-end electronics, which then sends the data to a high-speed acquisition system that monitors the treatment. This information is used by the DP in the reconstruction phase to track the secondary charges detected.

In order to optimise the signal-to-noise ratio of the SiPMs, there is a 2 cm thick aluminium plate inside the detector, in which there is a water-crossed coil, kept at a temperature of 12$°C$ by a cooling device (Julabo F250). The technical characteristics are given in Table 2.2.

Working temperature range [$°C$]	(-10) ÷ (+40)
Temperature stability [$°C$]	± 0.5
Temperature control	digital
Cooling capacity: +15°C +10°C	 240 W 220 W

Table 2.2: Technical characteristics of the Julabo cooler F250.

By controlling the temperature of the SiPM, high detection efficiency is achieved, reducing electronic noise that could compromise trace reconstruction by increasing the combinatorial background. When the electronics are fully enabled, the total power dissipation is approximately 100 $Watts$. A summary diagram of the above readout connections is shown in Figure 2.7. Detected events can be transferred to an external computer for processing and storage via the Ethernet connection. The DP has been designed with two different trigger logics: in the first case, an external input is used to activate the read-out boards (external trigger); in the second case, the discrimination between an event of interest or not is performed by the detector's internal logic combining the information from each BASIC (internal trigger).

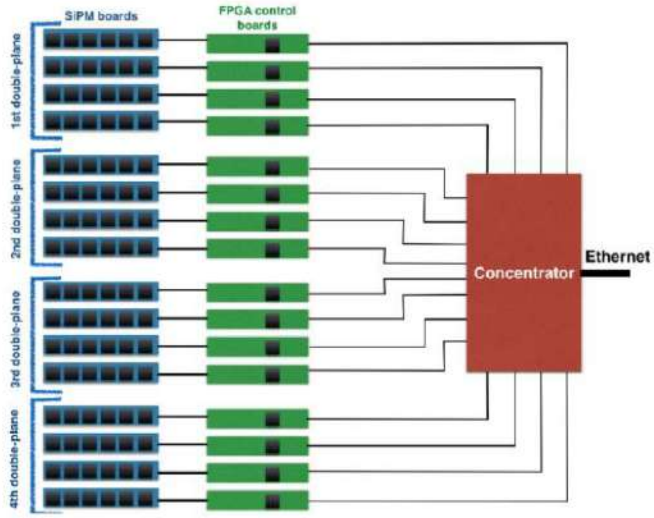

Figure 2.7: Overview diagram of the DP readout electronics.

The latter trigger logic is shown schematically in Figure 2.8: the elementary trigger unit requires at least one SiPM in both of the x-y of a biplanes is above threshold (OR) in both directions of view (AND). Finally, the selection of a charged particle passing through the detector takes place only if a signal comes from all the four biplanes (AND) in a time window of 50 ns. The BASIC reading then begins: during the beam in-spill phase, the data is temporarily stored in the CONCENTRATOR's memory. The transfer to the external workstation takes place in the interval between two spills (duration 2 s), in order to reduce the contribution of dead time due to transmission via Ethernet cable. Once triggered, the CONCENTRATOR acquires the data and transfers them to the external PC equipped with a data acquisition software developed in C++ using the ROOT libraries [64].

The various phases of a data acquisition session follow a protocol that includes an initial calibration of the instrument through measurements taken in the absence of a signal and the verification of the operation of all the channels. Once the correct functioning of the instrument has been verified, the actual data acquisition begins.

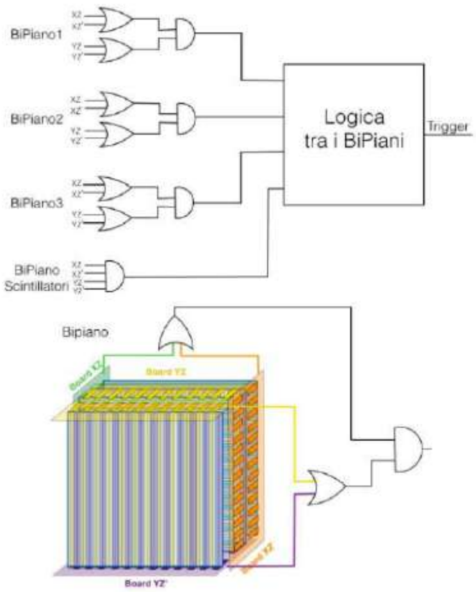

Figure 2.8: Schematic view of the internal trigger logic: there is an OR logic port for each pair of planes along the same direction, followed by an AND port that requires a signal from the biplane unit along both x and y, and finally the trigger is issued when a signal is received from all 4 units in a time window of 50 ns. Below is a schematic of the logic associated with the single biplane unit.

2.2.4 Rate capability and Dead Time

One factor that must be kept under control during data acquisition and analysis is the dead time (DT) of the detector: the time interval during which the detector processes the acquired data and is unable to collect new data. So a larger dead time leads to more loss of measurements and therefore a reduction in statistics.

During the characterisation phase of the detector, tests were carried out on the acquisition rate and the resulting DT under clinical conditions. Specifically, a carbon ion beam related to the treatment plan of a patient treated at CNAO was sent to an anthropomorphic target. The particle accelerator at CNAO is capable of delivering up to $\sim 10^8$ particles per single burst. After ion beam was delivered, a maximum DAQ rate value of ~ 150 kHz was obtained. In particular, the trend of the DAQ rate is shown in the right-hand graph in Figure 2.9. The rate of events collected during a treatment depends on the performance of the CNAO accelerator, which varies slightly from day to day.

Once the trigger is fired by the passage of a charged particle through the DP, the dead time of the detector is mainly due to the ASIC readout chain. During these tests, the DT was measured using a counter (100 MHz frequency) inserted in the CONCENTRATOR. The result is shown in the graph on the left of Figure 2.9, which shows the dead time distribution obtained, with a mean value of $\sim 4\ \mu s$.

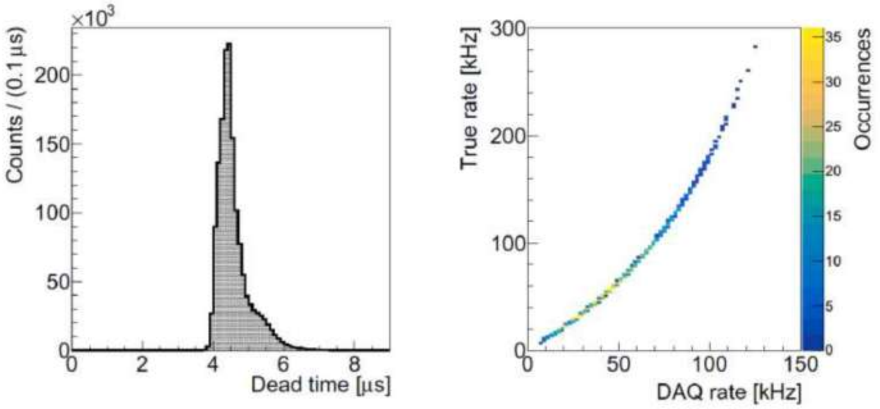

Figure 2.9: Distribution of the measured dead time for each event (left), and the true rate obtained by applying the correction to the DAQ rate (right) [60].

The true rate was derived by applying the correction given in Equation 2.1, where $\bar{\tau} = 4\ \mu s$ was considered. This gives a corrected rate which peaks at $\sim 300\ kHz$.

$$r_{true} = \frac{r_{DAQ}}{1 - (r_{DAQ} \cdot \bar{\tau})} \tag{2.1}$$

2.3 INSIDE clinical trial

In July 2019, the DP was installed and tested in treatment room n.1 of the CNAO, in order to characterise and evaluate its performances. The second phase of the INSIDE project started in August 2019 with the beginning of the first clinical trial. The aim of the trial was to verify the efficacy and sensitivity of the INSIDE system in detecting morphological changes during treatments. As explained in this chapter previously, changes in the density of the tissues crossed by the beam can result in a variation of the dose release profile compared to that planned by the TPS.

Two different patient groups were selected in the trial: the first group consisted of patients whose pathology did not predict the occurrence of morphological changes during treatment, making them suitable for assessing the sensitivity of the technique to identify false positives. Patients in the second group were expected to experience morphological variations during the whole treatment. This second group of patients was selected to test the sensitivity of the technique in identifying density changes in tissues crossed by the beam. In this second case, the absorbed dose may be significantly different from that planned during TPS, leading to a lower treatment efficiency and an increased risk to damage the healthy tissues.

2.3.1 Clinical workflow

The clinical-therapeutic protocol that the patient must follow in order to access treatment at the CNAO involves several stages. Once the patient has been enrolled, the treatment simulation phase begins, during which the immobilisation devices (thermoplastic masks and pillows) are selected and tailored for each patient to ensure correct positioning and to minimise movements during the whole irradiation. Next, CT and MRI scans of the patient wearing the personalised devices are acquired in order to localise the tumour and identify any organs at risk (OARs). The CT is also used as input to the TPS, which builds a treatment plan in accordance with the dose constraints provided by the physician. The treatment begins 1-2 weeks after the performed scans. The timing of the hadrontherapy treatment given to the patient depends on the particle used, which is determined by the medical team during the planning step:

- Carbon ions: 4 days per week up to 4 weeks.
- Protons: 5 days per week up to 7 weeks.

In addition, weekly check-ups are carried out throughout the treatment to monitor the patient's health. At the end of the treatment, the radiotherapist schedules radiological checks and periodic follow-up visits.

The clinical trial, in which the DP participated, monitored the treatment of head and neck tumours. Typically, each treatment session begins with positioning the patient using the Patient Positioning System (PPS), which consists of a carbon fibre couch that is moved by a robotic arm. The patient is then immobilised using the thermoplastic mask, that was designed during the simulation phase and worn by the subject for the whole duration of the irradiation. A series of optoelectronic markers are integrated into the mask and detected by the Optical Tracking System (OTS) [65], made up of 3 infrared cameras, which ensures the correct positioning of the patient before and during the treatment.

The next step is the acquisition of two X-ray images by the Patient Verification System (PVS, a rotating stereoscopic X-ray imaging system shown in Figure 2.10), which are compared with the images reconstructed from the CT acquired during the simulation phase. The comparison is made by co-registration of the two images, aligning bone structures that are considered fixed, such as the skull perimeter, frontal sinuses and orbital contours. Once the two images have been compared, a displacement is calculated to bring the patient into the position in which the treatment plan is to be carried out; the accuracy achieved by this comparison is ± 0.3 *mm* in translation and ± 0.1° in rotations [66].

Figure 2.10: View of a CNAO treatment room with X-ray patient positioning verification system.

After checking that the patient is correctly positioned, the treatment begins. The particle beam is delivered using the active scanning technique in which the target volume is divided into layers of equal energy (slices) and each slice is divided into smaller elements (voxels). A monochromatic beam irradiates each voxel and is deflected by magnets to deliver the dose to each slice. For each treatment, different directions of the primary beam, called *field*, can be used to irradiate the patient. The transition from one *field* to another is made by the PPS, which extrapolates information from the treatment plan and takes $\sim$ 2 - 3 minutes. The irradiation of a single *field* takes approximately 3 minutes, making the total duration of a treatment session an average of 30 minutes, most of which is spent immobilising and checking the patient's positioning.

The entire INSIDE system is used in the workflow as soon as the patient positioning is complete. The work group (usually consisting of three people per treatment day) moves the cart to the operating position described in Section 2.2.2 and shown in Figure 2.11 during a data-taking. After the positioning of the cart, the couch, guided by the PPS, is returned to the position defined by the treatment plan and beam delivery begins.

Figure 2.11: View of the treatment room n.1 at CNAO where the INSIDE system is integrated: DP is the beige box and the two PET heads are the white boxes above and below the bed.

There is an operator in the treatment control room who is responsible for starting the DP data acquisition before the start of each *field* and stopping it when the beam delivery is complete. Due to space limitations caused by the fixed position of the DP for all treatments, not all the *fields* can be monitored and if a second X-ray session is required, the INSIDE system must be removed and re-positioned after it. The cart is positioned with an accuracy of the order of $\sim 1\ mm$ during different measurement sessions. This positioning uncertainty leads to a systematic error in the reconstruction of the emission point of the secondary fragments in the treatment room reference system, but it is negligible compared to the uncertainty due to the multiple scattering.

2.3.2 Patients overview

Patients with the following diseases were selected for the clinical trial: meningiomas and squamous cell carcinomas of the nasopharynx treated with protons; Adenoid Cystic Carcinoma (ACC), clival chordomas and Intestinal-Type-AdenoCarcinoma (ITAC, a specific malignant tumour of the nasal cavities) treated with carbon ions. This choice was motivated in part by the possibility of monitoring both types of particles available at CNAO (protons and carbon ions) and then by the greater benefit that these pathologies could obtain from the range monitoring offered by the INSIDE system. Indeed, these clinical cases are affected by a pathology in which a morphological change is expected often resulting in the filling or emptying of the cranial cavities due to possible inflammation of the tissues or a change in the affected tumour mass.

A total of 40 patients were selected, some of whom were expected to have a morphological change and some of whom were expected to remain unchanged. The criteria for inclusion in the study are reported below:

- Patients that could be treated at CNAO with horizontal proton or carbon ion beams;
- Patients with pathologies from the list above;

- Compatibility of the INSIDE monitoring system with all beam delivery devices in the irradiation position;
- Possibility of performing emergency procedures with the INSIDE system integrated in the room;
- Patient's signed informed consent.

Of the 40 subjects selected, only the first half were observed in the first phase of the study. Among these, 10 were treated with carbon ions and monitored with the DP. In Table 2.3, the clinical information of the ten patients is presented. In the subsequent study, 60% of the patients treated with carbon ions underwent a re-evaluation CT and of these, only two cases (PZ6 and PZ10) were re-planned, while in the remaining four cases (PZ1, PZ2, PZ4 and PZ8) it was not considered necessary to change the planned treatment plan.

Patient ID	Pathology	Re-evaluation CT	Re-planning
PZ1	ACC	7° fraction	no
PZ2	ACC	5° and 10° fraction	no
PZ3	ACC	no	no
PZ4	ACC	8° fraction	no
PZ5	clival chordoma	no	no
PZ6	ITAC	7°fraction	yes
PZ7	clival chordoma	no	no
PZ8	ACC	7° fraction	no
PZ9	clival chordoma	no	no
PZ10	ITAC	8° fraction	yes

Table 2.3: Clinical information on the 10 patients monitored in CNAO clinical trial.

Table 2.4 summarises the main characteristics of the treatment plans for each patient, such as the number of fractions (treatment days) into which the plan is divided, the angle of each *field* in a given fraction, and the total dose for each subject.

The angle at which each *field* is delivered to the patient was evaluated as the angle between the beam trajectory and the patient couch. The former is fixed, while

Patient ID	N. Fractions	Field0 (B1) - N. ^{12}C	Field1 (B2) - N. ^{12}C	Field2 (B3) - N. ^{12}C	Dose [GyE]
PZ1	16	0° - $2.04 \cdot 10^9$	180° - $1.58 \cdot 10^9$	270° - $9.82 \cdot 10^8$	65.6
PZ2	12	340° - $1.90 \cdot 10^8$	200° - $1.62 \cdot 10^8$ - *no DP*	/	54
PZ3	20	/	270° - $2.49 \cdot 10^8$	155° - $1.57 \cdot 10^8$ - *no DP*	60
PZ4	16	0° - $2.20 \cdot 10^9$	310° - $1.77 \cdot 10^9$	/	68.3
PZ5	16	0° - $5.43 \cdot 10^8$	180° - $4.69 \cdot 10^8$ - *no DP*	290° - $6.58 \cdot 10^8$	70.4
PZ6	16	15° - $7.41 \cdot 10^8$	195° - $7.15 \cdot 10^8$ - *no DP*	270° - $5.98 \cdot 10^8$	65.6
PZ7	16	0° - $9.25 \cdot 10^8$	180° - $9.64 \cdot 10^8$ - *no DP*	270° - $9.58 \cdot 10^8$	70.4
PZ8	16	320° - $1.11 \cdot 10^9$	15° - $1.38 \cdot 10^9$	270° - $8.69 \cdot 10^8$	64
PZ9	16	0° - $8.02 \cdot 10^8$	180° - $1.35 \cdot 10^9$- *no DP*	270° - $1.63 \cdot 10^9$	65.6
PZ10	16	264° - $2.25 \cdot 10^9$	0° - $1.39 \cdot 10^9$	180° - $1.63 \cdot 10^9$	65

Table 2.4: Treatment plan of the 10 patients included in the trial, treated with carbon ions and monitored using the DP.

the latter can rotate in a plane parallel to the ground. At an angle of 0° the beam enters from the left side of the patient shown in Figure 2.12 (left) thus an angle of 270° is related to the positioning of the patient with the body aligned along the beam direction (right). For a patient, the different *fields* of the treatment are also called B1, B2 or B3 in order to distinguish them. *Fields* that cannot be monitored by the DP due to space limitations are outlined in the Table 2.4 with the notation $noDP$.

Figure 2.12: View of the INSIDE cart with the DP and the PET heads installed in treatment room n. 1 at CNAO: (left) View of the first patient treated with ^{12}C ions and monitored with DP. The image also shows the 0° position of the bed. (right) Patient mask attached to the bed to show the position of the DP during a *field* at 270°.

For the treatment of superficial tumours, a range shifter can be used because the beam energy needs to be lower than the limit imposed by the synchrotron. The range shifter consists in a layer of solid water of 3 *cm* thick, placed between the primary beam nozzle and the patient. It is positioned manually on the couch or directly at a fixed distance from the nozzle (32 *cm*). When the range shifter is crossed by the primary beam, many secondary fragments are produced which contribute to the total number of reconstructed tracks. Both fragmentation and energy loss due to the range shifter must be considered when planning and optimising the treatment plan with TPS.

2.4 Emission point reconstruction

The emission profile of the secondary charged fragments along the incident beam axis is reconstructed back-tracking the tracks measured inside the DP. The following section describes the process that leads to the determination of the emission point from the collected data.

When a secondary proton exit the patient and hits the DP fibres, it produces a collection of hits when the signal is above a predefined threshold in the SiPMs. The DP fibres are not optically insulated. The signal produced by one fibre can be collected by an adjacent fibre due to the optical *crosstalk*. In addition to optical *crosstalk*, there is also electronic *crosstalk* occurs when an electronic signal generated by one SiPM induces another one on adjacent SiPMs. At the same time, due to a mismatch between fibre and the SiPM, a given fibre can be readout by two SiPMs on different detector sides. In general, the signature of the crossing of a charged particle through a DP plane is the creation of a signal given by a cluster of fibers on both views.

It is expected that when a proton crosses a DP plane, more than one SiPM will give a signal. These phenomena mean that signals from adjacent fibres must be combined to give the best estimate of where the proton has actually passed. Therefore, hits (pixels with a signal above the threshold) belonging to adjacent positions in space are clustered. The average cluster size due to *crosstalk* phenomena was evaluated with measurements at the Trento Proton Therapy Centre. Figure 2.13 shows the results obtained: an average hit value of ~ 1.5 per cluster is found. The cluster position in the plane, which is used to reconstruct the fragment tracks, is obtained as the arithmetic mean of those belonging to the individual hits. An example of the reconstruction of a track inside the DP is shown in Figure 2.14, where the two views in the respective planes (x,z) and (y,z) are presented. The reconstruction of the trace occurs only when there are at least four clusters aligned in each projection, in order to maximise the efficiency of the track reconstruction, minimising the contribution due to the background.

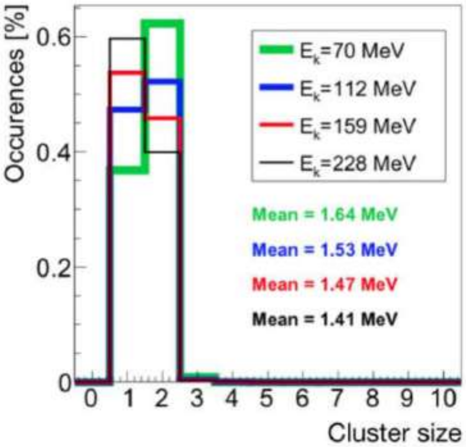

Figure 2.13: Cluster size measured using proton beams of different energies [60].

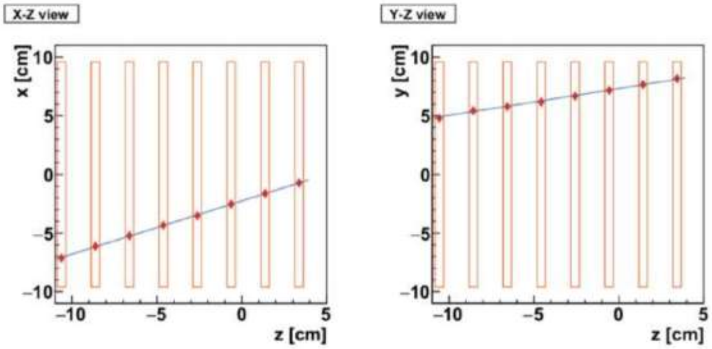

Figure 2.14: Example of track reconstruction (MC): the orange rectangles represent the eight fibre planes, the red markers indicate the position of the clusters and the reconstructed fragment track is superimposed (blue line) [60].

The fragments trajectory is reconstructed by applying the Hough transform, an image processing extraction technique that determine a straight line starting from a series of points [67]. The operating principle of the transform is shown graphically in Figure 2.15: (a) a collection of straight lines intercepting the point of coordinates (x',y') is associated with a straight line in the Hough space (m,b) (b); so, four points aligned in the x-y plane (c) determine an accumulation point in the Hough plane m-b (d), and finally the coordinates of this point (m',b') can be used as best estimate of track parameters.

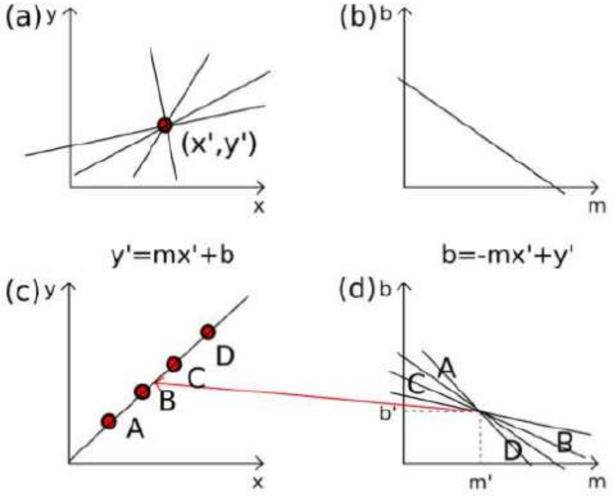

Figure 2.15: Graphic description of the Hough transform [32].

Once the coordinates of the accumulation point have been obtained, a χ^2 test is performed to verify their goodness. The contribution of the multiple scattering (MS) of the charged fragments, within the fibres, is negligible due to the short inter-plane distance and the high measured cluster size (1.5 *mm* on average). The average detection efficiency of the different planes was evaluated using the secondary fragments produced by irradiating an anthropomorphic phantom with carbon ion beam treatment plan and was $\sim$ 90% for each plane. In order to obtain it, the reconstruction of the tracks was carried out without using the information about the hits in the investigated plane.

Once the tracks have been selected, in order to estimate the coordinates (x,y,z) of the fragment emission point, the Point Of Closest Approach (POCA) between the reconstructed track and the carbon ion primary beam direction has been used (as shown in Figure 2.16). It consists in projecting the track towards the primary beam direction, provided by the DDS, taking into account the contribution of the MS.

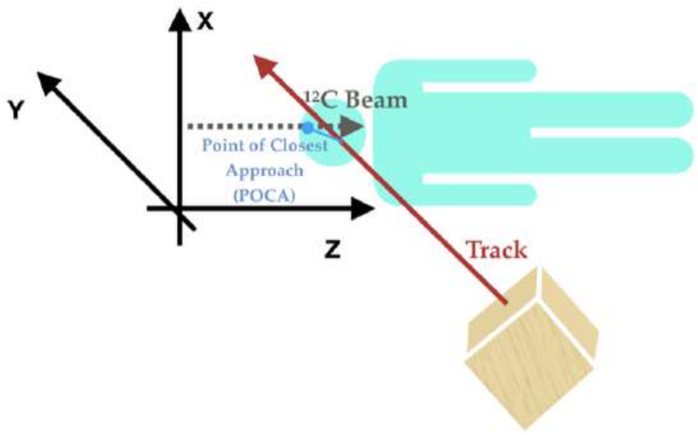

Figure 2.16: Schematic view of the Point Of Closest Approach (blue) reconstruction between the primary beam direction and the reconstructed fragment track [32].

The MS introduces an uncertainty of $5 \div 10\ mm$ in the position of the emission point, depending on the depth of the production point and the MCS that depends on the amount of material crossed by the secondary particles. In order to measure the resolution of the technique along the direction of the primary beam (z-axis), tests were carried out using a small plastic sphere target (d $= 4\ mm$, point-like target) placed at a variable distance from the detector. After irradiating the target with carbon ion beams, the tracks were reconstructed using the DP and the results are shown in Figure 2.17. On the left the distribution of the emission coordinates along z-projection obtained from the backtracking of the fragment is shown: in order to model the background, the curve has been fitted as the sum of a double Gaussian and a polynomial of degree 4^{th}. The resolution of the detector has been obtained as the weighted average of the two Gaussian resolutions; on the right, the total resolution is shown as a function of the target-DP distance. Under operating conditions, with the detector placed at a distance of 50 *cm* from the isocentre of the treatment room, a resolution value of 7 *mm* is obtained. This value is similar to the required one for hadrontherapy applications.

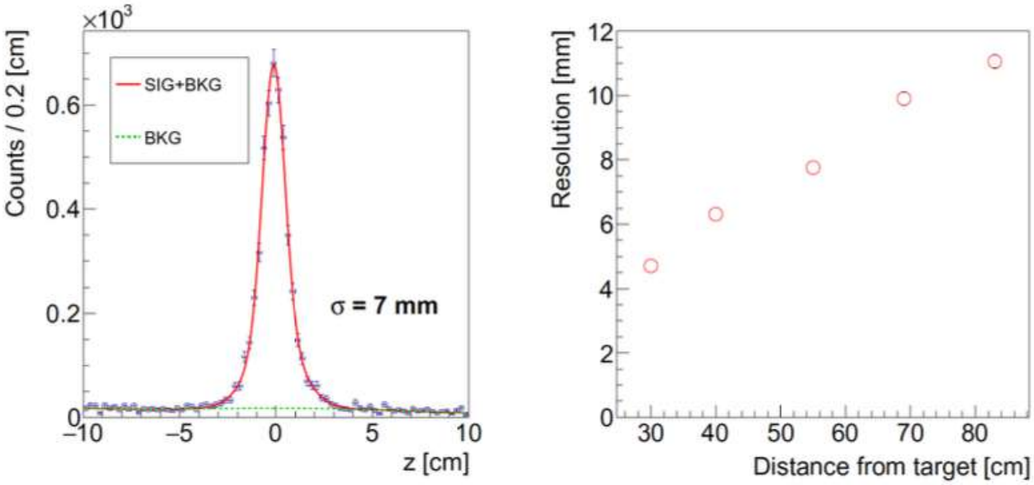

Figure 2.17: Left: distribution of the reconstructed coordinate along the beam direction (z) with the DP placed at 50 *cm* from the plastic sphere target (carbon ion beam at 280 MeV/u). Right: Resolution of the DP as a function of distance from the target [60].

2.5 Gamma Index

The gamma index test is a useful tool for dosimetric verification that is typically used to evaluate the degree of agreement between two 3D dose distribution maps. In this study, however, it is used to compare two secondary charged fragment emission maps from two different fractions, using the first one as a reference. The variation between two emission profiles is indicative of morphological variation inside the patient along the primary beam direction, as described in this chapter previously. The test can be exploited to identify the voxels in the evaluation map that are significantly different from the corresponding voxels in the reference map, i.e. those in which a change in density has occurred.

The gamma function is a Euclidean distance defined in a two-dimensional emission density space:

$$\Gamma(\vec{r_e}, \vec{r_r}) = \sqrt{\frac{|\vec{r_e} - \vec{r_r}|^2}{r^2} + \frac{|D_e(\vec{r_e}) - D_r(\vec{r_r})|^2}{D^2}} \tag{2.2}$$

where:

- $\vec{r_e}$ identifies the voxel, belonging to the evaluation map, on which the test is being performed;
- $\vec{r_r}$ identifies the voxel belonging to the reference map;
- $D_e(\vec{r_e})$ and $D_r(\vec{r_r})$ are the emission densities evaluated at points $\vec{r_e}$ and $\vec{r_r}$ respectively;
- r and D are two parameters used to describe the spatial tolerance and the emitted density, respectively.

Given an i-th voxel $\vec{r_e}$ of the evaluation map, this function is calculated for all voxels $\vec{r_r}$ of the reference map. The γ value for the i-th voxel is defined by the minimum of all the values returned by the Γ function:

$$\gamma(\vec{r_e}, \vec{r_r}) = min\{\Gamma(\vec{r_e}, \vec{r_r})\} \quad \forall \vec{r_r} \tag{2.3}$$

If the γ is greater than 1, means that the i-th voxel has varied significantly from the reference map. Figure 2.5 shows a schematic representation of the gamma index method in a two-dimensional distance-emission density space. The blue line is the result of calculating the gamma function for all voxels of the reference map, given a certain voxel of the evaluation map, represented by the blue x at the origin of the axis. The test is successful if the gamma index is less than one. Otherwise, the test result is negative.

The gamma index test is highly dependent on the tolerance parameters r and D. The parameter r indicates the radius of the sphere delimiting the voxels of the

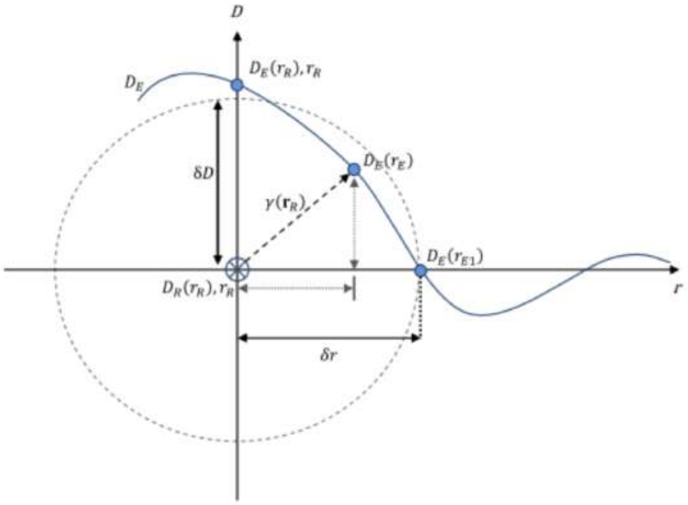

Figure 2.18: Schematic representation of the gamma index test. The x-axis is the distance between the tested voxel and voxels on the reference map, the y-axis is the emission density. The cross at the origin of the axes represents the tested voxel on the evaluation map, while the blue line is the result of the calculation of the function Γ for all voxels on the reference map. If the curved line (in blue) passes inside the ellipse defined by the tolerance parameters, the test result is positive, otherwise it is negative [68].

reference map taken into account for comparison with the i-th tested voxel (placed at the centre of the sphere). Increasing r means enlarging the observation region around the tested voxel and thus calculating the function $\Gamma(\vec{r_e}, \vec{r_r})$ on a larger number of voxels of the reference map, increasing the chances of finding at least one voxel $\vec{r_r}$ such that $\gamma(\vec{r_e}) \leq 1$. Therefore, if even a single voxel, among all those contained inside the sphere of radius r, verifies the condition $\Gamma(\vec{r_e}, \vec{r_r}) \leq 1$, then the gamma index of the voxel of the evaluation map will be less than 1 and the test result will be positive. In conclusion, the larger the tolerance parameter r, the easier it is that the content of the voxel has not changed compared to the corresponding one in the reference map.

Given a sphere of radius r around the tested voxel and assume that for a certain value $D = D^*$ such that $\gamma(\vec{r_e}) > 1$, This means that for all the emission density distances $|D_e(\vec{r_e}) - D_r(\vec{r_r})|$, evaluated at each voxel $\vec{r_r}$ inside the sphere, $\Gamma(\vec{r_e}, \vec{r_r}) > 1$

is valid, and thus the test result is negative. The effect of increasing D is to consider more and more voxels of the reference map increasing the possibility to find a voxel for which $\Gamma(\vec{r_e}, \vec{r_r}) \leq 1$, resulting in a positive value of the gamma test. In this study the parameters used as input for the gamma index code include two quantities closely related to the tolerance values shown above, as well as a threshold expressed as a percentage:

- DTA: Distance to Agreement $[mm]$;
- DD $= \frac{D}{D_{r_{max}}(\vec{r}_{r_{max}})}$: Emission Density Distance [%];
- DTH: Threshold related to emission density[%].

While the parameter r corresponds exactly to the DTA, the parameter D is expressed as a percentage of the maximum emission density value $D_{r_{max}}(\vec{r}_{r_{max}})$ of the reference map. In this way, the emission density tolerance D is redefined as the Emission Density Distance (DD). The test output also depends on a threshold in % (DTH), which allows to exclude all the voxels $\vec{r_e}$ of the evaluation map with an emission density value less than a certain percentage e of the maximum value of the reference map. The DTH value chosen for the gamma index test in the data analysis of this thesis is 5% as already optimised in previous studies [69, 70]. Gamma index maps can be measured following two different approaches:

- Gamma mode
- Pass rate mode

In the first case, the value of the gamma index for each voxel is distributed between 0 and a maximum value, depending on the two tolerance values chosen. In order to ease the readability of the gamma index map, the pass rate mode has been developed considering the value of the voxel as binary: 1 if the gamma value is bigger than 1, 0 if the gamma value is between 0 and 1 (Figure 2.19). In this mode clusters of discrepant voxels are easier to read.

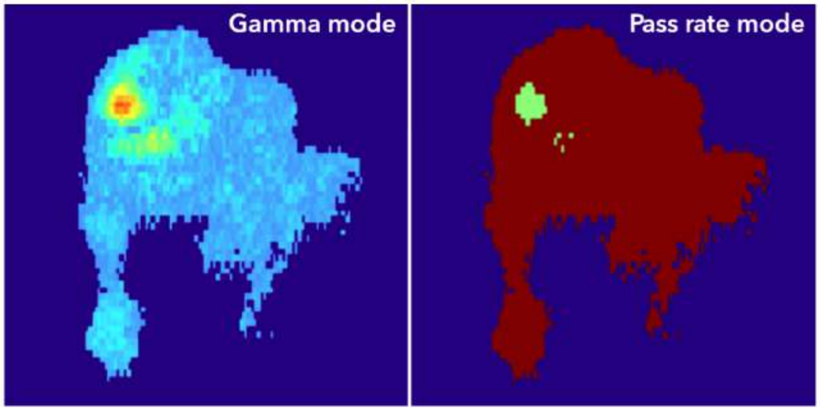

Figure 2.19: (Left) 3D gamma index map in gamma mode. (Right) 3D gamma index map in pass rate mode.

2.6 Monte Carlo simulation

In order to evaluate the performance of the DP and to verify the results obtained from the data collected during the clinical trial, Monte Carlo simulations (MC) were performed using the FLUktuierende KAskade (FLUKA) code [71, 72]. The MC method is used in a variety of scientific fields, including medical physics, where it is applied to the planning of radiotherapy treatments, imaging and the design of particle detectors to simulate particle-matter interactions. The various steps involved in developing a simulation start with modelling the geometry of the problem and the materials involved, including the type of particles in the beam, their energy and transport from the point of origin to their interaction.

With the FLUKA software is possible to simulate with high precision the interaction with matter and the propagation of about 60 types of particles, including photons and electrons in the energy range from 1 keV to thousands of TeV and hadrons with energies up to 20 TeV. The editing, execution and visualisation of output files can be done through the Flair (FLUKA Advanced Interface) graphical interface [73].

In this thesis, the setup of the clinical trial at the CNAO facility in terms of treatment room and DP, has been developed within the FLUKA software. Every individual pencil beam that make up the primary treatment beam is implemented thanks to the information on the energy and position provided by the DDS. The patient is simulated importing the densities of each voxel from the patient's CT. Furthermore, a specific function of FLUKA automatically performs the conversion between Hounsfield Units (HU) and the different densities of the patient's tissues, by applying calibration coefficients. The output of the FLUKA software is then processed including the information obtained from the pre-clinical characterisation measurements of the detector (Section 2.4) in terms of energy resolution, fibre detection efficiency and optical *crosstalk* contribution.

A schematic representation of the simulated setup provided by the FLUKA graphical interface is shown in Figure 2.20, where the DP is visible in its operating position. The Figure also shows the range shifter (green rectangle) for modulating the beam energy, the ionisation chambers and the nozzle from where the primary beam of carbon ions comes out (purple rectangles). Finally, the patient's CT positioned on the couch (grey rectangle) of the PPS is visible.

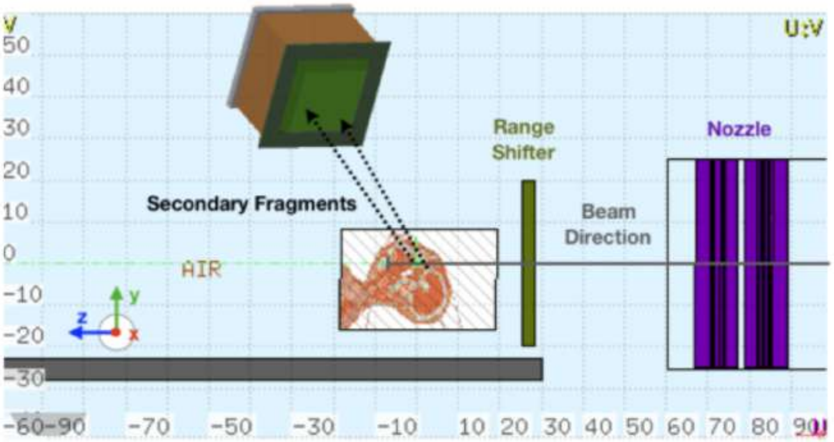

Figure 2.20: View in the y-z plane of the clinical setup of the CNAO implemented at FLUKA, showing the CT of the patient, the DP (green and brown cube), the RS (in green) and the nozzle (in violet and black) from which the primary ion beam comes out.

For the simulations, two CT of each examined patient were provided as input to the software, one (CT1, plan) acquired before the start of therapy to establish the treatment plan to be administered and the other (CT2, replan) after a certain number of treatment fractions. Indeed, by applying the same treatment to both CTs for each patient and comparing the distributions of the secondaries detected by the DP, the sensitivity to the morphological change demonstrated by the patients' CT2 can be verified. The pre-simulation step involves the co-registration of the two CTs (CT1 and CT2) for each patient in order to align them and was performed using the Slicer 3D software [74], which allows a rigid roto-translation with 6 degrees of freedom to be applied, using the cranial bone structures as a reference.

Once the simulations with FLUKA were complete, a code written in C++ was used to construct the 3D emission maps of the loaded fragments. It takes the FLUKA simulation as input, reprocesses it to reconstruct the quantities measured by the DP (Section 2.4) and using the same methods for data and simulation evaluates the emission profile.

To account for this uncertainty, the content of the single voxel in terms of emission density is distributed over a sphere of radius R centred on the voxel itself. The final 3D map will then be the result of the superposition of the contents of all the spheres constructed around all the voxels in the map. The value of R used in the following data analysis to construct all the maps is 5 mm. Once the two emission maps of the charged fragments have been reconstructed for a given patient, they are compared using the gamma index test described in Section 2.5.

In this clinical trial, the emission map of the first fraction will be compared with subsequent fractions to evaluate the inter-fractional monitoring method. Once the pre-treatment CT is performed, it can take one to two weeks before the patient is irradiated, which is enough time for significant changes to occur in the tissue. In this case, a comparison of the emission maps would show no difference, while the two CTs (CT1 and CT2) would be different. In the case of MC simulations, the two CTs of the patient are used as input for the treatment, so that the morphological conformation of the patient at the time of irradiation and DP data acquisition is known with certainty. For this reason, MC simulations were performed to verify that the results of the data were consistent with those of the simulations.

Chapter 3

Inter-fractional monitoring: Dose Profiler performance evaluation

The DP, as described in Chapter 2, provides an alternative strategy that allows inter-fractional monitoring to detect any morphological changes. The secondary fragment emission maps generated from the DP reconstructed traces are indeed strongly correlated with the tissue density distribution. The comparison of maps from different treatment fractions allows the identification of density changes in the patient's tissues.

An initial approach to identifying variations was based on the comparison of emission maps projected along the axis of beam propagation (z-axis) [75]. However, the results of this one-dimensional analysis showed a low sensitivity to variations occurring deeper down and an inability to provide information about the spatial localisation of the morphological change. In order to overcome these limitations, we moved to a three-dimensional approach involving the comparison of 3D emission density maps. The mathematical tool used to compare the 3D maps of the different fractions voxel by voxel is the gamma index test, the output of which depends on a number of free parameters that are explained in Section 2.5.

The aim of this work is to optimise the gamma index test free parameters in order to be able to adopt the DP inter-fractional range monitoring technique in a real clinical workflow scenario. In addition, I evaluated the performances of this method in detecting morphological changes, measuring the limitations and weaknesses. The analysis has been conducted both with data collected at the CNAO facility during the clinical trial of the INSIDE project and by means of MC simulations.

3.1 Data selection

In this thesis, not all the 10 patients described in Section 2.3.2 were analysed, but only Patient 1 (PZ1), Patient 4 (PZ4), and Patient 6 (PZ6) has been selected. This choice is dictated by the necessity to study only the patients with a re-evaluation CT. The second CT is essential to verify the morphological changes detected by the DP and to study the detector inefficiencies, evaluating the overall DP sensibility. A re-evaluation CT was also acquired for Patient 2, Patient 8 and Patient 10 but they were not included in this thesis due to data collection problems.

MC simulations were only performed on two patients: PZ4 and PZ6, as they were considered the most interesting to analyse in terms of the efficiency and sensitivity of the DP. In MC simulations, all DP characteristics are simulated and the methods of analysing the reconstructed quantities (e.g. emission map, etc.) are the same for both MC and data, as described in Section 2.6. However, differences between MC and data can arise due to the timing of the initial CT. Indeed, the pre-treatment CT is usually performed one week before the first treatment fraction, so any morphological changes between the initial CT and the first irradiation session cannot be detected by the DP. Instead, in MC simulations, the pre-treatment CT is used as input to the simulation. In particular, for PZ6 the CT was performed two weeks before the first treatment fraction due to personal problems of the patient.

The hadron-nucleus inelastic interaction cross sections adopted in the FLUKA MC simulation tool are based on nuclear interaction models that are constantly updated with the new experimental cross section data, which are exploited as benchmark. Since there was a lack of cross section data for the light fragments production in the carbon ion therapy particle and energy range, data on the flux of secondary charged particles emitted were collected using the DP prior to the start of the IN-

SIDE clinical trial in order to calculate the primary beam-target cross sections and to optimize the DP positioning in the treatment room [76]. The fragment yields obtained from the data were consistent with those used in the simulations, although several differences were found.

This chapter describes the three patients in detail, showing for each the morphological changes that occurred during treatment and that the DP should have detected. The pre-treatment planning CT (CT1) and the re-evaluation CT (CT2) are shown for each patient and morphological changes are highlighted with a yellow circle. For information on the treatment plan, see Table 2.4 in Section 2.3.2.

Patient 1

For PZ1, only the 0° *field* (B1) was analysed. Indeed, this *field* is characterised by a topology favourable to the detection of secondaries emitted by the patient. Furthermore, whereas the range shifter is manually positioned for the other configurations, for *field* B1 it is rigidly attached to the beam nozzle, thus avoiding any uncertainty regarding the repeatability of its positioning. Figure 3.1 shows the two CTs (CT1 and CT2). The filling of the cavity is highlighted by the yellow circle. It is probably due to an inflammatory state of the tissues surrounding the tumour mass in response to the irradiation. In PZ1, the morphological changes shown on the re-evaluation CT were not significant enough for the physicians to change the treatment plan.

Patient 4

In the case of patient 4, six fractions were monitored, for both *fields* B1 and B2. However, only the analysis for the B1 *field* is reported in this thesis, as it is the *field* with the most favourable topology for the detection of secondary fragments. Figure 3.2 shows the comparison between the two CTs, where the re-evaluation CT was acquired the day before the last fraction monitored with the DP. The yellow circle shows the emptying of the frontal sinuses, which is responsible for a significant decrease in HU in the transition from CT1 to CT2.

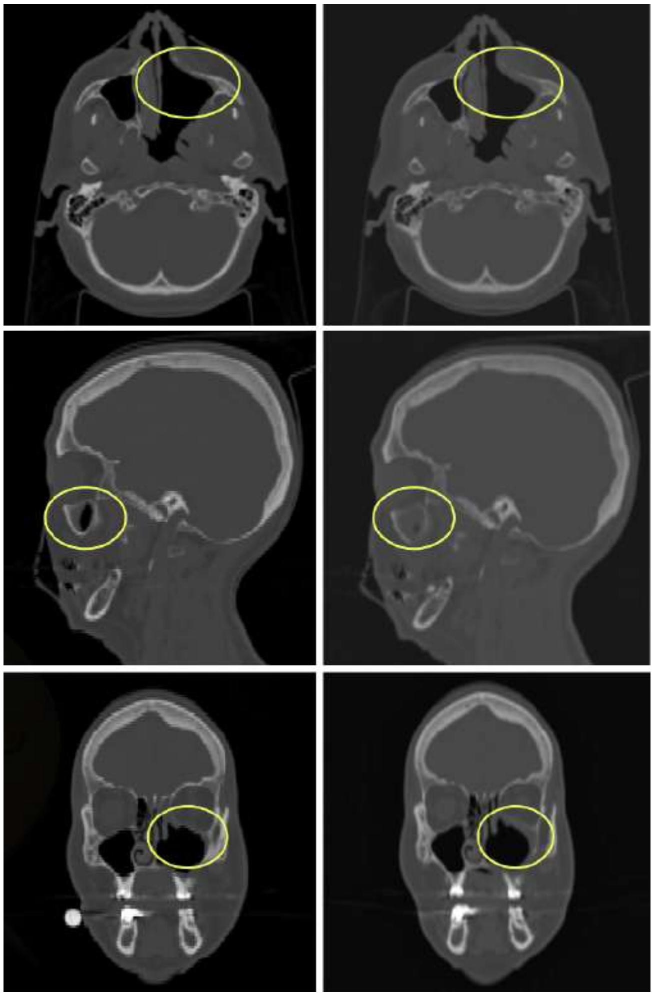

Figure 3.1: Comparison of CT1 (left) and CT2 (right) for PZ1: for both CTs, the transverse (top), sagittal (middle) and coronal (bottom) sections are shown. The cavity filling is shown in the yellow circles.

Patient 6

For PZ6, the planning CT was acquired approximately 20 days prior to the administration of the first fraction, and the re-evaluation CT was acquired after the seventh treatment fraction. The comparison of the two CTs shows two different morphological changes. The first one is very large and it is located in the tumour region, leading to a large variation in density, as highlighted by yellow circles in the

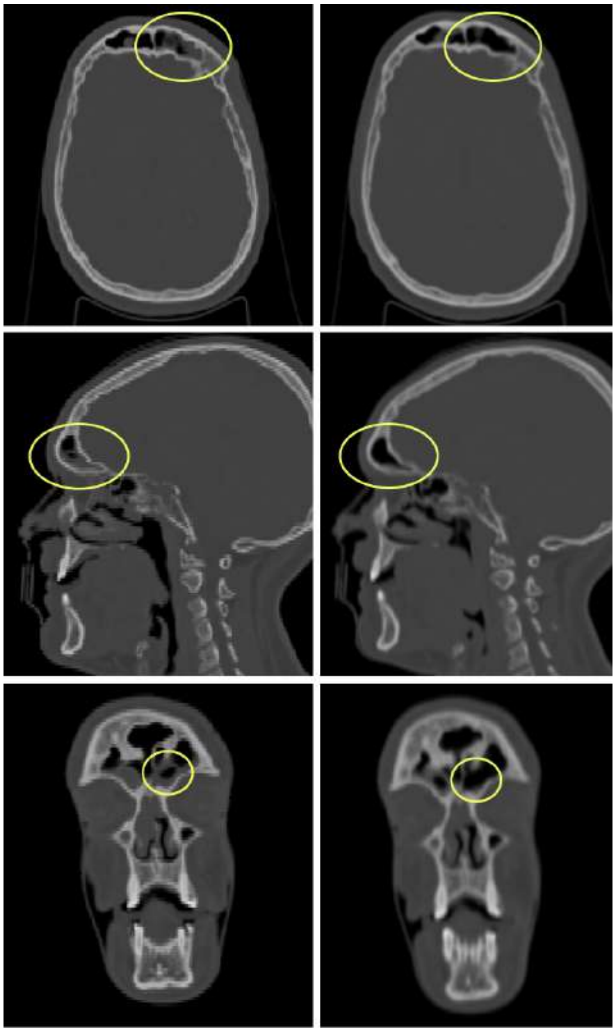

Figure 3.2: Comparison of CT1 (left) and CT2 (right) for PZ4: for both CTs, the transverse (top), sagittal (middle) and coronal (bottom) sections are shown. The emptying of the frontal sinuses is shown in the yellow circles.

left panel of the Figure 3.3. Probably, the change is due to the enlargement of the tumour. On the other hand, the second one is small and it's shown in the yellow circles in right panel of the Figure 3.3. PZ6 is the only one that has been rescheduled. For PZ6, only the B3 *field* (270°) was analysed as it is favourable for the detection of charged secondary fragments.

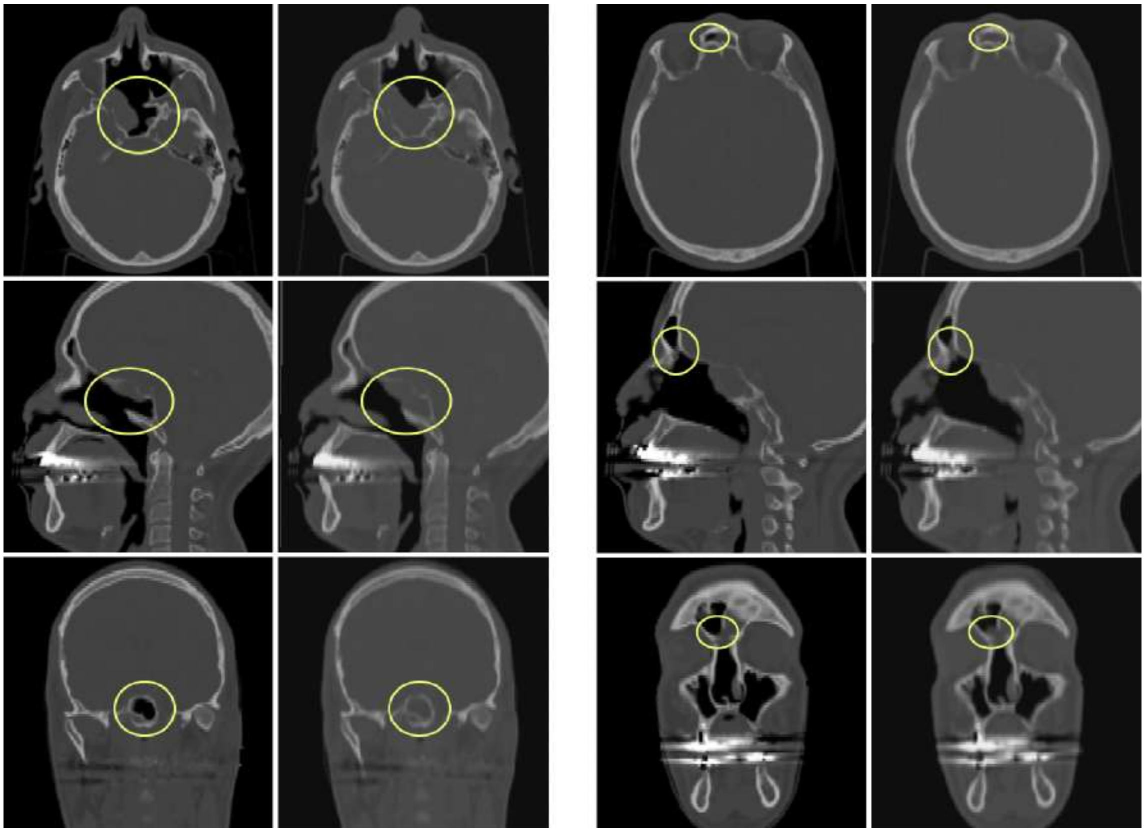

Figure 3.3: Comparison of CT1 (left) and CT2 (right) for PZ6: for both CTs, the transverse (top), sagittal (middle) and coronal (bottom) sections are shown. In the left panel is shown the first large morphological change, while the second one is shown in the right panel.

3.2 Gamma index 3D optimization strategy

Optimising the free parameters of the gamma index is one of the objectives of this work. In a carbon ions hadrontherapy treatment, the emission of secondary charged fragments is closely related to the morphological structure and thus to the CT of the patient; in particular, the greater the tissue density, the greater the number of nuclear interactions between the projectile and the target and, consequently, the greater the number of secondary fragments escaping from the patient.

If there is a morphological difference between the pre-treatment CT (CT1) and the re-evaluation CT (CT2), it can be observed producing a Hunsfield Units difference map (ΔHU). Exploiting the DP detector, a morphological change can be pointed out by means of the gamma index test conducted on the reconstructed secondary fragments emission maps. For this reason, the map of ΔHU between the two CTs is closely related to the gamma index map (the output of the gamma index test performed between two emission maps).

3.2.1 Optimisation criteria

As mentioned in Section 2.5, the gamma index test depends on three tolerance parameters (DTA, DD, DTH). The threshold parameter DTH has already been optimised and its value used in this work is 5% [69, 70]. The first approach used to optimise the DTA and DD parameters was to study the ability of the gamma index test to recognise the voxels included in the variation region as dissimilar to the reference condition. This was done by evaluating the absolute difference in HU between the two CTs voxel by voxel. Then the ΔHU value was compared with the gamma value obtained from the gamma index test of the corresponding voxel. Two different metrics have been developed: efficiency and purity. The efficiency (η) is defined as:

$$\eta = \frac{number\ of\ voxels\ with\ \gamma > 1\ and\ \Delta HU > threshold}{number\ of\ voxels\ with\ \Delta HU > threshold} \tag{3.1}$$

where the numerator is the number of voxels that have a γ value >1 in the gamma index map and a ΔHU value between the two CTs $>$ of a certain threshold. The denominator consists of all voxels that have ΔHU greater than the same threshold. With this definition, the efficiency is a number between 0 and 1. Efficiency measures how many of the discrepant voxels can be detected. The threshold was introduced to get rid of the negligible differences between the two CTs that can lead to small ΔHU values. It was found that a good threshold for identifying morphological variation is between 500 and 600 HU [70].

The other metric used is purity (ϵ), defined as:

$$\epsilon = \frac{number\ of\ voxels\ with\ \gamma > 1\ and\ \Delta HU > threshold}{number\ of\ voxels\ with\ \gamma > 1} \tag{3.2}$$

where the numerator is equal to the efficiency, while the denominator consists of all voxels with $\gamma > 1$. Purity indicates the precision of the gamma index test, measuring how many of the voxels that the gamma index test detects as discrepant are actually discrepant.

Previous studies have shown that by maximising efficiency, the corresponding gamma index maps are affected by a large amount of noise [69]. For this reason, the preferred parameter to optimise is purity. However, the efficiency is taken into account as secondary parameter in order to evaluate the DP performances. A visual example of two gamma index maps in pass rate mode of PZ4 with different DD and DTA values is shown in Figure 3.4. The green voxels did not pass the gamma index test, i.e. they were detected as discrepant, whereas the red voxels passed the gamma index test. It should be noted that both red and green voxels are those that satisfy the threshold condition set by the DTH parameter, that has been set at 5%. The map on the left maximises efficiency and there is a non negligible salt and pepper effect that lead to difficulties in the detection of the morphological change. On the other hand, the map on the right maximises purity and the single cluster of green voxels is clearly visible and identifiable.

The procedure adopted to optimize the gamma index parameters is to evaluate the gamma index maps for all the patients with all the combinations of the DTA and DD values tabulated in Table 3.1. Then, the efficiency and purity are calculated for each map. The aim is to determine a combination of DTA and DD that can

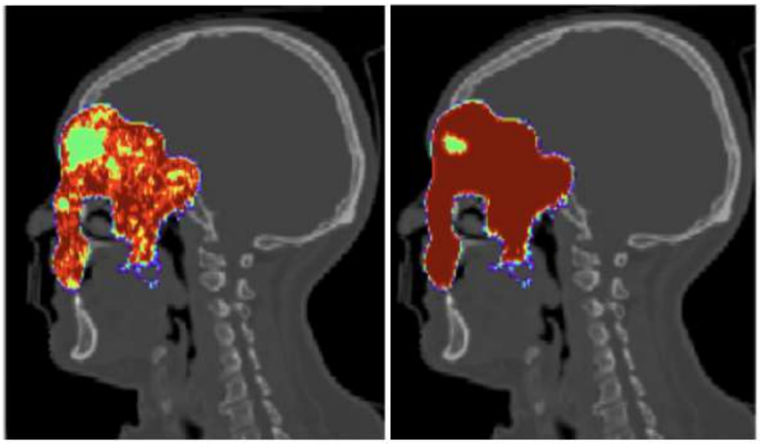

Figure 3.4: Gamma index maps in pass rate mode of PZ4 with different DD and DTA parameters. Left: combination of DD and DTA maximising efficiency. Right: combination of DD and DTA maximising purity [69].

nearly maximize the value of purity for all the patients. In case of DTA and DD combinations that lead to the same value of purity, the values that provides the gamma index maps with the best signal to background ratio has been chosen.

DTA (cm)	10	15	20	25	30	35	40	45
DD (%)	2	4	6	8	10	12		

Table 3.1: Values of DTA and DD used in the analysis of each patient.

3.2.2 Results of the 3D optimisation of the gamma index test parameters

Patient 1

As shown in the Figure 3.5 the purity distribution shows a maximum at ~ 0.056 for DTA = 10 cm and DD = 4%. In particular, fixing a value of DD, the purity is anti-correlated with the respect to the DTA values. On the other hand, fixing the value of DTA the purity shows a maximum for DD = 4%. The efficiency has a maximum of ~ 0.18 for DTA = 10 cm and DD = 2%. By fixing the value of DD, the

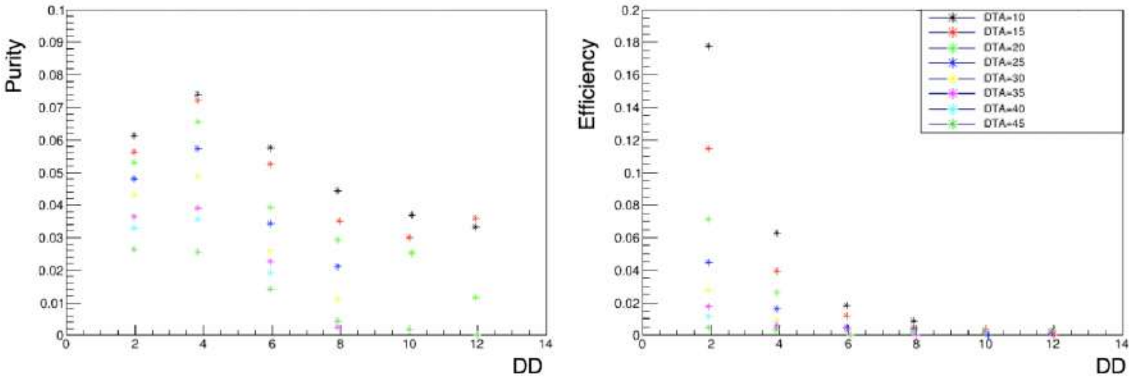

Figure 3.5: PZ1 purity and efficiency as a function of DD value for different DTA values set at a threshold of 500 HU. The legend refers to both plots.

efficiency is inversely proportional to the value of DTA, as is the case for the purity. Fixing the value of DTA, on the other hand, results in an almost hyperbolic trend.

The purity and efficiency values are low for all DTA and DD values. This can be explained by the co-registration effects shown in Figure 3.6, which shows the HU difference map between the two CTs superimposed on the gamma index map in pass rate mode with the parameters that maximise the purity (DTA = 10 cm DD = 4%). It can be seen that the gamma index test succeeds in detecting as discrepant the voxels enclosed in the variation region shown in the yellow circle. However, areas with co-registration effects (orange circle) are also visible. These effects are due to highly mobile organs or tissues that cannot be held fixed between two CTs acquired at different times or two distinct treatment fractions. As an example, highly mobile bone structures such as the maxilla are very difficult to fixate between CTs. In the case of PZ1, the primary beam passes through the maxillary zone and therefore voxels belonging to this area are included in the gamma index test, significantly lowering the purity and efficiency values.

Patient 4

In PZ4 the purity shows a maximum for values of DTA = 10 cm and DD = 8%, although it is almost stable for DD=10% and DD=12%. By fixing the value of DD and increasing the value of DTA, the trend is decreasing, as obtained for PZ1. The

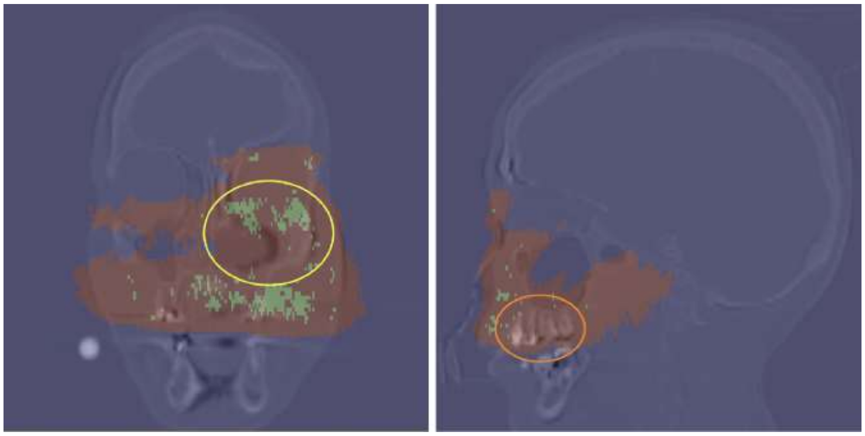

Figure 3.6: PZ1 ΔHU map superimposed on gamma index map (DTA = 10 *cm*, DD = 4%) in pass rate mode. Voxels with $\gamma > 1$ are shown in green and voxels that passed the test are shown in red. The varied morphological region is indicated in the yellow circle. Co-registration effects are shown in the orange circle

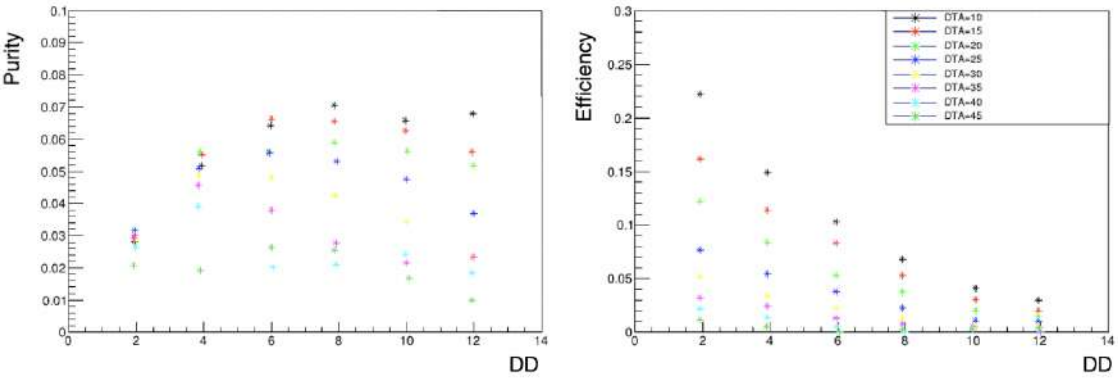

Figure 3.7: PZ4 purity and efficiency as a function of DD value for different DTA values set at a threshold of 500 HU. The legend refers to both plots.

trend of the efficiency is similar to that obtained for PZ1: it is inversely proportional to both the values of DD and of DTA, resulting in a hyperbolic trend. The maximum purity value obtained for DTA = 10 *cm* and DD = 8% is 0.07, while the efficiency value obtained for these parameters is 7%.

Also in this case, both purity and efficiency maximum values are low, but this is due to different reasons with respect to the previous case. Figure 3.8 shows the

ΔHU map superimposed on the gamma index map in pass rate mode with DTA = 10 *cm* and DD = 8%. The gamma index test detects the voxels included in the varied region (highlighted by the yellow circle) as discrepant. It can be seen that this variation has the shape of a spherical shell, while the cluster of green voxels does not cover all the varied region.

In addition, there is another effect that reduces the purity; as can be seen on the left panel of figure, there is a second cluster of green voxels highlighted by the orange circle that does not correspond to any voxels with $\Delta HU > threshold$. This cluster of voxels is placed along the beam direction beyond the morphological change. This effect is due to the fact that the carbon ions, in the re-evaluation CT, reach the area of the second cluster with a different energy with the respect to the pre-treatment CT due to the morphological change. In particular, the emptying of the sinuses lead to a decrease of the density of the material crossed by the projectiles, resulting in a increment of the projectile range and energy. This lead to a higher probability of escaping from the patient and being detected. This is why the emission maps are different in this area.

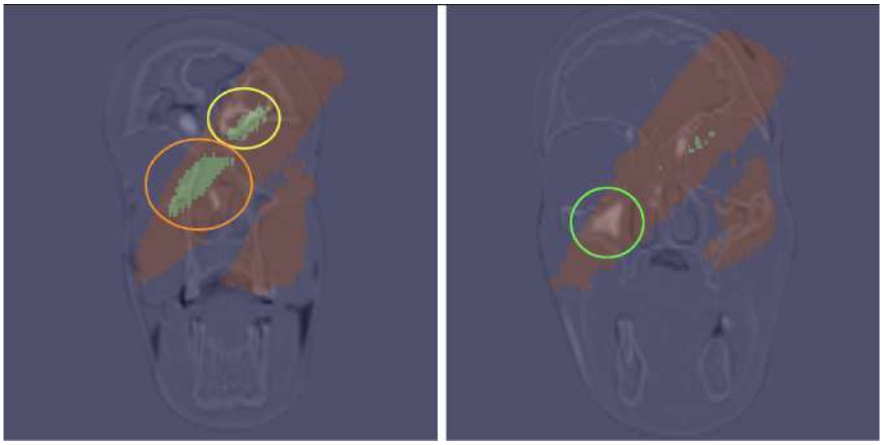

Figure 3.8: PZ4 ΔHU map superimposed on gamma index map (DTA = 10 *cm*, DD = 8%) in pass rate mode. The region varied and detected as discrepant is indicated in the yellow circle. The orange circle indicates the cluster of voxels detected as discrepant but where no change occurred. The variant region that the DP was unable to detect is highlighted by the green circle.

Also in PZ4 there are co-registration effects that reduce the purity and the efficiency. Another reason for reduced efficiency is a cluster of voxels with high ΔHU (green circle) that the DP could not detect as discrepant. The reason for this is probably that this variation is very deep, and only a few pencil beams reach that area resulting in a very low emission density of secondary fragments. This is certainly one of the limitations of the DP. The MC simulation of PZ4 gives results consistent with those derived from the data, showing very similar gamma index maps. Furthermore, the considerations and problems just described were also found in the simulations.

Patient 6

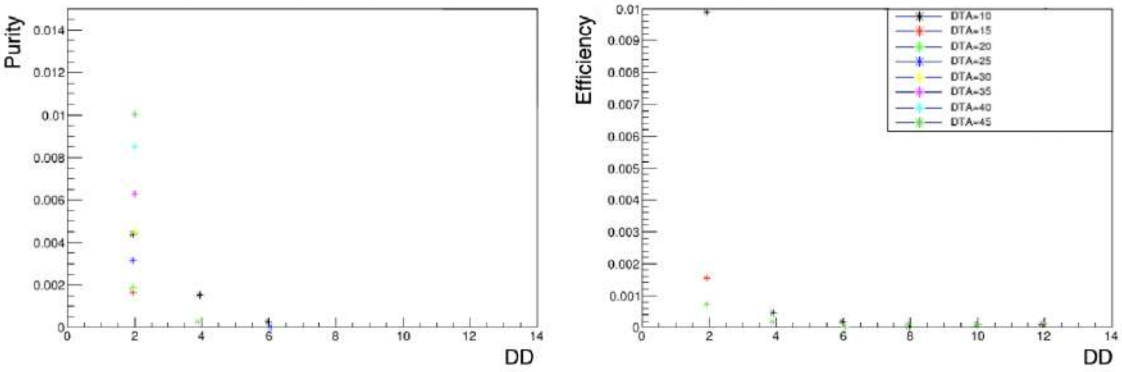

Figure 3.9: PZ6 purity and efficiency as a function of DD value for different DTA values set at a threshold of 500 HU. The legend refers to both plots.

In the case of PZ6, the purity and efficiency values are much lower than for the previous two patients. The purity shows a maximum at DTA = 45 *cm* and DD = 2%, while the efficiency follows the usual hyperbolic trend also obtained with PZ1 and PZ4. The reason for such low efficiency and purity levels is shown in the left panel of Figure 3.10. The gamma index test fails to detect as discrepant the voxels within the first varied region described in Section 3.1.

The MC simulation of PZ6 gives results consistent with those derived from the data. Very low efficiency and purity values are also obtained in the simulation. In particular, the highest purity value is ~ 0.01, obtained with values of DTA = 40 *cm* and DD = 4%. The gamma index maps are very similar to those obtained from the data and even in the simulations the DP does not detect the first morphological variation.

The reason for this inefficiency is due to the fact that the first morphological variation is too deep to be detected by the DP, similar to the case of PZ4. Indeed, the emission density of charged secondaries is very low in this region, as shown in Figure 3.10 (right). Secondaries fragments emitted in the inner regions have to cross a very large thickness of tissues before they can leave the patient and be detected by the DP. The detection statistics for the secondary particles of interest is drastically reduced.

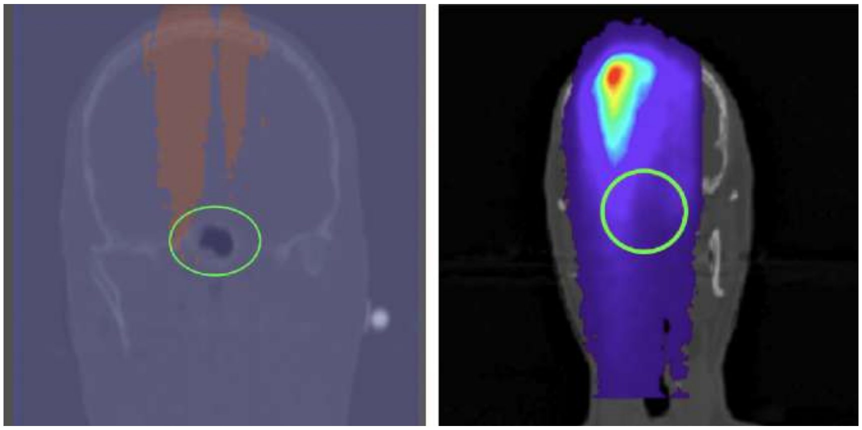

Figure 3.10: (left) PZ6 ΔHU map superimposed on gamma index map (DTA = 40 *cm*, DD = 4%) in pass rate mode. Within the green circle, the morphological variation that the DP should have detected is shown. (right) Emission map of secondary charged fragments reconstructed with DP. It can be seen that the number of fragments reconstructed at depth is much lower than at the surface [69].

However, in the PZ6 gamma index map there is a small cluster of green voxels corresponding to the second small morphological variation in the patient (circle yellow in Figure 3.11). In this case, the DP is able to detect voxels belonging to a varied region as discrepant. Nevertheless, the cluster of green voxels is not exactly superimposed on the morphological change, but it is positioned beyond it, along the direction of the primary beam. This effect, which is present also in PZ4, significantly reduces the efficiency and purity values. Subsequent analyses of PZ6 will be based on the second morphological variation rather than the first one, as the DP was unable to detect it.

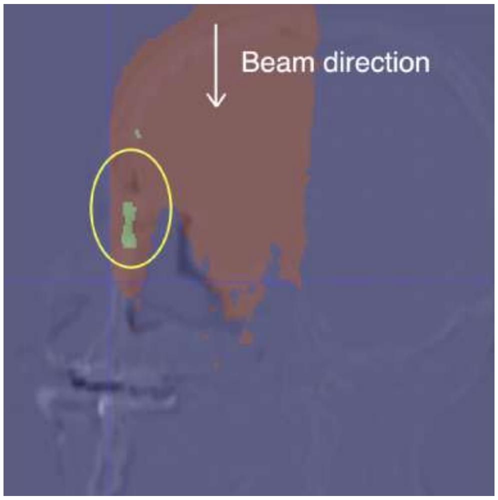

Figure 3.11: An other slice of PZ6 ΔHU map superimposed on gamma index map (DTA = 40 cm, DD = 4%) in pass rate mode. Within the yellow circle, the second morphological variation is shown.

Discussion of end results

The optimization of the gamma index parameters conducted on the 3D secondary fragments emission map shows different optimal DD and DTA parameters for all the patients. In addition, in PZ6 the DP is not able to detect one of the two morphological variations, revealing one of the limitations of the detector: morphological changes in depth are much more difficult to be identified because of the low emission density and the greater difficulty of the charged fragments to escape from the patient.

In addition, two undesirable effects are observed. The first is the co-registration effects that are inevitable. The second is the one presented in the PZ4 and PZ6 results and consists of a cluster of voxels detected as discrepant beyond a morphological change along the beam direction. This effect occurs because the projectiles reach this area with different energies, due to the morphological variation. Consequently, the charged fragments produced have a different energy and therefore escape from the patient with a different probability.

3.3 Gamma index 2D optimization strategy

To overcome the effects encountered in the 3D optimisation described in Section 3.2.2, a new strategy is adopted. It consists of projecting the ΔHU map (absolute difference) and gamma index maps in gamma mode along a plane perpendicular to the beam direction, obtaining 2D maps.

To construct the plane perpendicular to the primary beam direction, the information on the angle of incidence of the interested *field* described in Table 2.4 is used. Figure 3.12 shows, for each analysed patient, the direction of the primary beam and the plane onto which the ΔHU and gamma index maps are projected. Projection are performed as follows: the centre of each voxel of the 3D map is taken and projected onto the plane. The value of the pixel of the 2D map are calculated as the average of all the values of the voxels projected within that pixel.

This method can greatly limit the two undesirable effects found previously. Indeed, the effect of detecting a second cluster of discrepant voxels after a morphological change along the beam direction is absorbed: the two clusters of voxels are projected within the same pixels, resulting in a single cluster in the 2D map. In addition, the effects of co-registration, which are scattered and isolated events, are partially limited by the averaging process to obtain the pixel value in the 2D map.

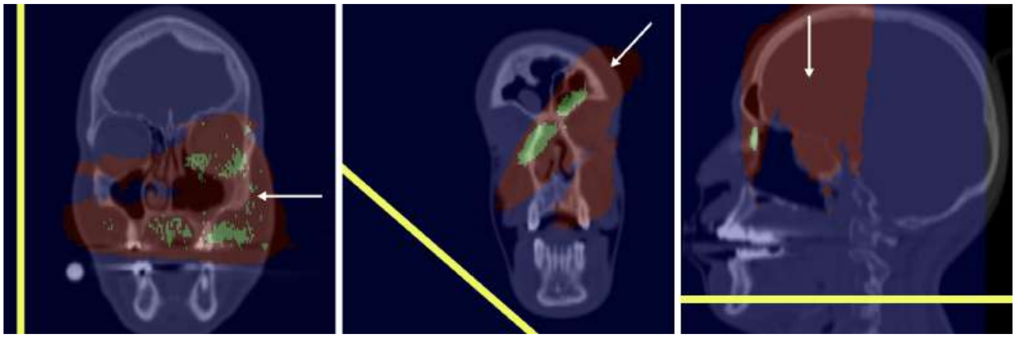

Figure 3.12: CT1 of PZ1 (left), PZ4 (centre) and PZ6 (right), each superimposed on a gamma index map in pass rate mode. The direction of the incoming primary beam is indicated by a white arrow; a yellow line indicates the plane in which the ΔHU maps and all gamma index maps are projected.

In the case of ΔHU map projection it was decided to weight each voxel with the patient's dose map prior to projection. This was done in order to give more weight to the regions that received a higher dose, which are often the most interesting since they are the tumour or nearby areas. In addition, not all voxels of the ΔHU map were projected, but only those for which the gamma index test was performed, i.e. those for which they met the emission threshold dictated by the DTH parameter (red and green voxels in the pass rate mode maps).

Regarding the gamma index map, in the three-dimensional case, the γ threshold is set at 1. In the case of 2D maps, the value of γ takes on different values and a different meaning than in the case of 3D maps, since it is derived from the averaging process. For this reason, the definitions of purity and efficiency is modified by introducing a threshold for the γ value in addition to the ΔHU value. In particular:

$$\eta = \frac{number\ of\ voxels\ with\ \gamma > threshold_{\gamma}\ and\ \Delta HU > threshold_{\Delta HU}}{number\ of\ voxels\ with\ \Delta HU > threshold_{\Delta HU}} \tag{3.3}$$

$$\epsilon = \frac{number\ of\ voxels\ with\ \gamma > threshold_{\gamma}\ and\ \Delta HU > threshold_{\Delta HU}}{number\ of\ voxels\ with\ \gamma > threshold_{\gamma}} \tag{3.4}$$

The 2D maps of the gamma index are then normalised setting the maximum of the gamma values at 1. In the two-dimensional analysis, the threshold value was varied from 0 to 1. A good reference value is found to be 0.3. A suitable threshold for the ΔHU value is found to be 100 HU, which is lower than the previous 3D case due to the average process.

The procedure adopted for each patient is to derive the 2D map of ΔHU from the two CTs, projecting all the 3D maps of gamma index used in the previous optimisation. Then, the purity and efficiency values are calculated according to the new definitions. The optimization rationale is the same as in the 3D case: find a set of values of DTA and DD that can nearly maximize the purity for all the patients.

3.3.1 2D maps of absolute HU differences

The 2D ΔHU maps obtained from the projection process of the 3D maps for all analysed patients are shown in Figure 3.13.

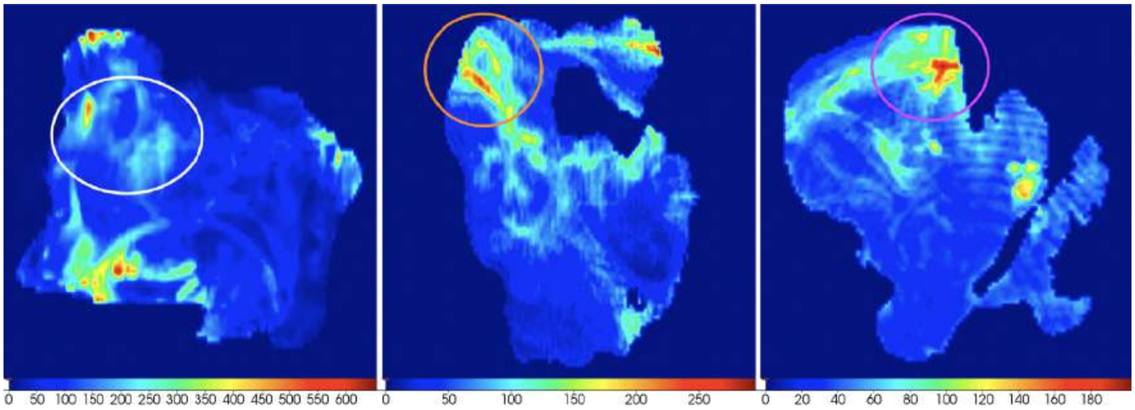

Figure 3.13: 2D maps of HU differences between the two CTs obtained by projecting the 3D maps along the direction of the primary beam of the PZ1 (left), PZ4 (centre) and PZ6 (right).

In the PZ1 map there are still areas of co-registration effects; this is still expected and unavoidable as the primary beam passes through the mandibular region, which is positioned sightly different between the two CTs, even if no morphological changes happened. Nevertheless, the morphological changes affected are visible and are circled in white.

The PZ4 map is less affected by co-registration effects. The morphological variation under investigation is clearly visible (orange circle). Moreover, its shape is as expected, since the variation in the 3D map has the shape of a spherical shell.

The map of PZ6 is also little affected by co-registration effects. The second small variation is clearly visible in the purple circle.

3.3.2 Results of the 2D optimisation of the gamma index test parameters

Purity

Figure 3.14 shows the purity values obtained by analysing the gamma index maps with all the combinations of DTA and DD values described in Table 3.1 for each patient. In this analysis the MC simulation results for PZ6 have been used. It has been done since the gamma index maps obtained from the data collected at CNAO

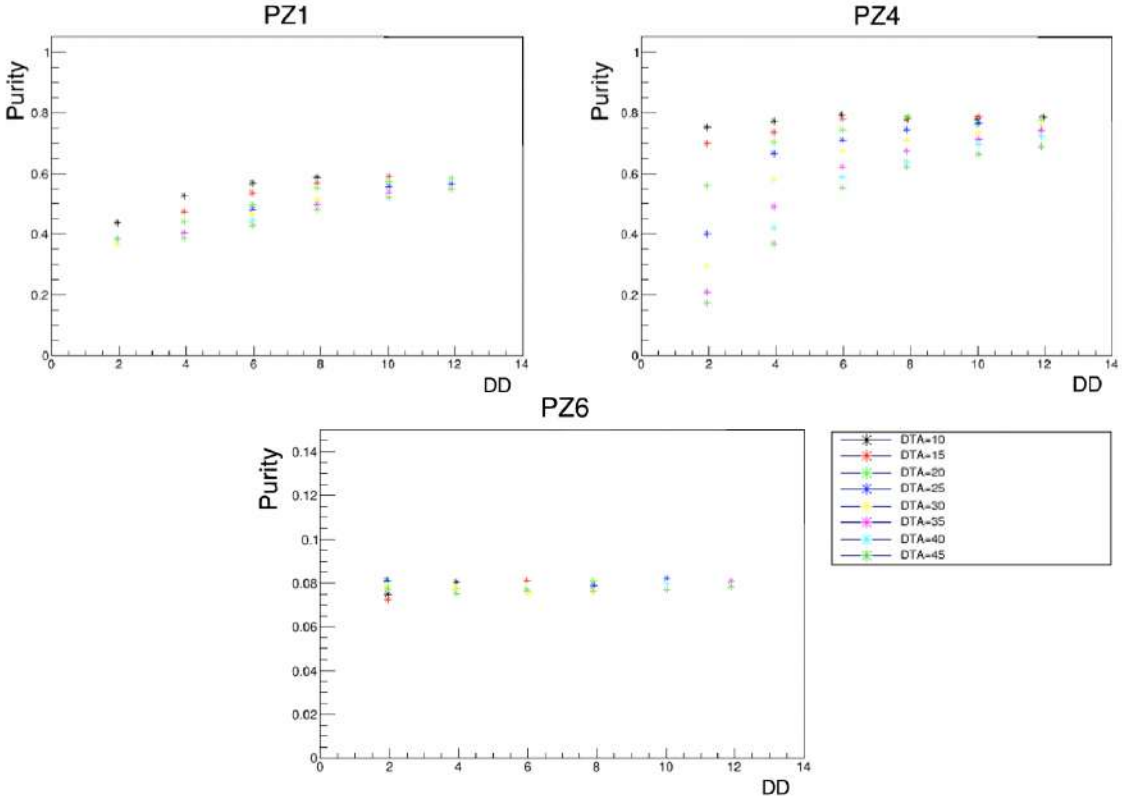

Figure 3.14: Purity as a function of DTA and DD parameters for PZ1, PZ4 and PZ6 obtained in the 2D optimization.

are similar to the MC maps, but are affected by much more background noise. This is probably due to the fact that the pre-treatment CT of PZ6 has been taken about two weeks before the first treatment fraction, the double with respect to the other patients. The correlation between the emission map of the secondary fragments of the first fraction and the pre-treatment CT is lower.

Considering all the optimization results of all the patients, the purity values are significantly higher than those obtained in the 3D case, even by a factor of 10 for PZ4. In addition, for all patients the values of DTA and DD that maximise purity are the same: DTA = 10 cm and DD = 12%. This is useful in view of the possibility to use the DP in the clinical routine.

Figure 3.15 shows the 2D gamma index maps of all three patients analysed with the parameters DTA = 10 cm and DD = 12%. Comparing these maps with the corresponding 2D maps of ΔHU shown in Figure 3.13, the areas with a high γ value (red circled areas) are also the areas with a high ΔHU. Thus, morphological variations can be detected even in the two-dimensional analysis. In addition, the 2D gamma index maps show only one cluster of red voxels, excluding PZ1 due to co-registration effect. It can be concluded that such variations can be identified even more clearly. This conclusion is also supported by the higher purity values obtained compared with the 3D case.

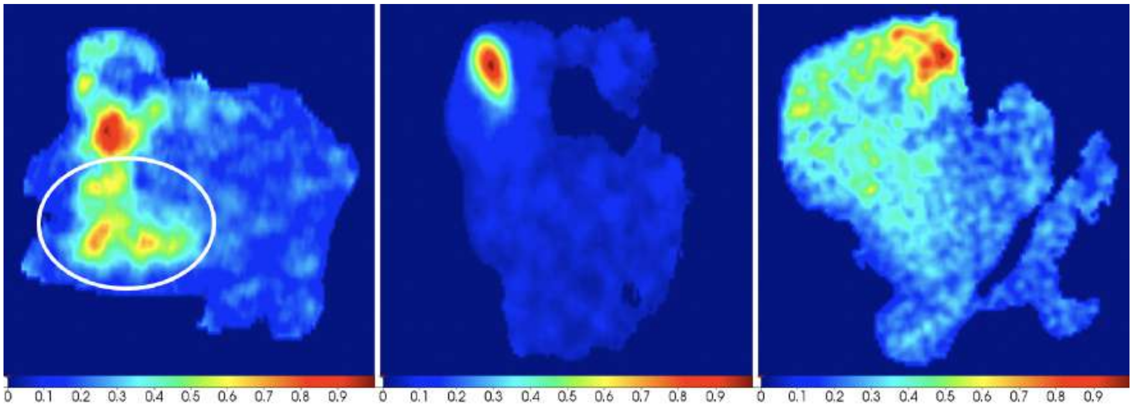

Figure 3.15: 2D maps of gamma index obtained with the parameters that maximizing purity, DTA = 10 cm and DD = 12%, for PZ1 (left), PZ4 (centre) and PZ6 (right). Co-registration effects in PZ1 are shown in the white circle.

In PZ1, there are also other small clusters of discrepant pixels in the area of the mandible as pointed out by the white circle in Figure 3.15, but they are smaller and more spatially spread than the cluster associated with the morphological change of interest. In the other cases, the correlation between the detected discrepant pixels (red pixels in the gamma index maps) and the pixels included in the varied region (red pixels in the ΔHU maps) is evident. However, despite the effect of the mandible in PZ1, it is possible to retrieve the 3D information of the discrepant gamma index zones and trace back to where the possible morphological change occurred. In this way, it is possible to understand whether the discrepancy is due to a very mobile organ such as the mandible, or whether there has actually been a morphological change that may lead to a re-evaluation CT.

As shown in Figure 3.14, for all the patients, there are different values of DD and DTA that provide almost the same maximum value of purity. In order to choose the best combination of DD and DTA, the values that provides the gamma index maps with the best signal to background ratio has been chosen. Figure 3.16 shows the gamma index maps with all the combinations of the extreme DTA and DD values analysed for PZ6 (DTA = 10 *cm* and 45 *cm*, DD = 2% and 12%). It can be seen that the maps are very similar: the red pixel clusters remain the same. The only thing that changes is the background noise of each map, which is minimal for values of DTA = 10 *cm* and DD = 12%. For this reason they have been chosen. The same result is obtained analysing the other patients.

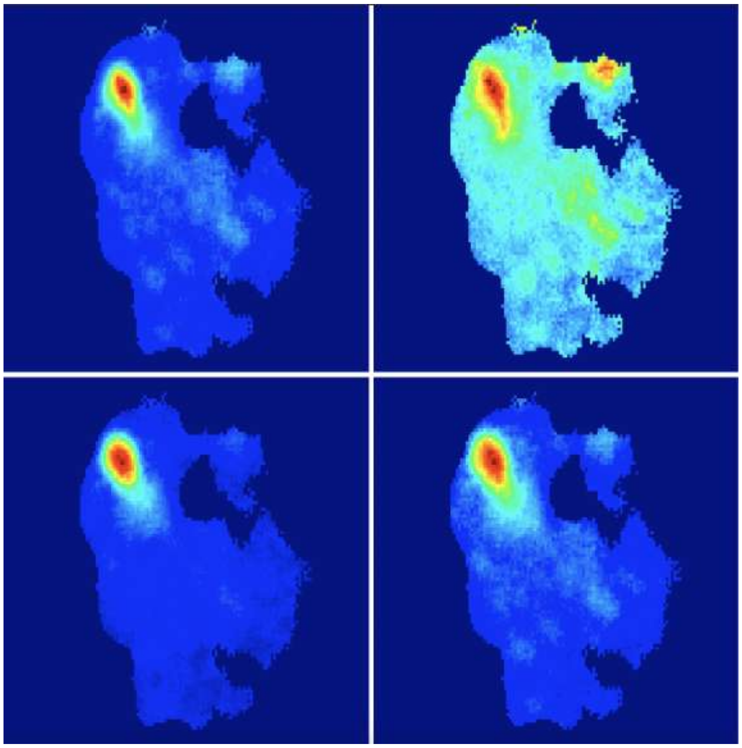

Figure 3.16: 2D maps of the gamma index of PZ4 with different parameters: DTA = 10 *cm* and DD = 2% (top left); DTA = 45 *cm* and DD = 2% (top right) ; DTA = 10 *cm* and DD = 12% (bottom left); DTA = 45 *cm* and DD = 12% (bottom right).

Efficiency

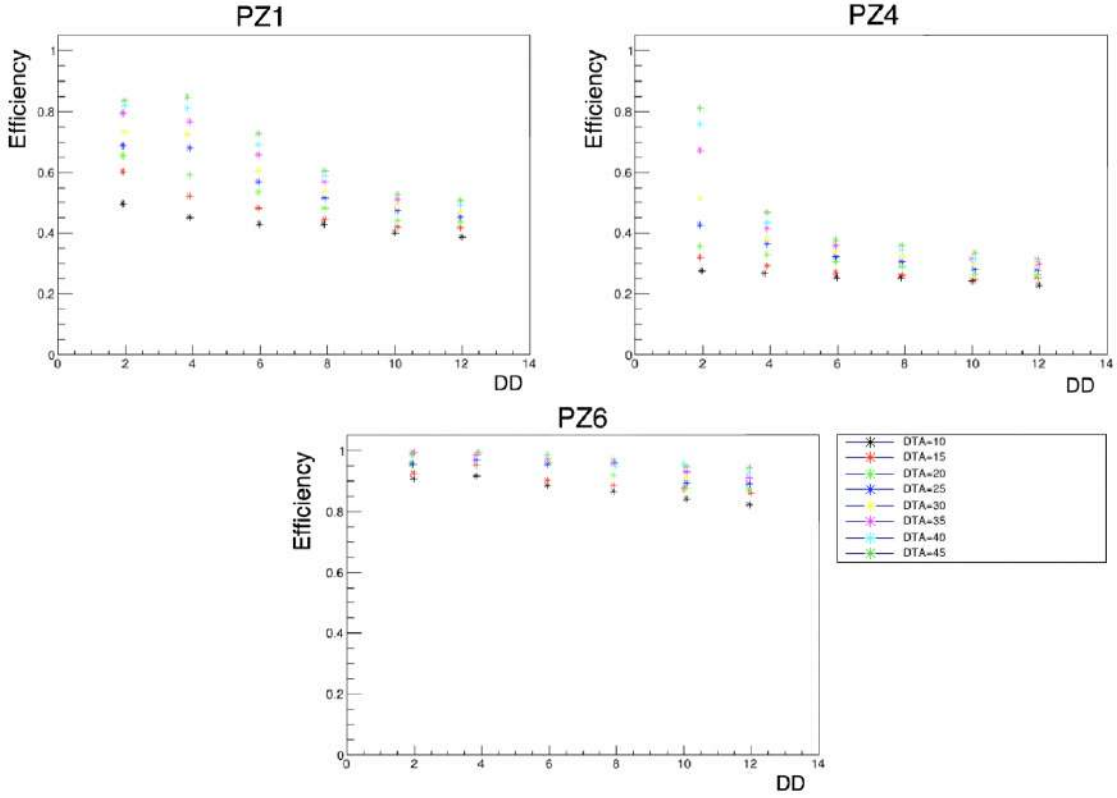

Figure 3.17: Efficiency as a function of DTA and DD parameters for PZ1, PZ4 and PZ6 obtained in the 2D optimization.

Figure 3.17 shows the evolution of the efficiency with the variation of DTA and DD parameters. As in the case of purity, the values obtained for each patient are higher than in the three-dimensional case. For PZ1, there is a maximum at $\eta = 0.85$ for DTA = 45 cm and DD = 4%. Then the efficiency decreases and for the parameters that maximise the purity (DTA = 10 cm and DD = 12%) there is a value of approximately $\eta = 0.4$. For PZ4, the values obtained are much lower. The reason for this is shown in Figure 3.18. In addition to the effects of co-registration, which are small, it can be seen that the cluster of voxels detected as discrepant is not perfectly superimposed on the cluster of voxels associated with the morphological variation. This small shift between the two clusters greatly reduces the efficiency.

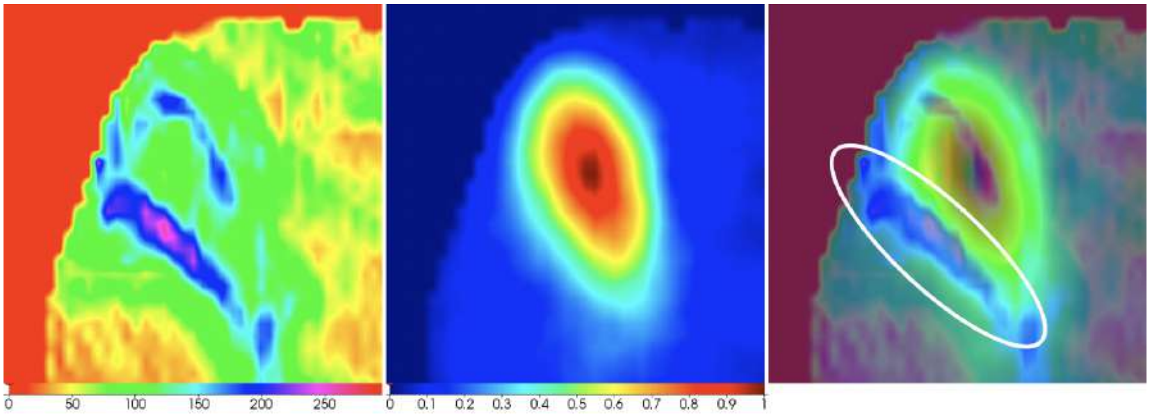

Figure 3.18: 2D map of ΔHU of PZ4 (left) and the 2D map of gamma index with values of DTA = 10 *cm* and DD = 12% (centre). The two map are superimposed in the right panel. Note the small shift between the two maps in the white circle.

In the MC simulation, this non-perfect overlap of the clusters was found, but it is less evident. Consequently, the efficiency values obtained from the MC simulation are higher as shown in Figure 3.19. For values of DTA = 10 *cm* and DD = 4%, the efficiency is approximately $\eta = 0.4$.

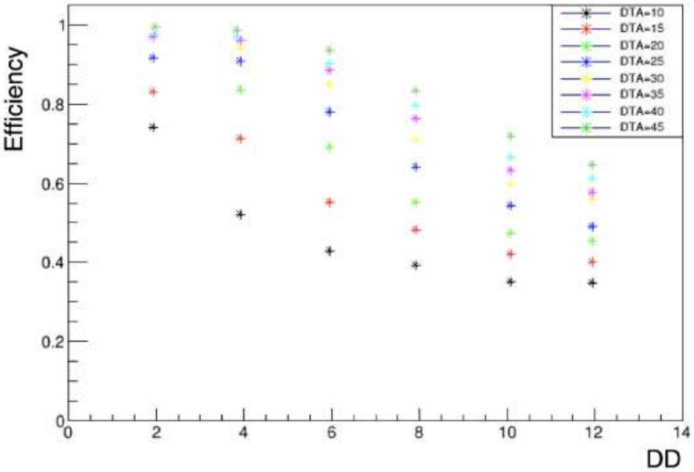

Figure 3.19: Efficiency as a function of DTA and DD values obtained by analysing the MC simulation of PZ4.

On the other hand, PZ6 shows very high efficiencies for all values of DTA and DD. As illustrated in Figure 3.20, the clusters of discrepant pixels of the gamma index map and the cluster associated with morphological variation of the ΔHU map overlap almost perfectly. This, despite the few effects of co-registration, leads to a high efficiency value. For DTA $= 10\ cm$ and DD $= 4\%$, a value of $\eta \sim 0.8$ is obtained.

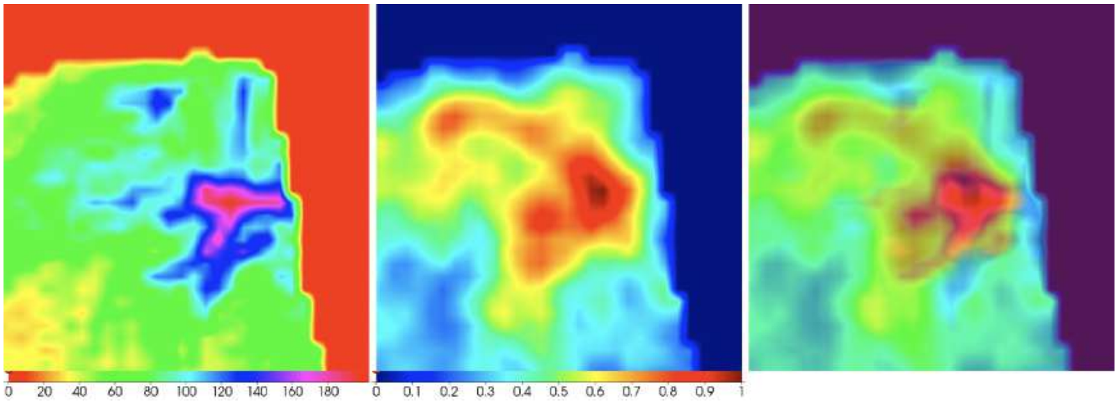

Figure 3.20: 2D map of ΔHU of PZ6 (left) and the 2D map of gamma index with values of DTA $= 10\ cm$ and DD $= 12\%$ (centre). The two map are superimposed in the right panel. Note the perfect overlap between the cluster associated with morphological variation (blue/purple voxels) and the cluster of voxels detected as discrepant by the gamma index test (red voxels).

The efficiencies in the two-dimensional case are significantly higher than in the 3D case. However, there are also disadvantages. The most important one is the loss of information along one dimension, i.e. the depth at which the morphological change occurred. The location of any morphological change is certainly important, but not fundamental in deciding on the acquisition of a re-evaluation CT. Furthermore, if a morphological change is detected in the 2D gamma index map, the 3D map can be used later to locate it more precisely.

3.4 Efficiency evaluation

The efficiencies obtained vary between patients: 0.4 for PZ1 and PZ4, 0.8 for PZ6. It was decided to adopt a slightly different strategy: not to include the entire CT in the analysis, but only the zone of morphological variation. This choice is also dictated by the desire to eliminate spurious co-registration effects scattered throughout the ΔHU map. By comparing the efficiency obtained by considering the whole map and that obtained by considering only the area of morphological variation, the impact of the co-registration effects on the efficiency value calculation can be also estimated. Figure 3.21 shows the areas of the ΔHU maps considered for the analysis.

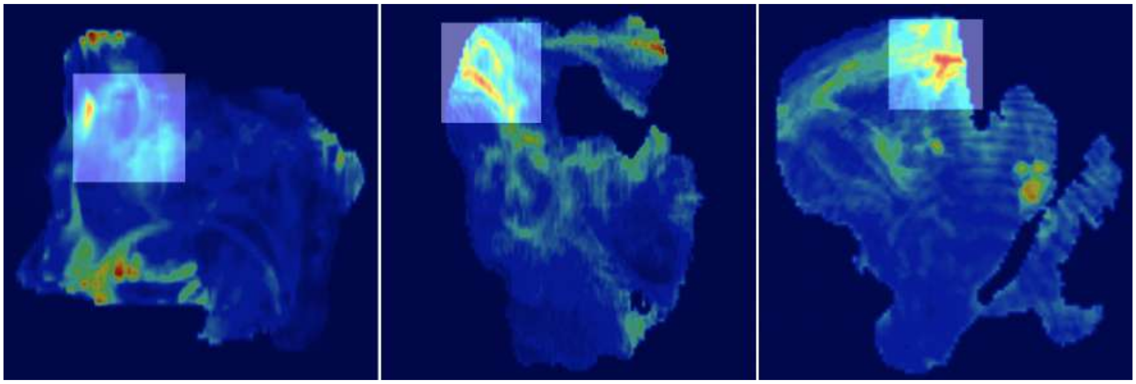

Figure 3.21: 2D ΔHU maps of PZ1 (left), PZ4(centre) and PZ6 (right) with the areas around the morphological variation considered in the analysis highlighted in the white square.

The trends of the efficiencies as a function of the DTA and DD parameters are shown in Figure 3.22 for each patient. As expected, the efficiencies are much higher in all cases as the co-registration effects have been eliminated. In the case of PZ1 there is an efficiency of almost 100% for some values of DTA and DD. For the parameter values that maximise purity, DTA = 10 cm and DD = 12%, the efficiency is of about $\sim$ 0.6, thus increasing the value obtained by considering the whole map by 0.2. In the case of PZ4, the trend is also very similar with some parameters of DTA and DD for which the efficiency is of about $\sim$ 1. For the parameters DTA = 10 cm and DD = 12%, the value of the efficiency is $\sim$ 0.6. In the case of PZ6, the efficiency is of about $\sim$ 1 for all the values of DTA and DD.

It can be concluded that the effects of co-registration have a significant impact on the value of efficiency. In particular, there is an increase of the efficiency calculation of about 20% for all the DD and DTA values. In addition, it is possible to say that

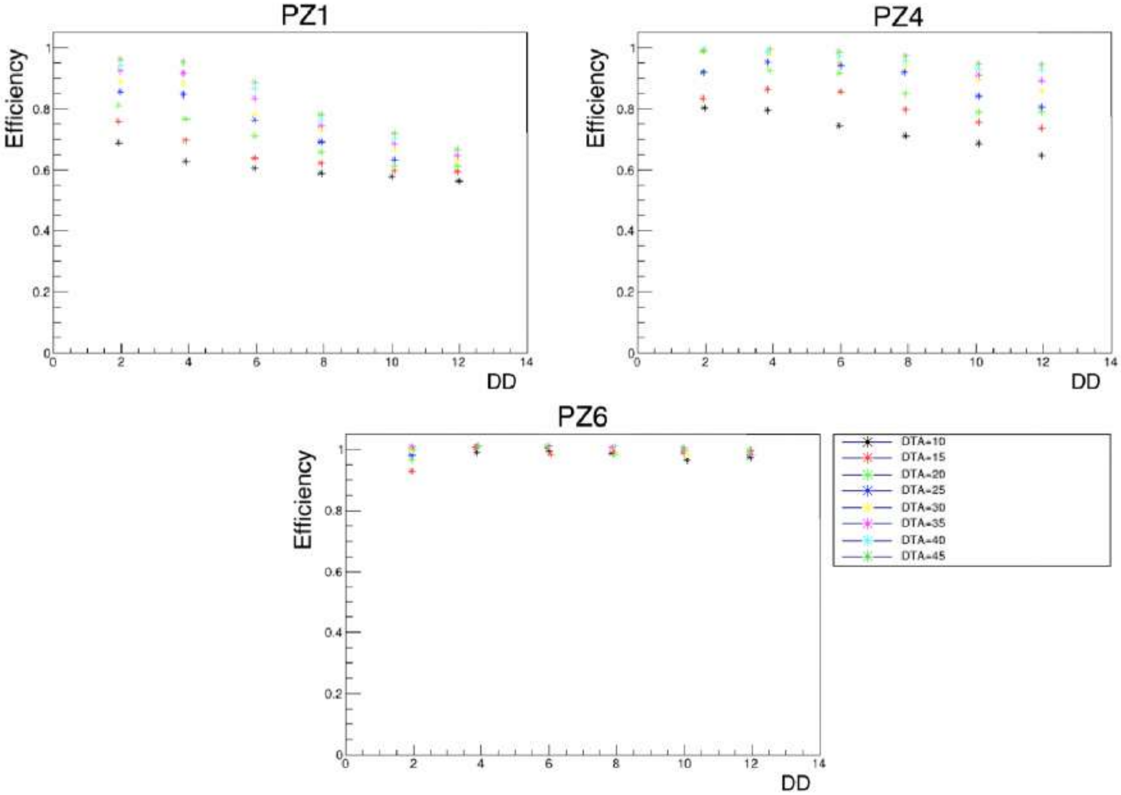

Figure 3.22: Efficiency trends as a function of DTA and DD parameters for PZ1, PZ4 and PZ6 considering only the areas around the morphological variation.

the value of efficiency depends on too many factors to find a single value for all patients.

Conclusions

During this thesis I studied the potential of an innovative inter-fractional range monitoring technique to spot morphological changes occurred in the patient among different fractions of carbon ions treatments. The technique is based on the measurement of secondary charged particles detected by the DP, developed in the framework of the INSIDE project. At the moment, there is an INSIDE clinical trial (ClinicalTrials.gov Identifier: NCT03662373) ongoing at the CNAO facility. Three patients with a re-evaluation CT that showed morphological changes have been selected for this work. This thesis has two main objectives: the first is to optimise the gamma index test parameters in order to find a set of values that are suitable for all the clinical cases; the second is to estimate the sensitivity of the DP. The optimization and the DP performance evaluation are carried out by means of two indicators defined as purity and efficiency. The first gives an estimation on the accuracy of the morphological changes reported by the DP. The latter gives an estimate of the capability of the DP in the detection of morphological changes.

Evaluating the efficiency and the purity on the whole CT with a three dimensional approach showed different artifacts. These effects are due to the physics of the secondary particle emission and due to the presence of highly mobile organs that mimic the effect of morphological changes (co-registration effect). To overcome these problem, a two-dimensional approach has been adopted projecting both the CTs and the gamma index 3D maps along a plane perpendicular to the beam direction. In this way, co-registration effects are partially limited and the effect occurring along the beam direction is absorbed. The optimisation of the free gamma index parameters has been done maximising the purity and choosing the values that provide the gamma index map with the best signal to background ratio. The results show the possibility to optimise the gamma index parameters for all the patients, with DTA = 10 cm and DD = 12%. This leads to the possibility to use the DP within a clinical environment, dealing with a variety of patients and cases.

Considering the efficiency, even with the two-dimensional approach there are significant co-registration effects. In order to completely eliminate these effects, only the area around the morphological variation has been considered. The efficiencies obtained for the patients are in a range of $0.6 \div 1$, depending on different parameters such as depth, volume and shape of the tumour, location of morphological variation relative to the DP, direction and position of the incoming beam.

The preliminary results obtained by the thesis work are promising, given the possibility to use the DP in a clinical routines to perform an inter-fractional monitoring on the carbon ion treatments. However, more data are needed to complete the detector performance assessment. The clinical trial should restart in 2024 and more patients with different pathologies will be included. The analysis tools developed within this thesis will be exploited to analyze the new data, completing the evaluation of the DP sensitivity.

Bibliography

[1] World Health Organization. URL: `https://www.who.int/health-topics/cancer#tab=tab_1`.

[2] Jacques Ferlay MSc et al. Hyuna Sung PhD. Global Cancer Statistics 2020: GLOBOCAN Estimates of Incidence and Mortality Worldwide for 36 Cancers in 185 Countries. *CA: A Cancer Journal for Clinicians*, 2021.

[3] PTCOG 2023 Facilities Brochure. URL: `https://www.ptcog.site/index.php/facilities-in-operation-public`.

[4] Orecchia R. et al. Particle beam therapy (hadrontherapy): basis for interest and clinical experience. *European journal of cancer*, 1990,1998.

[5] William R. Leo. *Techniques for Nuclear and Particle Physics Experiments.* Springer-Verlag Berlin Heidelberg GmbH, 1994.

[6] Aafke C. Kraan. Range verification methods in particle therapy: Underlying physics and monte carlo modeling. *Frontiers in oncology*, 2015.

[7] K Nakamura and Particle Data Group. Review of particle physics. *Journal of Physics G: Nuclear and Particle Physics, 37(7A):075021*, 2010.

[8] M. Plum. Interceptive beam diagnostics-signal creation and materials interactions. *Proceedings of AIP, Knoxville, Tennessee*, 732:23–46, 2004.

[9] D. Davino. Theory, design and tests on a prototype module of a compact linear accelerator for hadrontherapy. Master's thesis, Università degli Studi del Sannio, 2016.

[10] N.J. Carron. *An Introduction to the Passage of Energetic Particles through Matter*. CRC Press, 2006.

[11] M. Testa. *Physical measurements for ion range verification in charged particle therapy*. PhD thesis, Université Claude Bernar, 2010.

[12] Antony J. Lomax. Charged particle therapy: the physics of interaction. *The cancer journal (Sudbury, Mass.)*, 2009.

[13] Virgil L. Highland. Some practical remarks on multiple scattering. *Nuclear Instruments and Methods, 129(2):497 – 499*, 1975.

[14] Schardt Dieter and Elsasser Thilo. Heavy-ion tumor therapy: Physical and radiobiological benefits. *Reviews of modern physics, 82*, 2010.

[15] Jan J Wilkens and Uwe Oelfke. Direct comparison of biologically optimized spread-out bragg peaks for protons and carbon ions. *International Journal of Radiation Oncology* Biology* Physics*, 70(1):262–266, 2008.

[16] K. Gunzert-Marx et al. Secondary beam fragments produced by 200 mev/u 12c ions in water and their dose contributions in carbon ion radiotherapy. *New Journal of Physics 10*, 2008.

[17] Sihver L. et al. Depth-dose distributions of high-energy carbon, oxygen and neon beams in water. *Jpn. J. Med. Physics 18*, 2003.

[18] C. Steffer J. D. Harrison. The ICRP protection quantities, equivalent and effective dose: their basis and application. *Radiation protection dosimetry vol. 127, 1-4*, 2007.

[19] Hall Eric J. and Giaccia Amato J. *Radiobiology for the Radiologist.* 8th edition, Lippincott, 2019.

[20] Elahe Alizadeh, Thomas M. Orlando, and Léon Sanche. Biomolecular damage induced by ionizing radiation: The direct and indirect effects of low-energy electrons on DNA. *Annual Review of Physical Chemistry*, 66(1):379–398, 2015.

[21] Ben Milborne, Abul Arafat, Rob Layfield, Alexander Thompson, and Ifty Ahmed. The use of biomaterials in internal radiation therapy. *Recent Progress in Materials*, 2:1–34, 2020.

[22] P. L. Olive. The role of DNA single-and double-strand breaks in cell killing by ionizing radiation. *Radiation research 150.5s*, 1998.

[23] Leenhouts H.P. Chadwick K.H. A molecular theory of cell survival. *Phys. Med. Biol. 13, 78–87*, 1973.

[24] van Leeuwen C. M. et al. The alfa and beta of tumours: a review of parameters of the linear-quadratic model, derived from clinical radiotherapy studies. *Radiation oncology (London, England), 13(1), 96*, 2018.

[25] Amin Kassis. Therapeutic radionuclides: Biophysical and radiobiologic principles. *Seminars in nuclear medicine*, 38:358–66, 2008.

[26] Ugo Amaldi e Gerhard Kraft. Radiotherapy with beams of carbon ions. *Reports on Progress in Physics*, 2005.

[27] van Kersen GR Broerse JJ, Barendsen GW. Survival of cultured human cells after irradiation with fast neutrons of different energies in hypoxic and oxygenated conditions. *Int J Radiat Biol Relat Stud Phys Chem Med 13:559-572*, 1968.

[28] S. Ritter et al. W.K. Weyrather. RBE for Track-Segment Irradiation in Cell Lines of Differing Repair Capacity. *International journal of radiation biology, 75(11), 1357–1364*, 1999.

[29] G. W. Barendsen. Responses of cultured cells, tumours, and normal tissues to radiations of different linear energy transfer. *pp 293-356 of Current Topics in Radiation Research. Vol. IV. Ebert, Michael Howard, Alma (eds.). New York, John Wiley and Sons, Inc.*, 1968.

[30] C. A. Tobias E. A. Blakely et al. Inactivation of human kidney cells by high-energy monoenergetic heavy-ion beam. *Radiation Research 80, pp. 122–160*, 1979.

[31] Barendsen GW, Koot CJ, van Kersen GR, Bewley DK, Field SB, Parnell CJ. The effect of oxygen on impairment of the proliferative capacity of human cells in culture by ionizing radiations of different LET. *Int J Radiat Biol Relat Stud Phys Chem Med 10:317-327*, 1966.

[32] M. Fischetti. *Inter-fractional monitoring in Particle Therapy treatments with* ^{12}C *ions exploiting the detection of secondary particles: simulation studies and clinical trial results at the CNAO facility.* PhD thesis, Sapienza Università di Roma, 2020.

[33] Bridier A. Chavaudra J. Definition of volumes in external radiotherapy: ICRU reports 50 and 62. *Cancer radiotherapie : journal de la Societe francaise de radiotherapie oncologique*, 2001.

[34] J. Mattingly et al. K.S. Ytre-Hauge, K. Skjerdal. A monte carlo feasibility study for neutron based real-time range verification in proton therapy. *Sci Rep 9, 2011*, 2019.

[35] Lerendegui-Marco, J., Balibrea-Correa, J., Babiano-Suárez, V., Caballero, L., Domingo-Pardo, C., and Ladarescu, I. Simultaneous neutron and gamma imaging system for real time range and dose monitoring in hadron therapy and nuclear security applications. *EPJ Web Conf.*, 261:05001, 2022.

[36] C. A. Tobias E. A. Blakely et al. PET monitoring in hadrontherapy. *Nuclear Medicine Review 15, pp. 37–42*, 2002.

[37] K. Parodi et al. Patient study of in vivo verification of beam delivery and range, using positron emission tomography and computed tomography imaging after proton therapy. *International journal of radiation oncology, biology, physics, 68(3), 920-934*, 2007.

[38] Inoue K. et al. Nishio T., Miyatake A. Experimental verification of proton beam monitoring in a human body by use of activity image of positron-emitting nuclei generated by nuclear fragmentation reaction. *Radiological Physics and Technology 1.1, pp. 44–54.*, 2008.

[39] W. Hsi et al. In vivo verification of proton beam path by using post-treatment PET/CT imaging. *Med Phys 36, pp. 4136–4146*, 2009.

[40] X. Zhu et al. Monitoring proton radiation therapy with in-room PET imaging. *Phys. Med. Biol. 56.13, pp. 4041*, 2011.

[41] G. Shakirin et al. Implementation and workflow for PET monitoring of therapeutic ion irradiation: a comparison of in-beam, in-room, and off-line technique. *Phys. Med. Biol. 56.5, pp. 1281–1298*, 2011.

[42] Pawelke J. et al. In-beam PET imaging of the control of heavy-ion tumour therapy. *IEEE Trans Nucl Sci 44, pp. 1492–1498*, 1997.

[43] Enghardt W. et al. Charged hadron tumour therapy monitoring by means of PET. *Nucl Instrum Methods 525, pp. 284–288*, 2004.

[44] Iseki Y. et al. Positron camera for range verification of heavy-ion radiotherapy. *Nucl Instrum Methods 515, pp. 840–849*, 2003.

[45] Vecchio S. et al. A PET prototype for in-beam monitoring of proton therapy. *IEEE Nuclear Science Symposiums 56.1, pp. 51–56.*, 2009.

[46] T. Nishio et al. The development and clinical use of a beam ON-LINE PET system mounted on a rotating gantry port in proton therapy. *International Journal of Radiation Oncology Biology Physics 76.1, pp. 277–286*, 2010.

[47] Ferrero V. et al. The INSIDE project: on-line monitoring and simulation validation with the in-beam PET scanner. *Journal of Physics: Conference Series 841, p. 012011*, 2017.

[48] T. Nishio et al. Precise measurement of prompt photon emission from 80 MeV/u carbon ion beam irradiation. *Journal of Instrumentation 7.03, P03001*, 2012.

[49] I. Mattei et al. Prompt-γ production of 220 MeV/u ^{12}C ions interacting with a PMMA target. *PMB 10*, 2015.

[50] Verburg J. M. et al. Energy and time resolved detection of prompt γ-rays for proton range verificationg. *Phys. Med. Biol. 58.20, pp. 37– 49*, 2013.

[51] Krimmer J. et al. Prompt-gamma monitoring in hadrontherapy: A review. *J. Instrum. 878, pp. 58–73*, 2018.

[52] Thirolf P. G. et al. A compton camera prototype for prompt-γ medical imaging. *EPJ Web of Conferences 117.05005*, 2016.

[53] Haettner E. et al. Experimental fragmentation studies with ^{12}C therapy beams. *Radiat Prot Dosimetry 122, pp. 485–487*, 2006.

[54] L. Piersanti et al. Measurement of charged particle yields from PMMA irradiated by a 220 MeV/u ^{12}C beam. *Physics in Medicine and Biology 59.7, pp. 1857–1872*, 2014.

[55] I. Mattei et al. Addendum: Measurement of charged particle yields from PMMA irradiated by a 220 MeV/u ^{12}C beam. *Physics in Medicine and Biology 62.21, pp. 8483–8494*, 2017.

[56] C. Agodi et al. Charged particle's flux measurement from PMMA irradiated by 80 MeV/u carbon ion beam. *Physics in Medicine and Biology 57.18, pp. 5667–5678*, 2012.

[57] A. Rucinski et al. Secondary radiation measurements for particle therapy applications: Charged secondaries produced by ^{16}O ion beams in a PMMA target at large angles. *Physica Medica: European Journal of Medical Physics 64, pp. 45–53*, 2019.

[58] G. Traini et al. Design of a new tracking device for on-line beam range monitor in carbon therapy. *Physica Medica 34, pp. 18–27*, 2017.

[59] I. Mattei et al. Charged particles and neutron trackers: Applications to particle therapy. *Nuclear Instruments and Methods in Physics Research 954, p. 161229. issn: 0168-9002*, 2020.

[60] G. Traini et al. Review and performance of the Dose Profiler, a particle therapy treatments online monitor. *Physica Medica 65, pp. 84–93. issn: 1120-1797*, 2019.

[61] M. G. Bisogni et al. INSIDE in-beam positron emission tomography system for particle range monitoring in hadrontherapy. *Journal of Medical Imaging 4.1*, 2017.

[62] E. Fiorina et al. Monte Carlo simulation tool for online treatment monitoring in hadrontherapy with in-beam PET: A patient study. *Physica Medica 51, pp. 71–80. issn: 1120-1797*, 2018.

[63] Giordanengo S. et al. The CNAO dose delivery system for modulated scanning ion beam radiotherapy. *Medical physics 42, p. 263*, 2015.

[64] ROOT User Guide 2023. URL: `https://root.cern.ch/`.

[65] Fattori G. et al. Commissioning of an integrated platform for time-resolved treatment delivery in scanned ion beam therapy by means of optical motion monitoring. *Technol. Cancer Res. Treat. 13.6, pp. 517–528*, 2014.

[66] Ricotti R. et al. Long-time clinical experience in patient setup for several particle therapy clinical indications: management of patient positioning and evaluation of setup reproducibility and stability. *The British Journal of Radiology 93.1107, p. 20190595*, 2020.

[67] Richard O. Duda and Peter E. Hart. Use of the hough transformation to detect lines and curves in pictures. *Commun. ACM*, 15(1):11–15, 1972.

[68] CH Clark Mohammad Hussein. Challenges in calculation of the gamma index in radiotherapy–towards good practice. *Physica Medica, 36:1–11*, 2017.

[69] G. Giacchi. Monitoraggio 3D inter-frazione delle variazioni morfologiche in trattamenti con ioni ^{12}C al CNAO tramite rivelazione di frammenti secondari carichi. Master's thesis, Sapienza Università di Roma, 2022.

[70] A. Belardo. Studio Monte Carlo dell'utilizzo di PAPRICA per inter-fractional monitoring 3D su pazienti trattati al CNAO con adroterapia. Master's thesis, Università degli Studi di Milano, 2022.

[71] Fasso A Ferrari A, Sala P R and Ranft J 2005. CERN-2005-010, SLAC-R-773, INFN-TC-05-11.

[72] Battistoni G et al. The FLUKA code: An accurate simulation tool for particle therapy. *Frontiers in oncology 6 116*, 2016.

[73] Flair User Guide 2023. URL: `http://www.fluka.org/flair/index.html`.

[74] Slicer 3D User Guide 2023. URL: `https://www.slicer.org/wiki/`.

[75] G Battistoni et al. M Fischetti, G Baroni. Inter-fractional monitoring of ^{12}c ions treatments: results from a clinical trial at the CNAO facility. *Scientific Reports 10, 20735*, 2020.

[76] I. Mattei et al. Measurement of ^{12}C Fragmentation Cross Sections on C, O, and H in the Energy Range of Interest for Particle Therapy Applications. *IEEE Transactions on Radiation and Plasma Medical Sciences (Volume: 4, Issue: 2, Page(s): 269 - 282)*, 2020.